

Morphological Characterization and Analysis of Ion-Containing Polymers Using Small Angle X-ray Scattering

Mingqiang Zhang

Dissertation submitted to the faculty of the Virginia Polytechnic Institute and State University in partial fulfillment of the requirements for the degree of

Doctor of Philosophy

In

Chemistry

Robert B. Moore, Chair
Timothy E. Long
Hervé Marand
Judy S. Riffle

October, 2014
Blacksburg, Virginia

Keywords: perfluorosulfonic acid ionomer, Nafion[®], ionomer, proton exchange membrane, block copolymer, morphology, small angle X-ray scattering, solution processing

Morphological Characterization and Analysis of Ion-Containing Polymers Using Small Angle X-ray Scattering

Mingqiang Zhang

Abstract

Small angle X-ray scattering (SAXS) has been widely used in polymer science to study the nano-scale morphology of various polymers. The data obtained from SAXS give information about sizes and shapes of macromolecules, characteristic distances of partially ordered materials, pore sizes, and so on. The understanding of these structural parameters is crucial in polymer science in that it will help to explain the origin of various properties of polymers, and guide design of future polymers with desired properties.

We have been able to further develop the contrast variation method in SAXS to study the morphology of Nafion 117CS containing different alkali metal ions in solid state. Contrast variation allows one to manipulate scattering data to obtain desired morphological information. At room temperature, only the crystalline peak was found for Na⁺-form Nafion, while for Cs⁺-form Nafion only the ionic peak was observed. The utilization of one dimensional correlation function on different counterion forms of Nafion further demonstrates the necessity of contrast variation method in obtaining more detailed morphological information of Nafion. This separation of the ionic peak and the crystalline peak in Nafion provides a means to independently study the crystalline and ionic components without each other's effect, which could be further applied to other ionomer systems.

We also designed time resolved SAXS experiments to study the morphological development during solution processing Nafion. As solvent was removed from Nafion

dispersion through evaporation, solid-state morphological development occurred through a variety of processes including phase-inversion, aggregation of interacting species (e.g., ionic functionalities), and crystallization of backbone segments. To probe the real-time morphological development during membrane processing that accurately simulates industrial protocols, a unique sample cell has been constructed that allows for through-film synchrotron SAXS data acquisition during solvent evaporation and film formation. For the first time, this novel experiment allows for a complete analysis of structural evolution from solution/dispersion to solid-state film formation, and we were able to show that the crystallites within Nafion develop later than the formation of ionic domains, and they do not reside in the cylindrical particles, but are dispersed in solution/dispersion.

Besides bulk morphology of Nafion, we have also performed Grazing Incident SAXS to study the surface morphology of Nafion. We were able to manipulate the surface morphology of Nafion via neutralizing H⁺-form Nafion with different large organic counterions, as well as annealing Nafion thin films under different temperatures. This not only allows to obtain more detailed information of the nano-structures in Nafion thin films, but also provides a means to achieve desired morphology for better fuel cell applications.

We have also been able to study the polymer chain conformation in solution via measuring persistence length by utilizing solution SAXS. Different methods have been applied to study the SAXS profiles, and the measured persistence lengths for stilbene and styrenic alternating copolymers range from 2 to 6 nm, which characterizes these copolymers into a class of semi-rigid polymers. This study allows to elucidate the steric crowding effect on the chain stiffness of these polymers, which provides fundamental understanding of polymer chain behaviors in solution.

Self-assembling in block copolymers has also been studied using SAXS. We established a morphological model for a multiblock copolymer used as a fuel cell material from General Motors[®], and this morphological model could be used to explain the origins of the mechanical and transport properties of this material. Furthermore, several other block copolymers have been studied using SAXS, which showed interesting phase separated morphologies. These morphological data have been successfully applied to explain the origins of various properties of these block copolymers, which provide fundamental knowledge of structure-property relationship in block copolymers.

Acknowledgements

First of all, I would like to thank my family members. There have been many difficulties and frustrations during the past five years of my life. Without the endless support and love from my father, Zhonghou Zhang, and my mother, Zhiqun Tian, I could not be able to become who I am today. I would also like to thank my friends, Jie Chen, Delong Zhang, Xinwei Li, Chenfeng Fu, Chao Wang, and Zhengmian Chang, who keep encouraging me whenever needed.

As a graduate student at Chemistry Department in Virginia Tech, I really want to express my gratitude to Chemistry Department for giving me the precious opportunity to pursue my Ph.D. degree in Chemistry. Also, I would like to thank all my committee members, Prof. Timothy E. Long, Prof. Hervé Marand, and Prof. Judy S. Riffle, for their advice, help and support during my pursue in Ph.D. degree, as well as their patience with my research. As a group member in Moore Research Group, I received so much care and help and I would like to thank all the members past and present, Dr. E. Bruce Orler, Dr. Jong Keun Park, Dr. Sonya Bensen, Dr. Gilles M. Divoux, Dr. Scott J. Forbey, Amanda Hudson, Xijin Yuan, Elise Naughton, Jeremy Beach, Gregory Fahs, Ted Canterbury and Orkun Kaymakci, who have spent the most memorable five years with me in my life.

As I have collaborated with many graduate students from different departments across Virginia Tech, I would like to thank Dr. Renlong Gao, Dr. Shijing Chen, Dr. Tianyu Wu, Dr. Yi Li, Dr. Sean T. Hemp, Dr. Musan N. Zhang, Dr. Chen Chen, from whom I learned so much in different areas of polymer science, and also was inspired by their enthusiasm and persistence in science. I would also like to thank Dr. Garth L. Wilkes for his valuable suggestions and help in my research.

Finally, I would thank my advisor Prof. Robert B. Moore for his guidance, help, and support during the past five years. Not only did you help me on my research, but also did your fully support and help in my life and career. The lessons that you taught me to be an independent thinker and leader, as well as impassioned collaborator, would keep guiding me in my life. You are also a role model for being an excellent instructor, scientist, and mentor, and a great person. It is really my extreme luck and honor to have you as my advisor, and I can never thank you enough for inspiring me to be a better person every day.

Table of Contents

Acknowledgements.....	iiv
Table of Contents.....	vi
List of Abbreviations.....	x
List of Figures.....	xiv
List of Tables.....	xxi
Chapter 1 Basics of Small Angle X-ray Scattering.....	1
1.1 Introduction.....	1
1.2 Theory of Small Angle X-ray Scattering.....	1
1.2.1 Scattering Vector.....	1
1.2.2 Scattering from one free electron.....	3
1.2.3 Scattering from multiple centers.....	5
1.2.4 Contrast Variation.....	6
1.2.5 Scattering from Isolated Particles.....	8
1.2.5.1 Sphere.....	8
1.2.5.2 Infinitely Thin Rod.....	9
1.2.5.3 Infinitely Thin Circular Disk.....	9
1.2.6 Scattering from Concentrated Particles.....	10
1.2.7 Layout of SAXS system.....	13
1.2.8 Experimental Approach, Absolute Intensity, and Data Collection.....	14
1.3 Grazing Incident SAXS.....	16
1.4 References.....	19
Chapter 2 Morphological Characterization of Nafion®.....	23
2.1 Introduction.....	23
2.2 Processing Nafion.....	24
2.3 Mechanical and Thermal Properties of Nafion.....	27
2.4 Morphological Models Proposed for Nafion.....	31
2.5 Surface Morphology of Nafion.....	45
2.6 Studies of Nafion via Orientation.....	48
2.7 Further Study of Nafion and Nafion-like Materials.....	53
2.8 References.....	53
Chapter 3 Contrast Variation in Small-Angle X-ray Scattering as a Means to Isolate and Characterize Morphological Features Spanning Common Length Scales in Semicrystalline Ionomers.....	59

3.1 Introduction.....	59
3.2 Experimental Section.....	61
3.2.1 Materials	61
3.2.2 Preparation of Neutralized Perfluorinated Sulfonic Acid (PFSA) Membranes.....	62
3.2.3 SAXS Instrument.....	62
3.3 Data Analysis	63
3.4 Results and Discussion	64
3.5 Conclusions.....	72
3.6 Acknowledgement	73
3.7 References.....	73
Chapter 4 Morphological Development in Solution Processing Nafion during Solvent Evaporation.....	76
4.1 Introduction.....	76
4.2 Experimental Section.....	78
4.2.1 Materials	78
4.2.2 Preparation of Neutralized Perfluorinated Sulfonic Acid (PFSA) Membranes.....	78
4.2.3 Preparation of Nafion Dispersion	78
4.2.4 Solution Processing Procedure	79
4.2.5 Small Angle X-ray Scattering Experiment	79
4.3 Results and Discussion	81
4.4 Conclusion	87
4.5 Acknowledgement	87
Chapter 5 Effects of Annealing on the Surface Structure of Nafion Thin Films Neutralized with Organic Counterions	91
5.1 Introduction.....	91
5.2 Experimental Section.....	93
5.2.1 Materials	93
5.2.2 Preparation of Neutralized Perfluorinated Sulfonic Acid (PFSA) Membranes.....	93
5.2.3 Preparation of Nafion Dispersion	94
5.2.4 Thin Film Preparation	94
5.2.5 GISAXS	94
5.3 Results and Discussion	95
5.4 Conclusions.....	105
5.5 Acknowledgements.....	105
5.6 References.....	106

Chapter 6 Morphological Characterization of PFCB-Ionomer/PVDF Copolymer Blends from General Motors®	109
6.1 Introduction.....	109
6.2 Experimental Section	111
6.2.1 Materials	111
6.2.2 Membrane Casting Procedure.....	111
6.2.3 Small Angle X-ray Scattering.....	112
6.2.4 Atomic Force Microscopy	114
6.2.5 Through Plane Proton Conductivity Measurement.....	114
6.3 Results and Discussion	114
6.4 Conclusion	127
6.5 Acknowledgement	128
6.6 References.....	128
Chapter 7 Measurement of Persistence Length using Small Angle X-ray Scattering ¹ ...	131
7.1 Introduction.....	131
7.2 Experimental Section	136
7.2.1 Materials	136
7.2.2 Small Angle X-ray Scattering.....	137
7.3 Results and Discussion	138
7.3.1 Form Factor of Spheres.....	138
7.3.2 Study of Persistence Length using SAXS.....	139
7.4 Conclusion	145
7.5 Acknowledgements.....	145
7.6 References.....	146
Chapter 8 Morphological Characterization of Block Copolymers using Small Angle X-ray Scattering	149
8.1 Background.....	149
8.1.1 Introduction.....	149
8.1.2 Microphase Separation in Block Copolymer	150
8.1.3 SAXS as A Means to Study Microphase Separation in Block Copolymer ...	151
8.1.3.1 Invariant for Ideal Two-Phase System.....	151
8.1.3.2 Porod's Law	153
8.1.3.3 Miller Indices	153
8.1.3.4 Scattering on Ordered Nanostructures	153
8.2 Recent Published Results.....	157

8.2.1 Morphological Properties of A Series of Sulfonated Poly(arylene ether sulfone) (BPSH-BPS) Multiblock Copolymer (MBC) Ionomers	157
8.2.2 Characterization of Multiblock Partially Fluorinated Hydrophobic Poly(arylene ether nitrile) Hydrophilic Disulfonated Poly(arylene ether sulfone) Copolymers for Proton Exchange Membranes	161
8.2.3 Morphological Characterization of Multiblock Poly(arylene ether nitrile) Disulfonated Poly(arylene ether sulfone) Copolymers for Proton Exchange Membranes.....	164
8.2.4 Morphological Characterization of 4-vinylimidazole ABA triblock copolymers	168
8.2.5 Morphological Characterization of Perfectly Alternating Polycarbonate-Polydimethylsiloxane Multiblock Copolymers Possessing Controlled Block Lengths	173
8.3 Acknowledgements.....	176
8.4 References.....	176
Chapter 9 Future Work: Methods to Enhance Microdomain Orientation within Nafion	179
9.1 Introduction.....	179
9.2 Methods to Enhance Microdomain Orientation in Polymers	179
9.2.1 Applying Electric Field to Enhance Microdomain Orientation.....	179
9.2.2 Applying Magnetic Field to Enhance Microdomain Orientation	182
9.2.3 Proposed Further Work on Enhancing Microdomain Orientation in Nafion	185
9.3 References.....	187

List of Abbreviations

6FPAEB	Fluorine-terminated Poly(arylene ether benzonitrile)
AFM	Atomic Force Microscopy
APS	Argonne Photon Source
BCC	Body Centered Cubic
BPS	Sulfonated Poly(arylene ether sulfone)
BPSH	Acidified Form Sulfonated poly(arylene ether sulfone)
BVPE	Biphenyl Vinyl Ether
CV	Contrast Variation
DI	Deionized
DD	Double Diamond
DMA	Dynamic Mechanical Analysis
DMAc	Dimethylacetamide
DMSO	Dimethyl Sulfoxide
DPD	Dissipative Particle Dynamics
DSC	Differential Scanning Calorimetry
EC-AFM	Electrochemical AFM
EHM	Eisenberg-Hird-Moore
ePTFE	Expanded Microporous Polytetrafluoroethylene
EW	Equivalent Weight
FCC	Face Centered Cubic
FFT	Fast Fourier Transformation
FWHM	Full Width at Half Maximum

GISAXS	Grazing Incident SAXS
GM	General Motors
HEX	Hexagonal Packed Cylinders
ICTAS	Institute for Critical Technology and Applied Science
IEC	Ion Exchange Capacity
IEC _v	Volumetric Based Ion Exchange Capacity
IPMC	Ionic Polymer-Metal Composite
ISR	Intermediate Segregation Region
iVSANS	In-situ Vapor Sorption Small Angle Neutron Scattering
K	Kilo
KF	Knar Flex
kg	Kilogram
L	Litter
m	Meter
MaxEnt	Maximum Entropy Modeling
MBC	Multiblock Copolymer
mV	Milli Voltage
n/a	Not Available
nm	Nano Meter
NMR	Nuclear Magnetic Resonance
ODT	Order-Disorder Transition
PBI	Polybenzimidazole
PC	Polycarbonate

PEEK	Poly(etheretherketone)
PEM	Proton Exchange Membrane
PEMFC	Proton Exchange Membrane Fuel Cell
PEO- <i>b</i> -PMA	Poly(ethylene oxide- <i>block</i> -methyl acrylate)
PFCB	Perfluorocyclobutane
PFSA	Perfluorosulfonic Acid
PI	Polyisoprene
PMDS	Polydimethylsiloxane
PS	Polystyrene
PS- <i>b</i> -PMMA	Poly(styrene- <i>block</i> -methyl methacrylate)
PPV- <i>b</i> -PI	Poly-(2,5-di(2'-ethylhexyloxy)-1,4-phenylenevinylene- <i>block</i> -1,4-isoprene)
PSF	Polysulfone
PTFE	Polytetrafluoroethylene
QENS	Quasielastic Neutron Scattering
RH	Relative Humidity
RMS	Root Mean Square
S	Simons
SAXS	Small Angle X-ray Scattering
SANS	Small Angle Neutron Scattering
SBF	Sharp and Bloomfield Function
SLD	Scattering Length Density
sPEEK	Sulfonated Poly(etheretherketone)

sPPO	Sulfonated Poly(2,6-dimethyl-1,4-phenylene oxide)
sPS	Sulfonated Polystyrene
SSL	Strong Segregation Limit
SAPPSN	Poly(arylene ether nitrile) Dissulfonated Poly(arylene ether sulfone)
TBA	Tetrabutylammonium
TEM	Transmission Electron Microscopy
TMA	Tetramethylammonium
V	Voltage
VFT	Vogel-Fulcher-Tammann
VIM	Vinylimidazole
VT	Virginia Tech
WAXD	Wide Angle X-ray Diffraction
WSL	Weak Segregation Limit
wt	Weight

List of Figures

Figure 1.1. Interference between the waves originating at two scattering centers	3
Figure 1.2. Scattering of a wave of X-rays by a free electron	4
Figure 1.3. Yarusso-Copper's modified hard-sphere model.....	12
Figure 1.4. SAXS system in Hahn Hall 1018, Virginia Tech	14
Figure 1.5. Scattering geometry of Grazing Incident SAXS	17
Figure 1.6. Grazing Incident SAXS experiment setup.....	18
Figure 2.1. Structure of 1100 equivalent weight (EW) Nafion [®] ($n \approx 6.6$)	23
Figure 2.2. Effect of Solution-processing temperature and solvent on the properties of Nafion membrane.....	25
Figure 2.3. SAXS profiles of as-received (AR) dried Nafion 117 (●), solution-processed membrane(▲), and dispersion-cast NRE212CS(■). Drying condition was under vacuum at 70 °C for 12 hr.....	26
Figure 2.4. SAXS profiles of Nafion precursors with various equivalent weight (EW) (a) and tetramethylammonium (TMA ⁺)-form Nafion before and after melt-quenching from 330 °C (b).....	27
Figure 2.5. Correlations between SAXS, DMA, and NMR.....	28
Figure 2.6. Small-angle X-ray scattering (SAXS) profiles of TMA ⁺ (A) and TBA ⁺ -Nafion (B) subjected to thermal annealing at 100 and 200 °C for 10 min. Each plot contains two dimensional SAXS images before (left) and after (right) thermal annealing at 200 °C ...	30
Figure 2.7. Cluster-network model for Nafion membranes developed by Gierke and co-workers.....	32
Figure 2.8. Core-shell Model developed by Fujimura	35

Figure 2.9. Lamellar Model developed by Litt	36
Figure 2.10. Core-Shell Model by Haubold and co-workers	37
Figure 2.11. Change in morphology in Nafion as a function of the volume fraction of water as described by Gebel	38
Figure 2.12. Fibrillar Structure of Nafion developed by Rubatat and co-workers	41
Figure 2.13. Schematic of Nafion worm-like model as described by Kim and co-workers	42
Figure 2.14. Parallel water channel model developed by Schmidt-Rohr and Chen	43
Figure 2.15. Schematic representation of proposed morphology of hydrated Nafion by Elliot and co-workers	44
Figure 2.16. Schematic representation of micelle arrangement within Nafion cast onto different substrates	47
Figure 2.17. Sketch of fibrillar structure of Nafion proposed by Heijden and co-workers	50
Figure 2.18. Variable temperature SAXS of TMA ⁺ (A), TEA ⁺ (B), TPA ⁺ (C), TBA ⁺ (D)-Nafion	51
Figure 2.19. Hydrophilic channel domain alignment modes for uniaxially stretched membranes. The double arrows indicate the stretching direction. a, Extruded, as received. b, Draw ratio 2:1. c, Draw ratio 4:1	52
Figure 3.1. Structure of 1100 equivalent weight (EW) Nafion [®] (n≈6.6)	59
Figure 3.2. SAXS data of Nafion 117CS containing alkali metal ions	65
Figure 3.3. Electron densities of crystalline, amorphous, and ionic regions in Cs ⁺ and Na ⁺ -form Nafion	66

Figure 3.4. Variable temperature SAXS of Na ⁺ -form Nafion	67
Figure 3.5. Electron densities of crystalline, amorphous, and ionic regions in Na ⁺ -form Nafion before and after heating	68
Figure 3.6. Variable temperature SAXS of Cs ⁺ -form Nafion.....	69
Figure 3.7. Electron densities of crystalline, amorphous, and ionic regions in Cs ⁺ -form Nafion before and after heating	70
Figure 3.8. One-dimensional correlation data of Li ⁺ and Na ⁺ -form Nafion	71
Figure 3.9. One-dimensional correlation data of K ⁺ -form Nafion.....	72
Figure 4.1. Structure of 1100 equivalent weight (EW) Nafion [®] (n≅6.6).....	76
Figure 4.2. Solvent-casting cell for synchrotron SAXS studies of <i>in-situ</i> film formation	79
Figure 4.3. SAXS profiles of Nafion dissolved in DMSO solution with various polymer volume fraction (ϕ_p)	81
Figure 4.4. Three-dimensional SAXS profiles for solution processing Nafion in DMSO	83
Figure 4.5. SAXS profiles of Nafion, from gel to dry membrane	86
Figure 4.6. Two-dimensional SAXS plots for solution processing Nafion in DMSO	86
Figure 5.1. Structure of 1100 equivalent weight (EW) Nafion [®] (n≅6.6)	91
Figure 5.2. TMA ⁺ -Nafion films annealed at different temperatures overnight	96
Figure 5.3. TMA ⁺ -Nafion films annealed under 200 °C for different time	98
Figure 5.4. TMA ⁺ -Nafion films annealed for 1m under different temperatures.....	99
Figure 5.5. TBA ⁺ -Nafion films annealed under 90 °C for different time	100

Figure 5.6. GISAXS and SAXS scattering files of TMA ⁺ -Nafion thin film spin coated on silicon(A), and TMA ⁺ -Nafion 117 membrane(B) annealed under 200 °C for different time	102
Figure 5.7. GISAXS and SAXS scattering files of TBA ⁺ -Nafion thin film spin coated on silicon(A), and TBA ⁺ -Nafion 117 membrane(B) annealed under 90 °C for different time	102
Figure 5.8. GISAXS patterns of TMA ⁺ /TBA ⁺ mixture with different ratios under different temperatures	104
Figure 6.1. Structure of 1100 equivalent weight (EW) Nafion [®] (n≈6.6)	109
Figure 6.2. Chemical Structure of sulfonate block copolymer from GM [®]	111
Figure 6.3. Chemical Structure of KF from GM [®]	112
Figure 6.4. AFM images of H ⁺ -PFCB ionomer	115
Figure 6.5. SAXS profiles of different forms of pure PFCB ionomer	116
Figure 6.6. Proposed morphological model for pure PFCB ionomer	117
Figure 6.7. SAXS profiles of PFCB/Kynar Flex blends with variable weight percentages of Kynar Flex in the blends	118
Figure 6.8. Through plane conductivity of PFCB/Kynar Flex blends with variable weight percentages of Kynar Flex in the blends	120
Figure 6.9. Through plane conductivity, FWHM, and distance between the phases vs. KF content in the blends	121
Figure 6.10. Through plane conductivity vs. FWHM, and distance between the phases at the same KF content	122
Figure 6.11. SAXS profiles of different forms of 70/30 PFCB/Kynar Flex blend	124

Figure 6.12. RH Cycling Lifetime vs. Annealing Condition and %KF (80 °C, 0-150%RH)	125
Figure 6.13. SAXS data of 70/30 blends annealed under different temperatures.....	125
Figure 6.14. Δ RH Effect on RH Cycling Lifetimes:BR-10, 70/30 blends	126
Figure 6.15. SAXS data of 70/30 blends under different RH.....	127
Figure 7.1. Schematic drawing of the scattering curve in different q regions	133
Figure 7.2. Chemical structure of copolymer I, II, III, IV.	137
Figure 7.3. Theoretical and experimental SAXS curves of gold colloid	139
Figure 7.4. $I(q)$ vs. q plots for copolymers I, II, III, IV. The fit range includes all of the data points	141
Figure 7.5. Sharp and Bloomfield function fits to the data of Figure 6.5. The fit range includes all of the data points.....	143
Figure 8.1. Some architectures of block copolymers.....	148
Figure 8.2. χN versus fPI diagram for PI-PS diblock copolymers	150
Figure 8.3. Common lattice structure. (a) Lamellae; (b) hexagonal packed cylinders; (c) BCC; (d) FCC; (e) hexagonal close-packed spheres; (f) primitive cubic; (g) double gyroid; (h) double diamond (DD); (i) Pm3n; and (j) Fddd	154
Figure 8.4. Chemical structure of BPSH-BPS MBC monomers	157
Figure 8.5. SAXS profiles of BPSH-BPS MBC ionomer.....	159
Figure 8.6. Chemical structure of 6FPAEB-BPS100 multiblock copolymers.....	161
Figure 8.7. SAXS profiles of 6FPAEB-BPS100.....	162
Figure 8.8. Structures of Multiblock Poly(arylene ether nitrile) Disulfonated Poly(arylene ether sulfone) Copolymers (6FPAEB-BPS100, and 6FPAEB-HQS100).....	164

Figure 8.9. SAXS profiles of 6FPAEB-BPS100 and 6FPAEB-HQS100 multiblock copolymers and 6FPAEB35 random copolymer membrane	166
Figure 8.10. TEM images of 6FPAEB-BPSH (top left: 7K-7K, top right: 15K-15K) and 6FPAEB-HQSH (bottom 7K-7K) multiblock copolymer membranes.....	167
Figure 8.11. Chemical structures of poly(4VIM-b-DEGMEMA-b-4VIM) triblock copolymers.....	169
Figure 8.12. SAXS profiles of scattering intensity versus scattering vector for poly(4VIM-b-DEGMEMA-b-4VIM) triblock copolymers.....	169
Figure 8.13. SAXS profiles with varying volume fraction of phase. (a) vol%(a)=0.42; (b) vol%(a)=0.44; (c) vol%(a)=0.46; (d) vol%(a)=0.48; (e) vol%(a)=0.50; (f) vol%(a)=0.52; (g) vol%(a)=0.54; (h) vol%(a)=0.56; (i) vol%(a)=0.58.....	171
Figure 8.14. AFM phase image in tapping mode and TEM image of 40 wt. % 4VIM-containing ABA triblock copolymer.....	172
Figure 8.15. Chemical structure of PC-PDMS multiblock copolymers	173
Figure 8.16. SAXS profiles for PC-PDMS multiblock copolymers. The SAXS profiles have been vertically shifted to facilitate a comparison of the peak positions.....	174
Figure 9.1 . (A) SAXS pattern from the block copolymer sample after alignment in the electric field. The arrow shows that X-ray beam was orthogonal to the applied field direction. (B) Schema of the orientation of slice planes under the applied electric field	180
Figure 9.2. (A) Theoretical WAXS pattern of a main chain liquid crystalline block copolymer annealed in a magnetic field at elevated temperature. X-ray beam is perpendicular to the magnetic field direction (B) Experimental WAXS pattern clearly	

shows the rod-like structure are aligned parallel to the magnetic field (C) SAXS pattern clearly demonstrates the alignment of the blocks within the block copolymer is perpendicular to the magnetic field direction 182

Figure 9.3. SAXS patterns as a function of the applied magnetic field strength. The magnetic field direction is horizontal with respect to the orientation of the X-ray detector. The curves show the peak intensities and peak shapes of the microdomain scattering at $q=0.07 \text{ \AA}^{-1}$ (triangles) and scattering at $q=0.18 \text{ \AA}^{-1}$ (circles), respectively as a function of field strength 183

Figure 9.4. The average conductivity of 120:1 EO:Li⁺ sample aligned in 5 T magnetic field in two directions under room temperature, with conductivity of nonaligned sample shown for comparison 184

List of Tables

Table 1.1. Neutron scattering length densities for some common polymers and solvents	8
Table 4.1. Detailed information for the SAXS data shown in Figure 4.2	82
Table 5.1. Herman's orientation f vs. annealing temperature for TMA ⁺ -Nafion	97
Table 6.1. Summary of SAXS results in Figure 6.7	119
Table 7.1. Molecular characteristics of copolymer I, II, III, IV	137
Table 7.2. Results from SAXS measurements for copolymers I, II, III, IV	141
Table 7.3. Parameters of SBF for copolymer I, II, III, IV	143
Table 8.1. Peak position ratios of common lattice structures observed in block copolymers	157
Table 8.2. SAXS domain space comparison for the data in Figure 8.5	160
Table 8.3. H ₂ permeability coefficient at 5 atm of BPSH-BPS MBC ionomers	161
Table 8.4. Proton conductivity of 6FBPS0-BPSH100 block copolymer measure in liquid water at 30 °C	164
Table 8.5. SAXS q values and Bragg spacings	171
Table 8.6. Interdomain spacings for selected polymers	176

Chapter 1

Basics of Small Angle X-ray Scattering

1.1 Introduction

Small angle X-ray scattering (SAXS) is a technique to study the structural features of a sample in the nanometer range.¹ Since scattering process always follows reciprocity law, i.e. scattering dimension is inversely proportional to scattering angle, scattering data are always collected at very low angles (typically $0.1 - 10^\circ$) in order to obtain nano-scale structural information. SAXS has been widely applied in polymer science to study the morphology of various polymers.² For instance, the morphology of the benchmark material in fuel cell, Nafion, has been extensively studied by using SAXS.³⁻⁸ Also, researches have been utilizing SAXS to illustrate the structures of proteins,⁹⁻¹¹ DNA,¹²⁻¹⁷ and other biomacromolecules. SAXS has also been applied to study the phase behaviors of polymers.^{18,19} Time-resolved SAXS can help researches to study the crystalline process in real time.^{20,21} In short, one can find applications of SAXS in almost anything between 1 nm and $1 \mu\text{m}$.

1.2 Theory of Small Angle X-ray Scattering

1.2.1 Scattering Vector

Let us consider two scattering centers O and M, and a detector placed in the direction specified by the unit vector \hat{S} at a distance far from the scattering centers.^{2,22} The phase difference between the emitted waves is dependent on the relative positions of these two scattering centers, O and M. Based on the geometry in Figure 1.1, the phase difference can be calculated as

$$\varphi = \frac{2\pi\delta}{\lambda} \quad (1.1)$$

where δ is the path length difference between two X-rays, and it can be calculated as

$$\delta = Mn + mM = -\mathbf{S} \cdot \mathbf{r} + \mathbf{S}_0 \cdot \mathbf{r} = -(\mathbf{S} - \mathbf{S}_0) \cdot \mathbf{r} \quad (1.2)$$

where \mathbf{S}_0 and \mathbf{S} are the unit vectors that represent the directions of the incident and scattered X-rays, respectively, and \mathbf{r} is vector that designates the position of the second scattering center M relative to the first one O. Thus, one can obtain the phase difference written as

$$\varphi = -2\pi \mathbf{s} \cdot \mathbf{r} \quad (1.3)$$

where

$$\mathbf{s} = \frac{\mathbf{S} - \mathbf{S}_0}{\lambda} \quad (1.4)$$

and its magnitude is related to the scattering angle 2θ by

$$s = |\mathbf{s}| = \frac{2 \sin \theta}{\lambda} \quad (1.5)$$

Furthermore, the quantity \mathbf{q} that is related to \mathbf{s} is usually defined as the scattering vector and it can be written as

$$\mathbf{q} = 2\pi \mathbf{s} \quad (1.6)$$

and the magnitude of \mathbf{q} can be expressed as

$$q = \frac{4\pi \sin \theta}{\lambda} \quad (1.7)$$

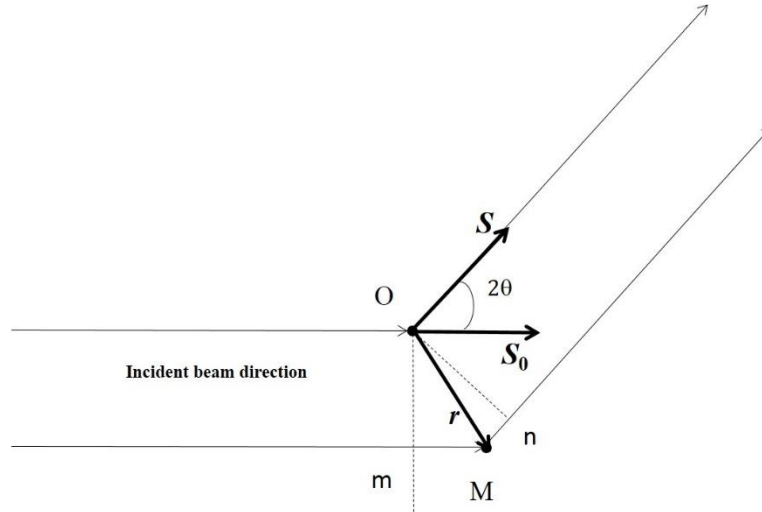


Figure 1.1. Interference between the waves originating at two scattering centers

The vector \mathbf{q} can also be considered as the difference between the scattered wave vector and the incident wave vector, \mathbf{k}' and \mathbf{k} , respectively, where $\mathbf{k}' = 2\pi\mathbf{S} / \lambda$, and $\mathbf{k} = 2\pi\mathbf{S}_0 / \lambda$. The scattering vector \mathbf{q} plays a fundamental role in scattering theory and will be used throughout all the following scattering calculations.

1.2.2 Scattering from one free electron

Consider that a free electron located at O in Figure 1.2^{2,22} is irradiated with a parallel beam of X-rays of intensity I_0 ,

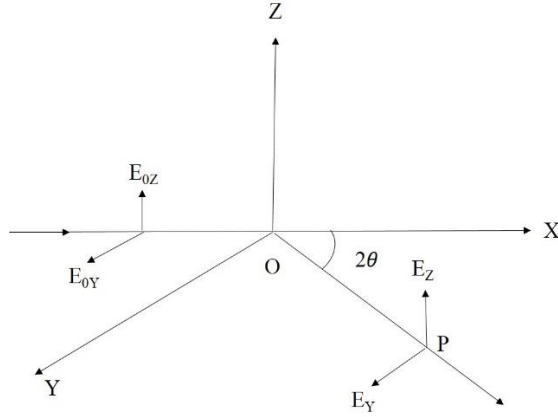


Figure 1.2. Scattering of a wave of X-rays by a free electron

First consider the electric vector of the incident wave be in the OXZ plane, and based on classical electromagnetic theory, the magnitude of this electric vector is given as

$$E_Z = \frac{e^2}{mc^2} \frac{E_{0Z}}{r} \quad (1.8)$$

where E_{0Z} is the magnitude of electric field in the OZ direction, r is the length of OP, $c = 2.998 \times 10^8$ m/s, which is the speed of light, $e = 1.6 \times 10^{-19}$ coulomb, which is the charge of one electron, and $m = 9.10938 \times 10^{-31}$ kg, which is the mass of an electron.

The flux of energy crossing a unit surface per second at position P can be calculated as

$$I_0 \frac{e^4}{m^2 c^4 r^2} \quad (1.9)$$

where $I_0 = E_{0Z}^2$, thus the intensity of scattering in the OP direction per second per unit is given by

$$I_Z = I_0 \frac{e^4}{m^2 c^4} \quad (1.10)$$

Similarly, assuming that the angle between OX and OP is 2θ , and if the electric vector of the incident wave is in the OXY plane, then the scattered intensity can be calculated as

$$I_Y = I_0 \frac{e^4}{m^2 c^4} \cos^2 2\theta \quad (1.11)$$

since the total scattered intensity can be expressed as

$$I_e = k_z I_z + k_y I_y \quad (1.12)$$

and if the incident X-ray beam is not polarized, we have

$$k_z = k_y = 0.5 \quad (1.13)$$

thus,

$$I_e = I_0 \frac{e^4}{m^2 c^4} \frac{1 + \cos^2 2\theta}{2} \quad (1.14)$$

where $e^2 / (mc^2)$ has dimension of length and is defined as the classical radius of an electron, r_e , and it has a numerical value of 2.818×10^{-15} m.

Thus, the scattering length of a free electron, b_e , for unpolarized X-rays can be calculated as

$$b_e = r_e \left(\frac{1 + \cos^2 2\theta}{2} \right)^{1/2} \quad (1.15)$$

and the corresponding scattering cross section is defined as square of the scattering length,

$$\left(\frac{d\sigma}{d\Omega} \right) = b_e^2 = r_e^2 \frac{1 + \cos^2 2\theta}{2} \quad (1.16)$$

1.2.3 Scattering from multiple centers

For a system containing multiple scattering centers, the amplitude of diffraction A as a function of scattering vector \mathbf{q} can be expressed as a summation over all the scattering centers²

$$A(\mathbf{q}) = b_e \sum_{i=1}^n e^{-i\mathbf{q}\cdot\mathbf{r}_i} \quad (1.17)$$

where $A(\mathbf{q})$ is the normalized amplitude of scattered X-rays, and \mathbf{r}_i denotes the position of the i th scattering center. If the structure is defined in terms of the density distribution of all the scattering centers, $n(\mathbf{r})$, instead of individual position, \mathbf{r}_i , and replace summation with integral, we will have

$$A(\mathbf{q}) = b_e \int_V n(\mathbf{r}) e^{-i\mathbf{q}\mathbf{r}} d\mathbf{r} = \int_V \rho(\mathbf{r}) e^{-i\mathbf{q}\mathbf{r}} d\mathbf{r} \quad (1.18)$$

where

$$\rho(\mathbf{r}) = \sum_V b_e n(\mathbf{r}) \quad (1.19)$$

and it is defined as the scattering length density. The $n(\mathbf{r})d\mathbf{r}$ in Eqn. 1.18 is used to represent the total number of scattering centers within a volume V . Now it can be seen that the amplitude $A(\mathbf{q})$ is the Fourier transform of the real-space scattering length density distribution. Thus, the magnitude of scattered intensity can be calculated as the product of A and its conjugate complex A^* ,

$$I(\mathbf{q}) = A(\mathbf{q})A^*(\mathbf{q}) = |A(\mathbf{q})|^2 = \left| \int_V \rho(\mathbf{r}) e^{-i\mathbf{q}\mathbf{r}} d\mathbf{r} \right|^2 \quad (1.20)$$

1.2.4 Contrast Variation

Another way to express the scattered intensity in SAXS is,²

$$I(\mathbf{q}) \propto F(\mathbf{q})S(\mathbf{q})(\Delta\rho)^2 \quad (1.21)$$

which shows that scattered intensity is a function of $F(\mathbf{q})$, $S(\mathbf{q})$, and $\Delta\rho$. $F(\mathbf{q})$ is defined as form factor, which characterizes the shape and size of the particles within the system; $S(\mathbf{q})$ is defined as structure factor, which characterizes the interference between the particles; and $\Delta\rho$ is defined as scattering length density difference between the matrix and the

particles. $F(\mathbf{q})$ and $S(\mathbf{q})$ will be introduced in the following sections, and here we focus on the use of $\Delta\rho$ to facilitate the analysis of scattering data.

The Babinet Principle states that diffraction pattern for an aperture is the same as the pattern for an opaque object of the same shape illuminated in the same manner.²³ This principle indicates that it would be impossible to distinguish scattering of particles (scattering length density ρ_1) from scattering of voids (scattering length density ρ_2) with identical dimension and distribution. The Babinet Principle in SAXS can be explained by using Eqn. 1.21 that if the dimension of the particles keeps unchanged, $F(\mathbf{q})$ will remain unchanged; and if the distribution of the particles are identical, the overall interferences between the particles will keep constant, then $S(\mathbf{q})$ will also remain unchanged. Then $I(\mathbf{q})$ will be identical for these two systems since $(\Delta\rho)^2 = (\rho_1 - \rho_2)^2 = (\rho_2 - \rho_1)^2$ are exactly the same. Thus SAXS cannot determine which of the two phases refers to the scattering of particles and which to scattering of voids.

Thus it is possible for one to manipulate the value of $\Delta\rho$ in order to obtain desired $I(\mathbf{q})$ for different analysis purposes. This technique is called contrast variation method, which is used to separate information on the particle as a whole to determine its structure.²³ Contrast variation method has been widely used in neutron scattering in that the scattering length density differences between hydrogenous solvents and deuterated solvents are very different, which allows one to prepare a mixture of hydrogenous solvent and deuterated solvent to match the scattering length density of the desired particles. Table 1.1 lists the neutron scattering length densities for some common polymers and solvents.²

Table 1.1. Neutron scattering length densities for some common polymers and solvents

<i>Polymer or Solvent</i>	<i>Neutron Scattering Length Density (10^{10}cm^{-2})</i>	
	<i>Hydrogeneous Sample</i>	<i>Deuterated Sample</i>
Water	-0.56	6.4
Cyclohexane	-0.28	6.69
Xylene	0.79	6.04
Toluene	0.94	5.66
Bezene	1.18	5.4
Polyethylene	-0.28	6.71
Polyisoprene	0.27	5.12
Polystyrene	1.41	6.47
Poly(methyl methacrylate)	1.06	7.09

1.2.5 Scattering from Isolated Particles

1.2.5.1 Sphere

In order to study the shape of individual particles, polymers are always dissolved in a very dilute solution in order to remove the interferences between particles.² Consider a simple sphere with a uniform density, ρ_o , in a dilute continuous matrix, we can define the density of this sphere as

$$\rho(r) = \begin{cases} \rho_o & r \leq R \\ 0 & r > R \end{cases} \quad (1.22)$$

where R is the radius of this sphere. Thus we can calculate the scattered intensity as,

$$I(q) = |A(q)|^2 = \rho_o^2 v^2 F(q, R) \quad (1.23)$$

where v is the volume of the sphere, and $F(q, R)$ is the form factor of a sphere and is defined as

$$F(q, R) = \left(\frac{3(\sin qR - qR \cos qR)}{(qR)^3} \right)^2 \quad (1.24)$$

Eqn. 1.24 gives the locations of the minimums of the scattering curve by taking

$$qR = \tan qR \quad (1.25)$$

and it can be calculated that the solutions to Eqn. 1.25 are $qR = 4.493, 7.725, 10.90, 14.07, \dots$. Thus the size of the spheres, R , can be calculated by using the q values determined at the minimum positions in the $I(q)$ vs. q scattering curve.

1.2.5.2 Infinitely Thin Rod

For a thin rod with length L and a as the radius of the cross-section area, if $L \gg a$, then the form factor can be written as²³

$$F(q, L) = 2 \frac{Si(qL)}{(qL)} - 4 \sin^2(qL/2)(q^2 L^2) \quad (1.26)$$

where $Si(x)$ is the sine integral function and it is defined as

$$Si(x) = \int_0^x \frac{1}{t} \sin t dt \quad (1.27)$$

Given the scattering length density, ρ_0 , we can calculate the scattered intensity for an infinitely thin rod in a dilute solution as

$$I(q) = \rho_0^2 v^2 F(q, L) \quad (1.28)$$

1.2.5.3 Infinitely Thin Circular Disk

For a thin circular disk with R as the radius, and d as the thickness of disk, if $R \gg d$, then the form factor can be written as²

$$F(q, R) = \frac{2}{(q^2 R^2)} [1 - J_1(2qR) / (qR)] \quad (1.29)$$

where J_1 is the first order Bessel function²⁴, which is defined as the solution to the Bessel differential equation,

$$x^2 \frac{d^2 y}{dx^2} + x \frac{dy}{dx} + (x^2 - 1)y = 0 \quad (1.30)$$

Thus the scattered intensity can also be written as Eqn. 1.28, with Eqn. 1.30 as the form factor for infinitely thin circular disk.

1.2.6 Scattering from Concentrated Particles

For a system containing concentrated particles, the interferences between particles must be considered. To the interest of this thesis, we would like to study the microstructure of ionomers, such as Nafion,⁷ and it has been proved the existence of ionic aggregations within ionomers.²⁵ Assuming the ionic aggregates to be spherical with radius R ,²⁶ several models have been proposed to calculate the size of these spheres. Guinier and Fouret¹ proposed the following equation for spherically symmetric particles,

$$I(q) = I_e(q) V \frac{1}{v_p} v_0 \rho F(q, R) \left\{ 1 - \frac{1}{v_p} \int_0^\infty [1 - P(r)] \frac{\sin(qr)}{(qr)} (4\pi r^2) dr \right\} \quad (1.31)$$

where $F(q, R)$ is the form factor of a sphere and is defined in Eqn. 1.24. I_e is the intensity scattered by a single electron, ρ is the electron density difference between the spheres and the matrix, v_p is average volume per particle, and v_0 is the volume of the sphere, which is defined as

$$v_0 = \frac{4}{3} \pi R^3 \quad (1.32)$$

$P(r)$ is a probability function that indicates the inter-particle separations, and if assuming that $P(r)$ is independent of the particle concentration,²⁷ it can be defined as

$$P(r) = \begin{cases} 0 & r < 2R \\ 1 & r > 2R \end{cases} \quad (1.33)$$

and this leads to the final equation as

$$I(q) = I_e(q)V \frac{1}{v_p} v_0^2 \rho^2 \Phi^2(qR) \left[1 - \frac{8v_0}{v_p} \Phi(2qR) \right] \quad (1.34)$$

where

$$\Phi(x) = 3 \frac{\sin x - x \cos x}{x^3} \quad (1.35)$$

A more accurate assumption incorporated a finer inter-particle potential function was proposed by Guinier¹ as follows

$$I(q) = I_e(q)V \frac{1}{v_p} v_0^2 \rho^2 \Phi^2(qr) \frac{v_p}{v_p - (2\pi)^{3/2} \varepsilon \beta(q)} \quad (1.36)$$

where ε is a constant very close to one and $\beta(q)$ is used to calculate the interferences between particles, and it can be written as,

$$\beta(q) = \frac{1}{q} \frac{2}{(2\pi)^2} \int_0^\infty r \exp(-\psi(r)/kT) \sin(qr) dr \quad (1.37)$$

where $\psi(r)$ is the inter-particle potential energy function, and

$$\psi(r) = \begin{cases} \infty & r < 2R \\ 0 & r > 2R \end{cases} \quad (1.38)$$

Then integrating Eqn. 1.37 will yield the following equation,

$$I(q) = I_e(q)V \frac{1}{v_p} v_0^2 \rho^2 \Phi^2(qR) \frac{1}{1 + (8v_0/v_p) \varepsilon \Phi(2qR)} \quad (1.39)$$

An even more accurate model was proposed by Yarusso and Copper,²⁸ which is based on the assumption that the interpartical interference between the spherical scattering particles can be characterized as a liquid-like degree of order in the relative positions of

these particles. The model assumes that there exists a closest approach between two particles, defined as $2R_{CA}$, and the ionic aggregates will form a depleted-zone core-shell structure. The core with radius R_1 contains a dense aggregate of ionic groups, and it is surrounded by a shell that is depleted of ions. Later, Eisenberg, Hird and Moore²⁹ proposed a new multiplet-cluster model to explain ionic aggregates in ionomer, which states that the thickness of the shell is postulated to be the order of the persistence length of the polymer. The model proposed by Yarusso and Copper is illustrated in Figure 1.3, and the scattered intensity for this model can be calculated using Eqn. 1.40.

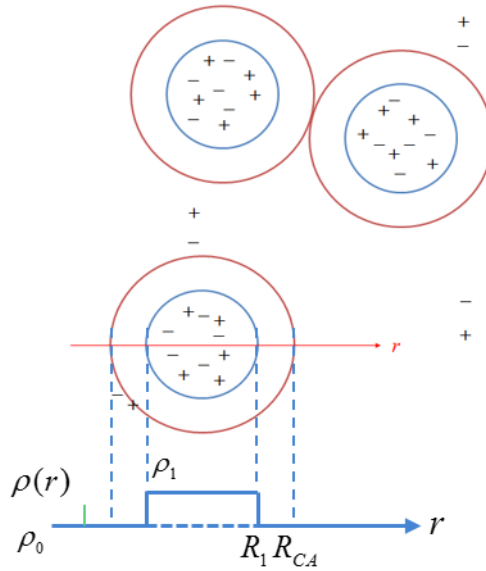


Figure 1.3. Yarusso-Copper's modified hard-sphere model (Adapted with permission from *Macromolecules* **1983**, 16, 1871. Copyright, The American Chemistry Society, 1983)

$$I(q) = I_e(q) V \frac{1}{v_p} v_1^2 \rho_1^2 \Phi^2(qR_1) \frac{1}{1 + \frac{8v_{CA}}{v_p} \Phi(2qR_{CA})} \quad (1.40)$$

where

$$v_1 = \frac{4}{3} \pi R_1^3 \quad (1.41)$$

$$v_{CA} = \frac{4}{3} \pi R_{CA}^3 \quad (1.42)$$

1.2.7 Layout of SAXS system

The in-house SAXS system used to collect SAX data is shown in Figure 1.4, and this system has

- Three pinhole collimation
- A rotating anode emitting X-ray with a wavelength of 0.154 nm (Cu K α)
- Multiple sample chambers for long and mid-range SAXS
- Automated sample changer
- Complete vacuum environment
- User-swappable pinholes and beamstop sets for increased flux at lower resolution
- Photodiode beamstop for intensity measurements and sample absorption correction
- Custom scripting language for automated data collection

Besides SAXS experiments under room temperature, this system can be equipped with Linkam hot stage for experiments under temperatures from -196 °C (temperature of liquid nitrogen) to 600 °C. It can also be equipped with Linkam stretching stage for studies of polymer morphology under orientation. Liquid cell and humidity cell have also been designed for solution samples, and samples under various relative humidity, respectively. Furthermore, it can also be equipped with a grazing incident stage to facilitate studies of surface morphology of various polymers.



Figure 1.4. SAXS system in Hahn Hall 1018, Virginia Tech

1.2.8 Experimental Approach, Absolute Intensity, and Data Collection

A typical two-dimensional SAXS pattern was obtained by using a fully integrated 2D multiwire, proportional counting, gas-filled detector, with an exposure time of 1 hour. SAXS data were analyzed using the SAXSGUI software package to obtain radially integrated SAXS intensity versus scattering vector q , where $q=(4\pi/\lambda)\sin(\theta)$, θ is one half of the scattering angle and λ is the wavelength of X-ray, which is 0.154 nm. The q -range was calibrated using a silver behenate standard. For variable temperature SAXS, samples were heated using a Linkam hot stage positioned in the sample chamber and held for 30 min to equilibrate at a given temperature before data acquisition. An exposure time of 1 hour was used for all samples.

For data analysis, SAXS profiles were commonly plotted as either arbitrary intensity versus q or absolute intensities versus q . Arbitrary intensity units (a.u.) allow shifting the curves vertically to clearly show the peak positions and facilitate the comparison among all the scattering curves, whereas absolute intensities (cm^{-1}) allow quantitative analysis and modeling of the scattering data.

Absolute intensities were obtained by first determining the calibration scale factor.³⁰ This factor was obtained by comparing the scattering intensity of glassy carbon sample and the calibrated intensity of glassy carbon from Argonne Photon Source (APS),³⁰

$$\text{Scale Factor} = \left(\frac{\partial \Sigma}{\partial \Omega} \right)_s \bigg/ \frac{(I_{st}(q) - BG_{st})}{d_{st} T_{st}} \quad (1.43)$$

where d_{st} is the thickness of glass carbon, T_{st} is the transmission of glassy carbon, and BG_{st} is the background scattering. The background scattering was obtained by collecting the scattering data with no sample under high vacuum for the same time as the collection time of the sample.

Thus, absolute intensities of all samples were obtained using the following equation,

$$\text{Absolute intensity} = \left(\frac{\partial \Sigma}{\partial \Omega} \right)_s (q) = \left(\frac{\partial \Sigma}{\partial \Omega} \right)_{st} \frac{(I_s(q) - BG_s)}{d_s T_s} \bigg/ \frac{(I_{st}(q) - BG_{st})}{d_{st} T_{st}} \quad (1.44)$$

where d_s is the thickness of the sample, and T_s is the transmission of the sample.

For solution SAXS, solution sample was sealed in a glass capillary with a diameter of 1.5 mm. The wall thickness of the capillary was 0.01 mm in order to minimize the scattering from the glass. For each solution sample, scattering data of an empty capillary were obtained first. Then the same capillary was filled with pure solvent for another SAXS experiment to collect the scattering data from solvent plus the capillary. Thus, scattering from pure solvent can be calculated as

$$I_{solent} = \frac{I_{solvent+capillary(1)}}{T_{solvent+capillary(1)}} - \frac{I_{capillary(1)}}{T_{capillary(1)}} \quad (1.45)$$

where $T_{capillary(1)}$ and $T_{solvent+capillary(1)}$ are the transmission of the capillary and transmission of the same capillary with pure solvent, respectively.

Similarly, the scattering from the solution that contains polymer can be obtained by using another capillary, and calculated as

$$I_{solent+polymer} = \frac{I_{solvent+polymer+capillary(2)}}{T_{solvent+polymer+capillary(2)}} - \frac{I_{capillary(2)}}{T_{capillary(2)}} \quad (1.46)$$

where $T_{capillary(2)}$ and $T_{solvent+polymer+capillary(2)}$ are the transmission of the capillary and transmission of the same capillary with polymer dissolved in the solvent, respectively.

Thus, scattering from polymer in the solution can be calculated as

$$I_{polymer} = I_{solent+polymer} - I_{solent} \quad (1.47)$$

1.3 Grazing Incident SAXS

Grazing Incident SAXS (GISAXS) is a technique to study the nano-scale structure of objects at the surface. It has been widely used since 1989 to study the surface structures of nanoparticles on substrates. The first study using GISAXS was performed by Levine and coworkers^{31,32} to study the surface structures of thin films. Later on, it has been adapted to study the surface morphology of inorganic (hard) materials,^{33,34} polymers (soft) including block copolymer,^{35,36} ionomer,^{37,38} and so on.

The scattering geometry of GISAXS is illustrated in Figure 1.5, and the experiment setup is shown in Figure 1.6. The beam direction defines the x-axis, and the sample surface defines the xy-plane, while z-axis is defined to be perpendicular to xy-plane.³⁹ For specular

scattering, the condition $\alpha_i = \alpha_f$ should be satisfied. If $\alpha_i \neq \alpha_f$, it will result in diffuse scattering. Given the configuration in Figure 1.5, the scattering vector \mathbf{q} can be written as

$$\mathbf{q} = (q_x, q_y, q_z) \quad (1.48)$$

where

$$q_x = \frac{2\pi}{\lambda} (\cos \psi \cos \alpha_f - \cos \alpha_i) \quad (1.49)$$

$$q_y = \frac{2\pi}{\lambda} (\sin \psi \cos \alpha_f) \quad (1.50)$$

$$q_z = \frac{2\pi}{\lambda} (\sin \alpha_i + \sin \alpha_f) \quad (1.51)$$

where α_i, α_f, ψ are the incident beam angle, exit angle in the Z direction, and out of plane angle, respectively.

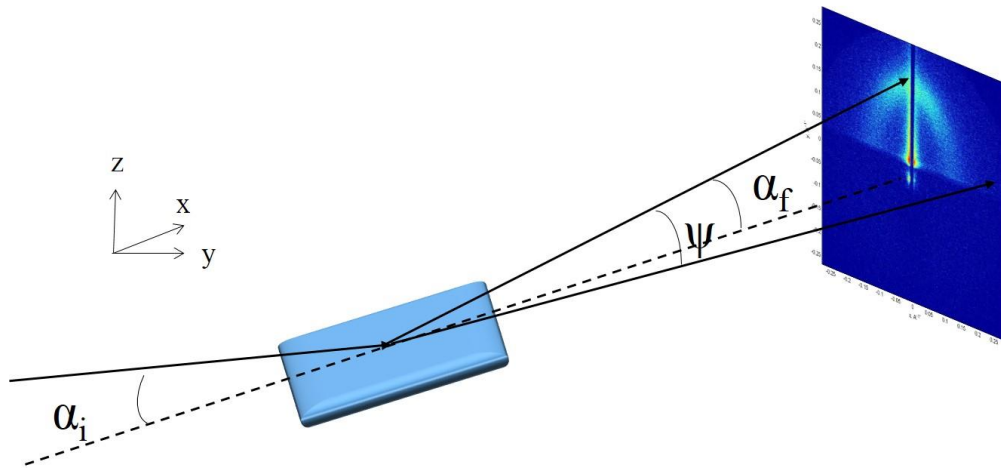


Figure 1.5. Scattering geometry of Grazing Incident SAXS

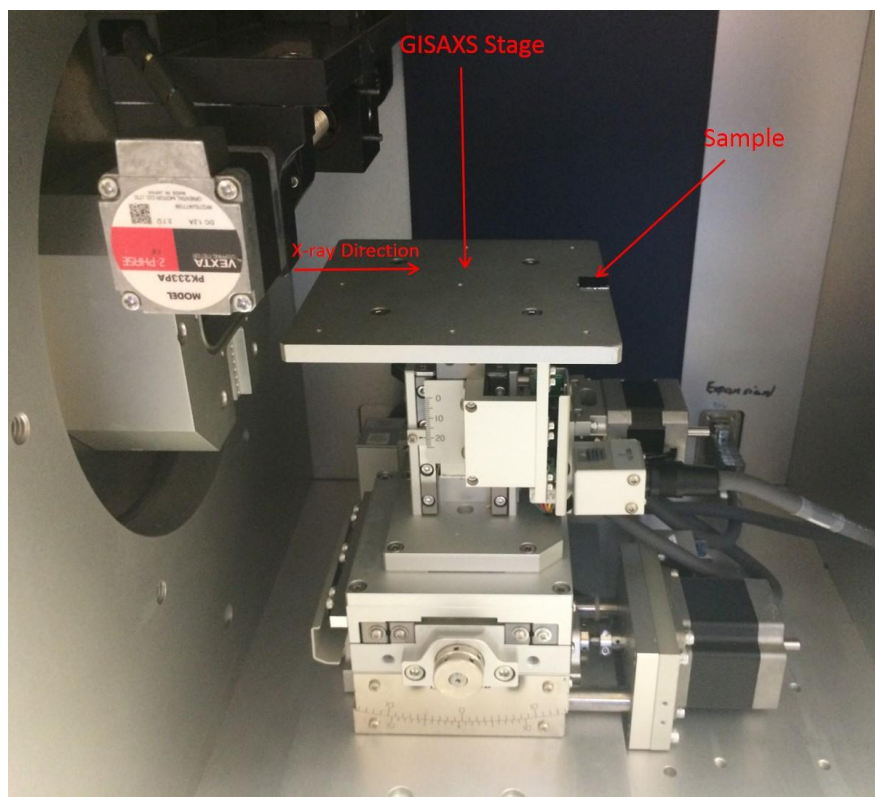


Figure 1.6. Grazing Incident SAXS experiment setup

Since common polymers normally have a smaller refractive index for X-rays compared to vacuum and air, it is possible to achieve total external reflection for the X-ray beams. If the incident angle is chosen to be below the critical angle of the polymer for GISAXS experiment, the wave will penetrate into the film and it is called evanescent in that the intensity of the wave is exponentially damped. This allows one to separate information of near-surface structure from the full film scattering at higher angles.⁴⁰ If the incident angle is chosen to be between the critical angle of the polymer and the substrate, it allows one to obtain information about the dynamics of the surface.⁴¹ If the incident angle is chosen to be larger than the critical angle of the substrate, it allows one to study kinematic of the surface.⁴⁰ A detailed study on surface morphology of Nafion will be introduced in Chapter 5.

1.4 References

- (1) Guinier, A.; Fournet, G. *Small-Angle Scattering of X-rays*; John Wiley & Sons, Inc. Chapman & Hall, Ltd. New York, London, 1955.
- (2) Roe, R.-J. *Methods of X-ray and Neutron Scattering in Polymer Science*; Oxford University Press, Inc. New York, 2000.
- (3) Fujimura, M.; Hashimoto, T.; Kawai, H. *Macromolecules* **1981**, *14*, 1309.
- (4) Moore, R. B.; Martin, C. R. *Macromolecules* **1988**, *21*, 1334.
- (5) Gebel, G. *Polymer* **2000**, *41*, 5829.
- (6) Schmidt-Rohr, K.; Chen, Q. *Nat Mater* **2008**, *7*, 75.
- (7) Mauritz, K. A.; Moore, R. B. *Chemical Reviews* **2004**, *104*, 4535.
- (8) Page, K. A.; Landis, F. A.; Phillips, A. K.; Moore, R. B. *Macromolecules* **2006**, *39*, 3939.
- (9) Bernadó, P.; Mylonas, E.; Petoukhov, M. V.; Blackledge, M.; Svergun, D. *J. Journal of the American Chemical Society* **2007**, *129*, 5656.
- (10) Lipfert, J.; Doniach, S. *Annu. Rev. Biophys. Biomol. Struct.* **2007**, *36*, 307.
- (11) Hura, G. L.; Menon, A. L.; Hammel, M.; Rambo, R. P.; Poole Li, F. L.; Tsutakawa, S. E.; Jenney Jr, F. E.; Classen, S.; Frankel, K. A.; Hopkins, R. C. *Nature methods* **2009**, *6*, 606.
- (12) Rädler, J. O.; Koltover, I.; Salditt, T.; Safinya, C. R. *Science* **1997**, *275*, 810.
- (13) Koltover, I.; Salditt, T.; Rädler, J. O.; Safinya, C. R. *Science* **1998**, *281*, 78.

- (14) Lasic, D. D.; Strey, H.; Stuart, M. C. A.; Podgornik, R.; Frederik, P. M. *Journal of the American Chemical Society* **1997**, *119*, 832.
- (15) Park, S. Y.; Lytton-Jean, A. K. R.; Lee, B.; Weigand, S.; Schatz, G. C.; Mirkin, C. A. *Nature* **2008**, *451*, 553.
- (16) Andersen, E. S.; Dong, M.; Nielsen, M. M.; Jahn, K.; Subramani, R.; Mamdouh, W.; Golas, M. M.; Sander, B.; Stark, H.; Oliveira, C. L. P.; Pedersen, J. S.; Birkedal, V.; Besenbacher, F.; Gothelf, K. V.; Kjems, J. *Nature* **2009**, *459*, 73.
- (17) Das, R.; Mills, T. T.; Kwok, L. W.; Maskel, G. S.; Millett, I. S.; Doniach, S.; Finkelstein, K. D.; Herschlag, D.; Pollack, L. *Physical Review Letters* **2003**, *90*, 188103.
- (18) Vonk, C. *Journal of Applied Crystallography* **1973**, *6*, 81.
- (19) Wu, S. *Polymer Engineering & Science* **1987**, *27*, 335.
- (20) Fougnyes, C.; Damman, P.; Dosiere, M.; Koch, M. *Macromolecules* **1997**, *30*, 1392.
- (21) Hsiao, B. S.; Verma, R. K. *Journal of Synchrotron Radiation* **1998**, *5*, 23.
- (22) Guinier, A. *X-ray diffraction in crystals, imperfect crystals, and amorphous bodies*; W.H. Freeman: San Francisco,, 1963.
- (23) Glatter, O.; Kratky, O. *Small angle x-ray scattering*; Academic Press, 1982.
- (24) Abramowitz, M.; Stegun, I. A. *Handbook of mathematical functions with formulas, graphs, and mathematical tables*; Wiley-Interscience, New York, 1984.
- (25) Pineri, M.; Meyer, C.; Levelut, A. M.; Lambert, M. *Journal of Polymer Science: Polymer Physics Edition* **1974**, *12*, 115.

- (26) Roche, E. J.; Stein, R. S.; MacKnight, W. J. *Journal of Polymer Science: Polymer Physics Edition* **1980**, *18*, 1035.
- (27) Debye, P. *Phys. Z.* **1927**, *28*, 135.
- (28) Yarusso., D. J.; Cooper., S. L. *Macromolecules* **1983**, *16*, 1871.
- (29) A. Eisenberg, B. H., and R. B. Moore *Macromolecules* **1990**, *23*, 4098.
- (30) Fan, L.; Degen, M.; bendle, S.; Grupido, N.; Ilavsky, J. *Journal of Physics: Conference Series* **2010**, *247*, 012005.
- (31) Levine, J. R.; Cohen, J.; Chung, Y.; Georgopoulos, P. *Journal of Applied Crystallography* **1989**, *22*, 528.
- (32) Levine, J. R.; Cohen, J.; Chung, Y. *Surface science* **1991**, *248*, 215.
- (33) Schmidbauer, M.; Wiebach, T.; Raidt, H.; Hanke, M.; Köhler, R.; Wawra, H. *Phys Rev B* **1998**, *58*, 10523.
- (34) Renaud, G. *Surface science reports* **1998**, *32*, 5.
- (35) Lee, B.; Park, I.; Yoon, J.; Park, S.; Kim, J.; Kim, K.-W.; Chang, T.; Ree, M. *Macromolecules* **2005**, *38*, 4311.
- (36) Sun, Z.; Wolkenhauer, M.; Bumbu, G.-G.; Kim, D.; Gutmann, J. *Physica B: Condensed Matter* **2005**, *357*, 141.
- (37) Bass, M.; Berman, A.; Singh, A.; Konovalov, O.; Freger, V. *Macromolecules* **2011**, *44*, 2893.
- (38) Bass, M.; Berman, A.; Singh, A.; Konovalov, O.; Freger, V. *The Journal of Physical Chemistry B* **2010**, *114*, 3784.
- (39) Müller-Buschbaum, P. *Analytical and bioanalytical chemistry* **2003**, *376*, 3.

(40) Müller-Buschbaum, P. In *Applications of Synchrotron Light to Scattering and Diffraction in Materials and Life Sciences*; Gomez, M., Nogales, A., Garcia-Gutierrez, M. C., Ezquerra, T. A., Eds.; Springer Berlin Heidelberg: 2009; Vol. 776, p 61.

(41) Borsali, R.; Pecora, R.; SpringerLink (Online service); Springer Netherlands, Dordrecht, 2008, p v. digital.

2.2 Processing Nafion

Early studies generally used as-received commercial Nafion films. These commercial films were extruded and contained some residual orientation. The residual orientation influenced the small angle scattering data, leading to a vague understanding of the morphology of Nafion. Since 2000s, there has been greater use of dispersion cast films that produce isotropic films.

In the early 1980's, Grot³ detailed a procedure for dissolving Nafion membrane in water/alcohol mixtures at elevated temperature and pressures, and in 1982 Martin and coworkers⁴ developed a procedure for the dissolution of Nafion based on the solvent swelling studies of Yeo and coworkers on 1100 and 1200 EW Nafion.⁵ Later on, Moore and Martin^{6,7} developed “solution processing” procedure to reconstitute the desired mechanical properties of as-received Nafion from recast Nafion. They observed that Nafion cast from alcohol/water solution under low temperature is very brittle and has limit mechanical properties. While adding dimethyl sulfoxide (DMSO) into Nafion dispersion and process under high temperatures will yield improved mechanical properties. (Figure 2.2)

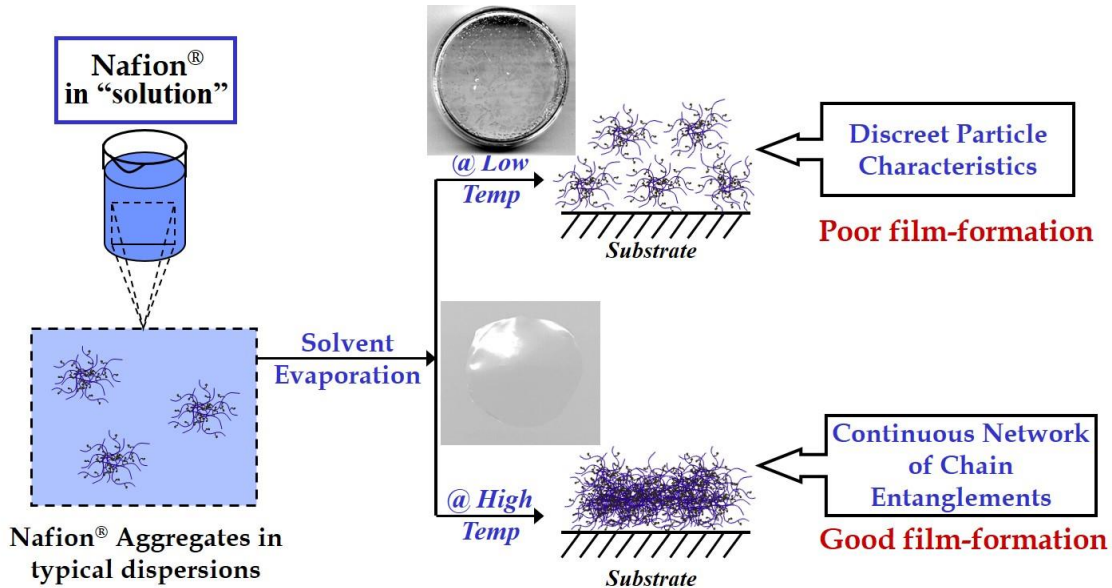


Figure 2.2. Effect of Solution-processing temperature and solvent on the properties of Nafion membrane

In early 2000's, DuPont⁸⁻¹⁰ developed a new solution-casting process, which yields improved water management and mechanical durability features, and since then this new dispersion-cast procedure is widely applied in preparing Nafion membranes. Recently, a detailed study of morphology and properties of solution-cast Nafion membranes from different solvents were performed by Yu and coworkers,^{11,12} which showed that the morphology and properties of cast Nafion are strongly influenced by both solubility parameters and dielectric constants of the solvents.

A further study of the morphology of solution-processing Nafion was performed by Park and coworkers from Prof. R. B. Moore's research group.¹³ Figure 2.3 presents the SAXS profiles from the as-received, dried Nafion 117CS produced by melt-extrusion, membranes prepared by Moore and Martin's solution-processing method, and DuPont's new dispersion-cast method (NRE212CS).⁸⁻¹⁰ For all the three Nafion samples, two peaks

are observed, with the ionic peak appeared at almost the same position. However, the power law for these three different samples are clearly different. A $q^{-1.14}$, $q^{-1.93}$, and $q^{-2.23}$ power law was observed for Nafion 117CS, DuPont's dispersion-cast NRE212CS, and solution-processed, respectively. Furthermore, different EW Nafion precursors showed similar power law while ionic peak totally disappeared (Figure 2.4 (A)). For Nafion under different thermal histories, different power law was also observed (Figure 2.4 (B)). This clearly indicates that processing history will strongly affect the power law, and the power law is dependent not only the ionic region, but also crystalline region.

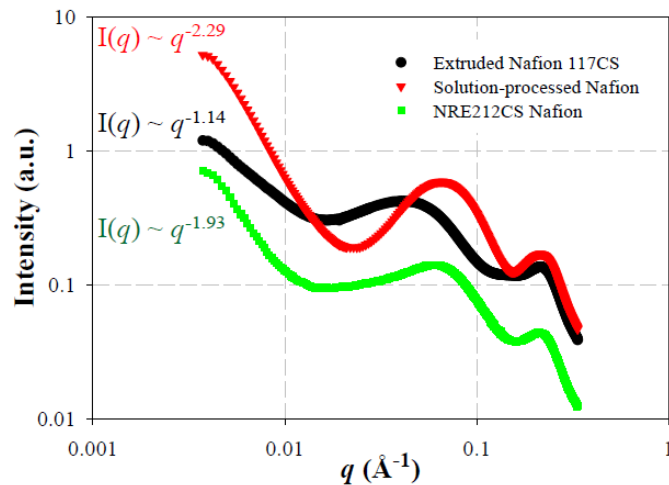


Figure 2.3. SAXS profiles of as-received (AR) dried Nafion 117 (●), solution-processed membrane(▲), and dispersion-cast NRE212CS(■). Drying condition was under vacuum at 70 °C for 12 hr (Data were collected by Jong Keun Park from Prof. R. B. Moore's research group)

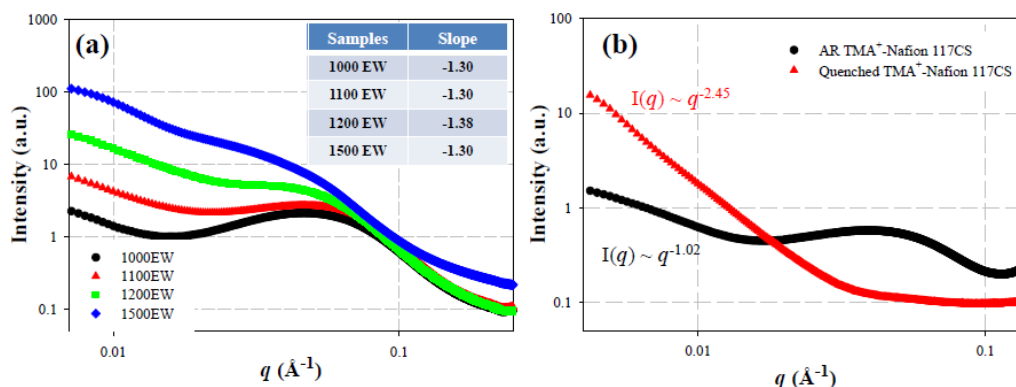


Figure 2.4. (a) SAXS profiles of Nafion precursors with various equivalent weight (EW) and (b) tetramethylammonium (TMA⁺)-form Nafion before and after melt-quenching from 330 °C (Data were collected by Jong Keun Park from Prof. R. B. Moore’s research group)

2.3 Mechanical and Thermal Properties of Nafion

In early studies of Nafion, the sulfonic acid groups within Nafion were generally neutralized with small inorganic counterions that formed strong electrostatic cross-links. These strong electrostatic cross-links prevent further melt processing and thermal disruption of the ionic domain structures. However, the utilization of large tetra alkyl ammonium counterions will greatly reduce electrostatic interactions within the ionic networks, so greater chain mobility and flow can be achieved. The enhanced mobility allows melt processing of Nafion and provides additional methods to probe the thermal and mechanical properties of the ionic domains within Nafion.

Dynamic mechanical measurements show that Nafion has several (α , β , and γ) relaxations.^{15,16} Until recently, there was controversy regarding the molecular origins of these relaxations. By neutralizing Nafion with a series of tetra alkyl ammonium counterions, Page and co-workers^{17,18} showed that the temperature of the mechanical relaxation decreases with increasing counterion size. A correlation of dynamic mechanical analysis (DMA), small angle X-ray scattering (SAXS) and nuclear magnetic resonance

(NMR) results (Figure 5.5) for tetra-methyl ammonium (TMA⁺)-form Nafion clearly showed two distinct relaxations within Nafion. The low-temperature transition, assigned as β -relaxation, is significantly influenced by the strength of the electrostatic interactions, which is assigned as the onset of segmental motion of polymer chains within electrostatic network. While the high-temperature relaxation, assigned as α -relaxation, is attributed to the onset of long-range mobility of chains/side chains as a result of destabilization of electrostatic networks.¹⁷

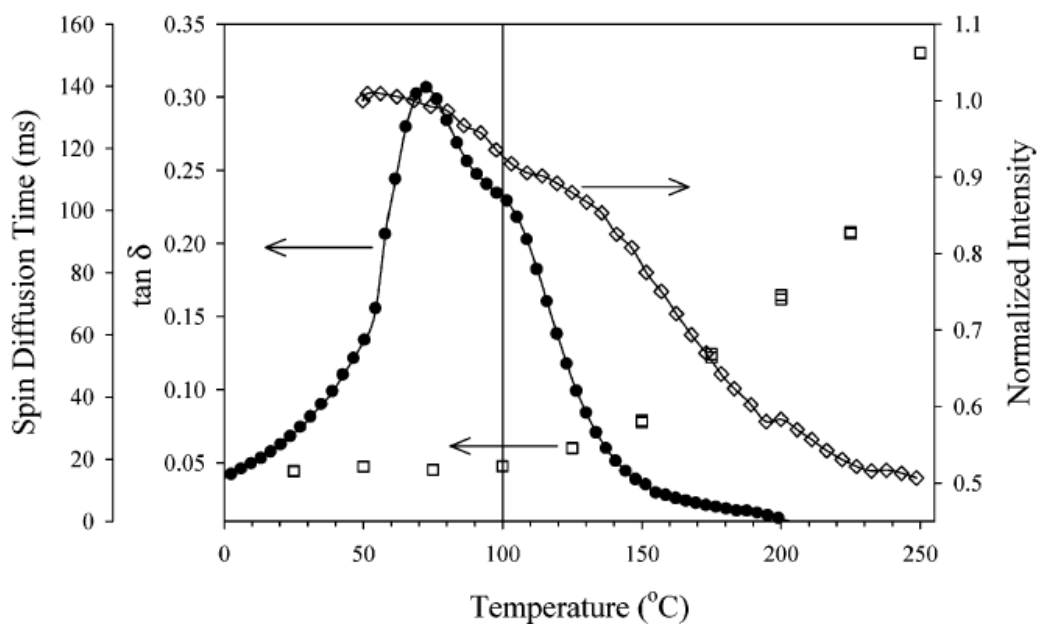


Figure 2.5. Correlations between SAXS, DMA, and NMR (Reprinted with permission from *Macromolecules* **2005**, 38, 6472. Copyright, The American Chemical Society, 2005)

Subsequent work by Osborn and co-workers¹⁹ showed that the β -relaxation is strongly dependent on the composition of the mixture of H⁺-form and tetrabutylammonium (TBA⁺)-form Nafion, while the α -relaxation is relatively composition independent as also demonstrated in the previous works.¹⁷⁻¹⁹ For H⁺ and TBA⁺-Nafion mixture with decreasing amount of TBA⁺, a shift to lower temperatures with a decrease in the magnitude of DMA peak was observed. While α -relaxation temperature does not change too much in either

temperature or DMA peak magnitude. The temperature and magnitude of γ -relaxation remain unchanged, which is in agreement with previous studies¹⁵ that γ -relaxation is related to the local backbone motions. Furthermore, the fit of dielectric data to the Vogel-Fulcher-Tammann (VFT) equation suggests the existence of a large free volume, which indicates a liquid-like state in Nafion at β -relaxation temperature. Thus, β -relaxation is assigned to the genuine T_g of Nafion.¹⁹

Phillips and Moore²⁰ further studied the mechanical and transport properties of various mixtures of sodium and tetrabutylammonium forms of Nafion via solution processing procedure. It shows that α -relaxation of these mixtures-form Nafion follows the Fox equation, while β -relaxation shows a negative derivation. This further supports the assignment of the molecular origins of α and β relaxations in Nafion in the previous studies.¹⁷⁻¹⁹ It was also observed that membranes prepared at a 50/50 Na^+/TBA^+ composition shows an unusually broad ionic peak, and it yields a relatively high proton conductivity after converted back to H^+ -form Nafion, which is attributed to a continuous morphological feature within Nafion. This indicates that processing history and membrane morphology will strongly affect the membrane transport properties.

Park and co-workers²¹ combined the use of SAXS and solid-state NMR to the study of TMA^+ and TBA^+ -forms of Nafion. By annealing TMA^+ and TBA^+ -forms of Nafion under 150 °C and 200 °C, respectively, it was observed that the ionic peak of TMA^+ -Nafion becomes much sharper when annealing under 200 °C compared to that of TBA^+ -Nafion. The NMR data showed that the T_1 relaxation time increases with increasing temperature for TMA^+ -Nafion, while it decreases with increasing temperature for TBA^+ -Nafion. This

is attributed to an improved and well-ordered counterion packing within the ionic domains in TMA⁺-Nafion, which results in the thermally induced ordering effect for TMA⁺-Nafion.

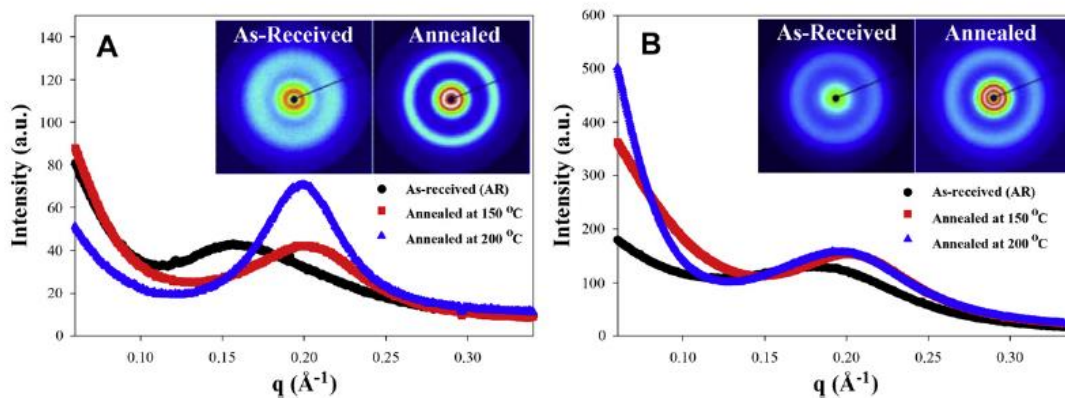


Figure 2.6. Small-angle X-ray scattering (SAXS) profiles of TMA⁺ (A) and TBA⁺-Nafion (B) subjected to thermal annealing at 100 and 200 °C for 10 min. Each plot contains two dimensional SAXS images before (left) and after (right) thermal annealing at 200 °C (Reprinted with permission from *Polymer* **2009**, 50, 5720. Copyright, Elsevier, 2009)

Quasielastic neutron scattering (QENS) was first applied by Page and co-workers²² to directly study the in-situ counterion motions within Nafion membranes. The QENS results showed that the motions of counterions have a length of around 2.5 nm at α -relaxation temperature, which proves that α -relaxation is related to the ion-hopping process. The authors also evidenced that crystallinity of Nafion has little effect on α -relaxation, while both α -relaxation and β -relaxation are strongly dependent on the counterion type. It was also observed that the counterion motion is local when temperature is 60-70 °C below the α -relaxation temperature.

Lee and co-workers²³ studied the effect of annealing temperature on the crystallinity of Nafion cast from an alcohol/water dispersion. They found that annealing above the T_g of Nafion results in an increase in the degree of crystallinity, while the size of ionic clusters

decreases and both O₂ diffusion and solubility increase. However, the authors did not address the effects that the change of the amount of ionic clusters had on the O₂ diffusion and solubility. Another study on the effects of thermal annealing on Nafion was performed by Hensley and co-workers,²⁴ which further proved that annealing at higher temperatures increases crystallinity and leads to greater water and proton self-diffusion. However, the reasons for the increase in water and proton self-diffusion were not fully addressed in this paper. A further study of temperature effect on the crystallinity of solution processing Nafion from DMSO by Moore and co-workers¹³ showed a decrease in the degree of crystallinity with increasing casting temperatures, which will result in lower number of crystallites, but with more uniform sizes. This increase in crystallinity leads to a decrease in the water uptake, which indicates that crystallites in Nafion cannot be settled within the ionic aggregates. Besides various studies on the crystallinity of Nafion, still a detailed explanation on how crystallinity affects the ionic clusters, and thus the properties of Nafion, is lacking.

2.4 Morphological Models Proposed for Nafion

An early model proposed by Gierke and co-workers^{25,26} states that hydrolyzed Nafion exhibits a cluster-network morphology, with spherical ionic clusters that form an inverted micellar structure as shown Figure 2.7. The ionic clusters are separated by an average distance of around 5 nm, and the channel connecting these ionic clusters have an average diameter of 1.0 nm.

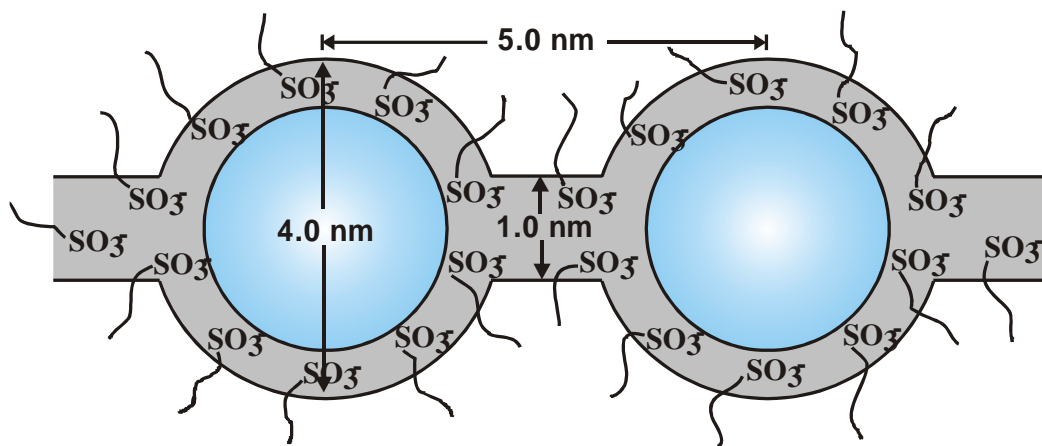


Figure 2.7. Cluster-network model for Nafion membranes developed by Gierke and co-workers (Adapted with permission from the *Journal of Membrane Science* **1983**, *13*, 307. Copyright, Elsevier, 1983)

It was also observed in this work that Nafion neutralized with different counter ions (Li^+ , Na^+ , K^+ , Rb^+ , and Cs^+) almost have identical ionic peak positions as that of H^+ -Nafion, which confirms the existence of ionic aggregations in Nafion. This scattering behavior that ionic peak position will not be affected by the change in counterions in ionomers was addressed by the EHM model proposed by Eisenberg, Hird and Moore.²⁷ It was also observed that the size of the cluster, exchange sites per cluster and water molecules per exchange site are all strongly affected by the amount of water absorbed by Nafion, i.e. they all increase as water content increases. Also, the diameter of the ionic cluster is affected by both the equivalent weight and cation forms of Nafion.

An important aspect of this model lies in that it could explain the transport properties of Nafion. The connections between the ionic clusters will allow the transport of ions and water. The authors also proved the heterogeneity of the ion-clusters distributed within Nafion.

In the meantime, Roche and co-workers^{28,29} investigated the structures of Nafion by utilizing both SAXS and SANS. Nafion shows a scattering peak at 18 nm corresponding

to the distance between crystallites within Nafion, which was also observed in Gierke's studies.²⁵ The amount of water has a huge effect on the morphology of Nafion. At high water content, i.e., more than 15 wt%, Nafion exhibits a two-phase morphology with hydrophilic phase containing ionic groups and water and hydrophobic phase containing perfluorocarbon backbones. On the other hand, at low water content Nafion exhibits a three-phase morphology, which contains crystalline phase, ionic phase, and inhomogeneous matrix phase. Consistent with Gierke's work,²⁵ they also observed the shift to lower angle in the first scattering maxima and increase in scattering intensity with increasing water content. It also needs to point out that their research excludes the possibility of hard-sphere model to explain the morphology of Nafion due to the existence of ionic peak at even very low water content. Instead they proposed that the morphological model of Nafion should include structure attributed to the internal ionic aggregates.

The origins of the scattering maxima of Nafion in SAXS were also studied by Fujimura and co-workers^{30,31} in early 1980s. Besides sulfonate Nafion, carboxylate Nafion was also studied in this work. Two scattering maxima in SAXS plots, with one at around 0.07 nm^{-1} and the other at around 0.3 nm^{-1} were also observed, which is consistent with Gierke's studies.²⁵ Combining SAXS and WAXS data, the first maxima at lower q value was confirmed to be related to the crystallinity of Nafion. It was also observed that the degree of crystallinity of Nafion increases with increasing equivalent weight. The crystalline peak in SAXS shifts to lower q value with increasing equivalent weight, indicating an increase in interlamellar spacing, which may be due to an increase in the thickness of the crystallites.

More studies were focused on the ionic peak which appears at larger q value by Fujimura and co-workers, where they assumed that the ionic cluster has a core-shell

structure as shown in Figure 2.8. This is similar to the core-shell model proposed for ionomer by MacKnight, Stein, and co-workers,^{32,33} but is not in favor of the two-phase model for ionomer by Cooper and coworkers.³⁴ It is observed that ionic scattering maxima will shift to larger q value as temperature is increased, which indicates a decrease in the intercluster distance. This maxima will also shift to larger q value with decreasing equivalent weight. The authors attributed this as a balance between electrostatic interactions between ionic domains and thermodynamic energy needed for elastic deformation, which is consistent with Gierke's work.²⁵ From swelling studies on the ionic regions, the ionic maxima at $q=0.2 \text{ nm}^{-1}$ was observed to shift to smaller q value with an increase in the magnitude of the scattering intensity. This indicates an increase in the size of the core with more water, and thus the electron density of the core is reduced, which leads to an increase in the magnitude of the scattering intensity. Furthermore, the results from uniaxial stretching Nafion showed that the microscopic deformation is much less than the macroscopic deformation, which supports their core-shell model for the ionic clusters within Nafion.

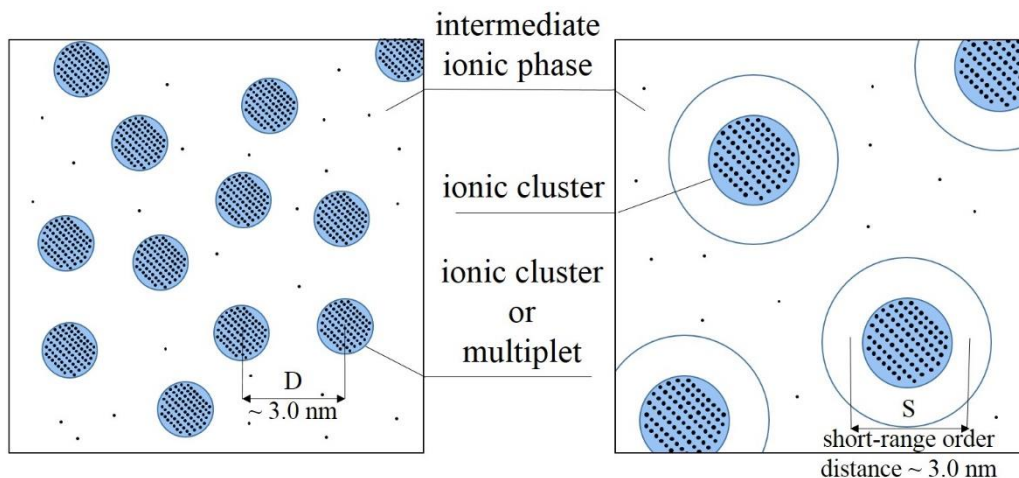


Figure 2.8. Core-shell Model developed by Fujimura (Adapted with permission from *Macromolecules* **1981**, *14*, 1309. Copyright, The American Chemical Society, 1981)

In 1990, Dreyfus and co-workers³⁵ proposed a local-order model for Nafion. This model states that the micelles containing ionic aggregates and water are ordered on a short range, with each micelle surrounded by four neighbor micelles, and it exhibits a gas-like disorder on a long range. Based on this mode, a radial distribution $P(r)$ was proposed and incorporating this $P(r)$ into the form factor yields a well-defined equation to calculate scattered intensity. This model was applied in the later studies by Gebel and Lambard³⁶ on water-swollen Nafion. They demonstrated that the local order model would fit the experimental data well within a q range between 0.3 and 2 nm^{-1} . For even smaller q range, the scattering curve could be fit by using Debye-Bueche model,^{37,38} which considers both the electron density fluctuations and heterogeneously dispersed ionic clusters, and it gives a correlation length of 8 nm . Furthermore, USAXS data were also collected for Nafion 117, 115, and 112, which allows them to get a long-range correlation length of 350 nm within Nafion.

A lamellar model was proposed for Nafion by Litt³⁹ in 1997 as shown in Figure 2.9. Based on the SAXS data of swollen Nafion from Gierke and co-workers,²⁵ the proposed model could give a value of the volume of Nafion per equivalent weight very close to the experimental value. Thus the model could be used to explain the swelling behavior of Nafion.¹



Figure 2.9. Lamellar Model developed by Litt

Haubold and co-workers⁴⁰ proposed a sandwich-like model based on fitting SAXS data. This model (Figure 2.10) states that the core containing water/methanol is sandwiched by two shells that consist of side chains and ionic groups. The sandwiches are distributed in the matrix with the cores forming channels for protons to travel through. The thickness of the shell increases as volume% of methanol in water increases, while the core decreases in thickness. With 100% water, the shell and core have a thickness of 2.8 and 3.5 nm, respectively. While with 100% methanol, the shell and core have a thickness of 4.9 and 1.2 nm, respectively. The total thickness of the sandwich is about 6 nm. The model could be applied to explain the swelling behaviors and transport properties of Nafion. However, it ignores the effect of crystallinity from the fluorocarbon backbone.

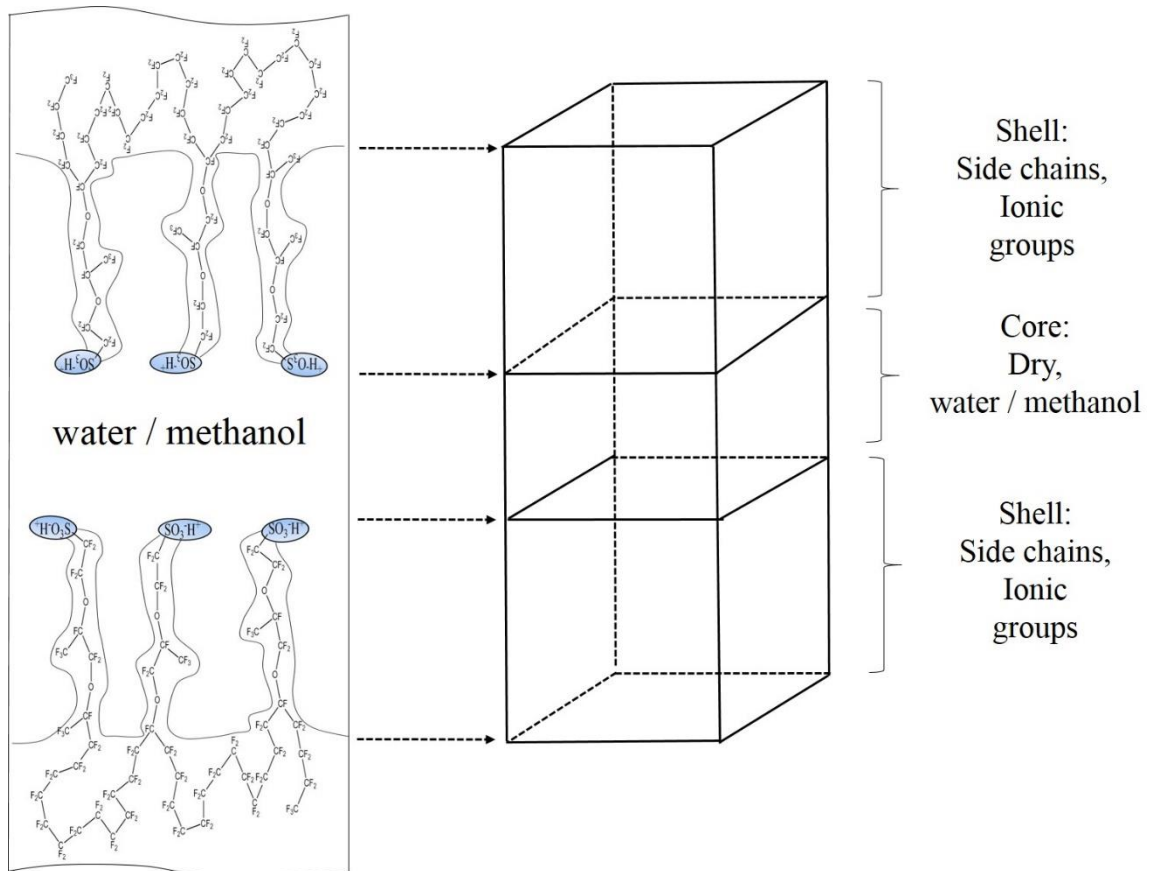


Figure 2.10. Core-Shell Model by Haubold and co-workers (Adapted with permission from *Polymer* **2000**, *41*, 5829. Copyright, Elsevier, 2000)

Gebel⁴¹ fully studied the morphological evolution of Nafion from dry state to solution state by means of SAXS and SANS. This paper was aiming at further understanding the morphological transition of core-shell structure in solid state membrane to reverse micellar structure in swollen membranes, and finally to the rod-like structure in PFSI solutions that was evidenced in the previous studies.^{42,43} Figure 2.11 shows the morphological development of Nafion with increasing water content.

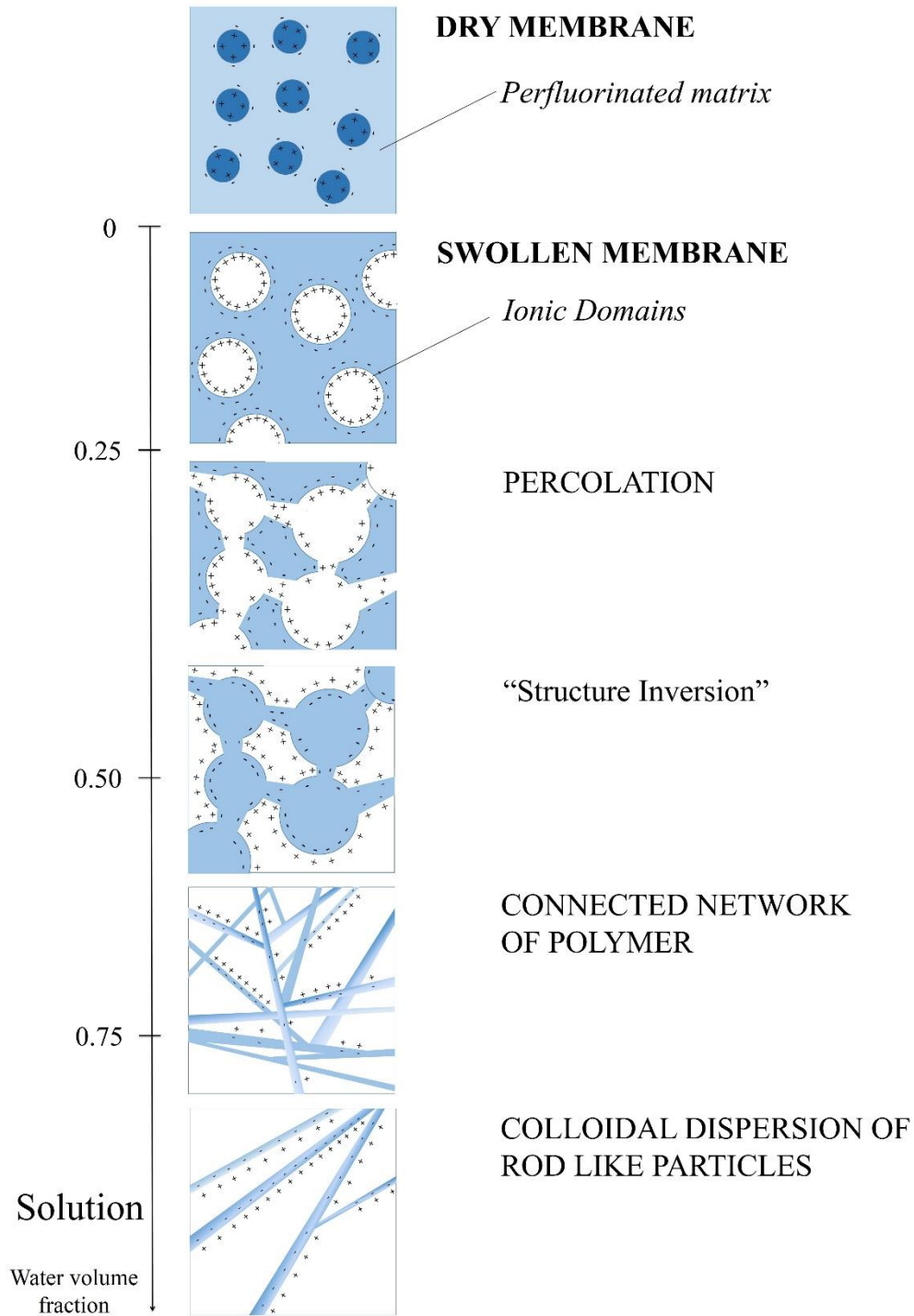


Figure 2.11. Change in morphology in Nafion as a function of the volume fraction of water as described by Gebel (Adapted with permission from *Polymer* **2000**, *41*, 5829. Copyright, Elsevier, 2000)

At dry state, the ionic aggregates form spherical ionic clusters that have an average diameter of 1.5 nm, and these clusters are separated by an average distance of 2.7 nm. At low water content, the size of the ionic clusters becomes a little larger, i.e., 2 nm in diameter, and average distance between the clusters is close to 3 nm. Due to separations between the ionic clusters at low water content, the ionic conductivity is still extremely low. As water content increases, the hydrophilic ionic clusters will start to swell with an increase in diameter from 2 nm to 4 nm. Water now is acting as a plasticizer and facilitates the percolation process of the ionic clusters. This results in a decrease in the number of ionic clusters, but an increase in the number of ionic aggregates per cluster. A large increase in ionic conductivity was observed when the volume fraction of water is larger than 0.2 ($\phi_w > 0.2$), which indicates that the ionic aggregates have formed percolation pathway. As water volume fraction is between 0.3 and 0.5, the diameter of the spherical ionic clusters increases to 5 nm, and these clusters are connected with water-filled cylinders that are dispersed in the polytetrafluoroethylene (PTFE) matrix. The morphology of Nafion under this water content is similar to the cluster-network model proposed by Gierke and co-workers.²⁵ As water volume fraction goes above 0.5, the structure undergoes an inversion in that the cylinders or rod like structures will be filled with the hydrophobic phase of polymer aggregates, and they are dispersed in the water matrix. As water content continues to increase, the rod-like networks continue to swell, and finally yield a colloidal dispersion of rod-like particles in water, with a radius of around 2.5 nm.

Rubatat and co-workers⁴⁴⁻⁴⁶ proposed a fibrillar nanostructure of Nafion by studying the structure of oriented Nafion using SAXS and SANS. Based on SAXS, TEM and AFM data of Nafion solution, they were able to confirm the existence of cylindrical aggregates

as evidenced by Loppinet and co-workers.^{42,43} The cylindrical aggregates have a diameter between 3 and 5 nm. The use of USAXS data allowed them to study the density fluctuations at large scales similar to what have been done by Gebel and Lambard.³⁶ By using Debye-Bueche model,^{37,38} a correlation length of 8 nm was also obtained. The USAXS data of Nafion with different water content clearly showed two distinct scattering behaviors. At low q region, a clear q^{-1} power law was observed, indicating the existence of rod-like particles within Nafion. While at high q region, a clear q^{-4} power law was observed, which suggests a sharp interface between the crystalline regions and the ionic regions.

By plotting the characteristic (Bragg) distances using $d=2\pi/q^*$, the authors also observed the two microscopic swelling regimes as evidenced by Gebel.⁴¹ They also found that under different polymer volume fractions, the scattering data follow different power laws. When polymer volume fraction is lower than 0.6, it follows a $q^{-0.5}$ power law, and at a higher polymer volume fraction ($\phi_p > 0.6$), a q^{-1} power law was observed that is in agreement with previous studies.^{30,31,39} The authors proposed a ribbon-like structure to explain the change in power law at $\phi_p=0.6$, and the ribbons have a cross-sectional thickness of 2 nm and a width of 8 nm.

Furthermore, they found that the degree of crystallinity in Nafion film does not change upon stretching, and the ratio of the orientation factors between the ionic region and crystalline region upon stretching does not keep constant (i.e. 1), indicating the spherical network model is not accurate in describing the structure of Nafion. On the other hand, these results suggest an elongated polymeric aggregate model. These fibrillar structures have a mean diameter of 3.5 nm, and a minimum length of 80 nm (Figure 2.12).

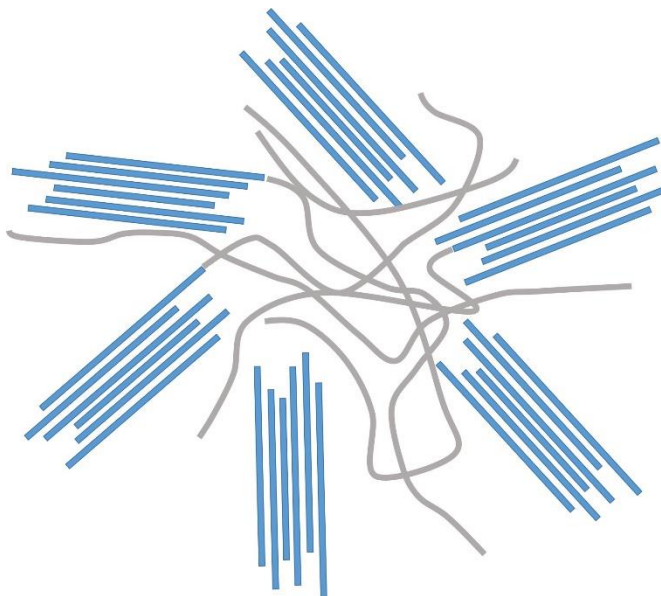


Figure 2.12. Fibrillar Structure of Nafion developed by Rubatat and co-workers (Adapted with permission from *Macromolecules* **2004**, 37, 7772. Copyright, The American Chemical Society, 2004)

Based on the in-situ vapor sorption small angle neutron scattering (iVSANS) experiments on Nafion membranes, Kim and co-workers¹⁴ proposed a fringed-micelle model, which consists of cylindrical bundles of linear segments aligned in parallel, with the bulky side chains excluded from the crystalline phase. In this study, a q^{-1} power law was also observed as has been evidenced in the other studies.^{30,31,39,44-46} This model can explain the kinetics and water uptake within Nafion membranes. Although both the fibrillar structure proposed by Rubatbat²⁰⁻²² and the fringe-micelle model contain rod-like structures, they are different in that the fibrillar model suggests the crystallites within Nafion stay in the rods, while fringed-micelle model has the crystallites dispersed not only in the ionic domains, but also in the whole matrix. What also needs to be pointed out here is that this work also showed processing affects the morphology of Nafion. The q^{-1} power law was only observed for excluded Nafion, while solution cast Naifon and thicker Nafion membrane did not show this power law. Furthermore, crystallinity was not observed in

melt-extruded membrane, which may indicate the q^{-1} power law could be a scattering result from all the three regions within Nafion, i.e. the ionic, crystalline and amorphous regions. However, this study does not give a sound explanation for the relationship between ionic domains and crystalline regions.

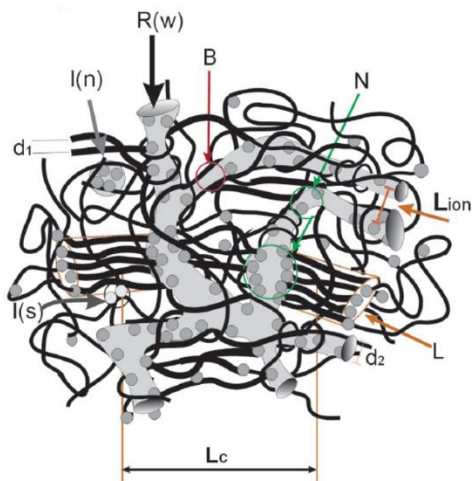


Figure 2.13. Schematic of Nafion worm-like model as described by Kim and co-workers (Adapted with permission from *Macromolecules* **2006**, 39, 4775. Copyright, American Chemical Society, 2006)

In 2007, Schmidt-Rohr and Chen⁴⁷ proposed a parallel cylindrical water nanochannel model based on simulations of SAXS curves carried out by numerical Fast Fourier transformation (FFT) of scattering densities. In this model, inverted-micelle cylinders containing ionic aggregates are surrounded by partially hydrophilic side chains. A simulation curve for Nafion with 20 volume% of water was obtained based on the model proposed in Figure 2.14, and the simulation data could match the experimental SAXS data obtained by Rubatat and co-workers.⁴⁸ The model states that the inverted-micelle cylindrical water channels contain ionic aggregates inside, and are surrounded by PTFE backbones outside. (Figure 2.14.a) These water channels have an average diameter of 2.4 nm, and the crystallites are aligned parallel to the water channels, with cross-sections of

around 25 nm². Also, these inverted-micelle cylinders are mostly hexagonal packed as shown in Figure 2.14.b. The crystallites are dispersed within Nafion matrix, and the calculated volume percentage of crystallinity is 13%, which is in the range of the degree of crystallinity within Nafion.³⁰ The thickness of these crystallites is between 2 and 5 nm with an aspect ratio from 1 to 1.8. The authors also tried to simulate SAXS data based on various other models as introduced in the previous sections,^{14,25,44-46} but all of them failed to satisfy the experimental data. This model could also explain the reason why diffusion of water in Nafion is faster than other sulfonated ionomers, and it is due to the large size of the water channels within Nafion.

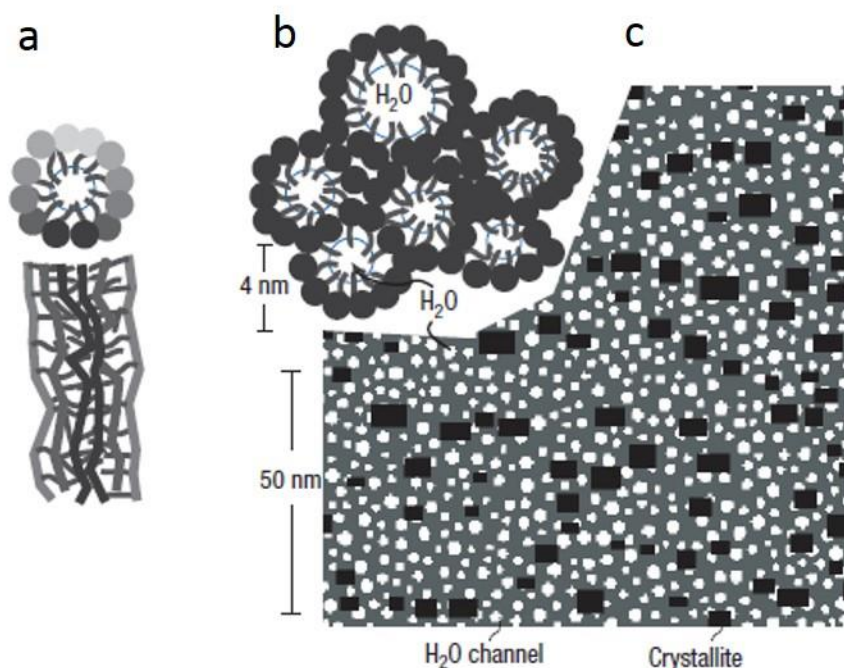


Figure 2.14. Parallel water channel model developed by Schmidt-Rohr and Chen (Reprinted with permission from *Nature Materials* **2008**, 7, 75. Copyright, Nature Publishing Group, 2008)

Recently, Elliott and co-workers⁴⁹ combined statistical (Maximum Entropy Modeling, MaxEnt) analysis of SAXS data and thermodynamic (Dissipative Particle Dynamics, DPD)

simulations to study the complex morphology of Nafion. The use of MaxEnt algorithm does not require any information on the charge distribution, which is more accurate in the sense of computational simulation. Another feature of this method is that no direct fitting parameters would be required for simulation. The authors suggested a bicontinuous network of ionic clusters embedded in a matrix of fluorocarbon chains within Nafion. This model is consistent with the results from both unoriented and oriented studies, and it also demonstrated that hydrocarbon rich regions will contain the lowest amount of ionic aggregations. This proposed morphology in Nafion also allows for redistributing sulfonic acid groups between adjacent ionic aggregates to achieve morphological rearrangement, which may indicate a dynamic rearrangement of ionic groups within Nafion.

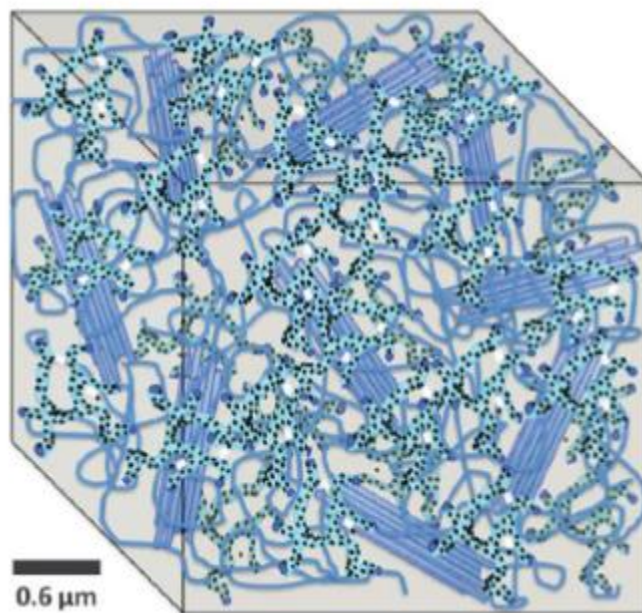


Figure 2.15. Schematic representation of proposed morphology of hydrated Nafion by Elliot and co-workers (Reprinted with permission from *Soft Matter* **2011**, 7, 6820. Copyright, RSC Publishing, 2011)

2.5 Surface Morphology of Nafion

Recently, several groups have been studying surface structure of Nafion films using neutron reflectometry,⁵⁰ grazing incident SAXS (GISAXS),⁵¹⁻⁵³ and atomic force microscopy (AFM).⁵⁴⁻⁶⁰ These studies mainly focus on the orientations of nano-channels in Nafion under different processing procedures or environmental conditions.

Umeda and coworkers^{30,31} observed different morphologies of Nafion when stored in water and alcohols by using AFM. In water, ionic clusters of size 7-15 nm are clearly observed. They also observed that alcohols would not strongly interact with sulfonic acid groups, but on the other hand they would solvate the fluoroether side chain.^{54,55} For the first time Hiesgen and coworkers^{57,58} were able to apply electrochemical AFM (EC-AFM) to visualize the ionic channels on the surface of Nafion. Later on, they⁵⁹ visually observed the existence of inverted micelles, which is in agreement with the model proposed by Schmidt-Rohr and Chen.⁴⁷ However, a super-structure of clusters on different length scales was also observed in their images, which is consistent with the model proposed by Elliot and coworkers.⁶¹ Takimoto and coworkers⁶⁰ observed that under low relative humidity (RH) ionic clusters within Nafion would expand gradually with increasing water content, and ionic clusters would aggregate with each other under high RH. They concluded that this morphological rearrangement would result in the high proton conductivity of Nafion even at low RH since hydrophilic domains would rearrange to maintain the connections of network of conductive paths within Nafion. Kwon and co-workers⁵⁶ measured the proton conductivity of Nafion membranes as a function of annealing time under different annealing temperatures and observed an initial increase and then decrease in conductivity. They concluded that annealing above T_g of Nafion would induce the parallel orientation of

ionic channels on the surface of Nafion membrane and further annealing would result in a chemical decomposition of Nafion. However, the changes in conductivity with increasing annealing temperatures were not addressed in this work.

Dura and co-workers⁵⁰ utilized neutron reflectometry measurements to show the existence of multilamellar interfacial structures in Nafion. The reflectivity data were fitted to determine the depth profile of neutron scattering length density (SLD), which can be used to obtain the components of Nafion film at different depth. When Nafion was cast onto silicon surfaces, alternating water-rich and Nafion-rich multilamellar structures were observed. On the other hand, when Nafion was cast onto Au or Pt surfaces, only one single water-rich lamellar was formed at the interface between Nafion and the substrate. This is attributed to the low affinity of Au and Pt surfaces to the sulfonic acid/water phase. Furthermore, a residual interfacial structure was also observed even when Nafion was heated up to 150 °C, which may be due to the existence of water that is either trapped at the interface or tightly bounded to the residual structures. This study also showed that the thickness of the lamella and the number of layers are affected by humidity, which will both increase with increasing humidity.

In a later study utilizing GISAXS, Bass and co-workers^{51,52} found that the orientation of Nafion micelles would be affected by both the substrate and phase of water. By varying the incident angle, they were able to study the alignment of micelle bundles. When Nafion films casted onto C18-caped Si and native Si were treated in vapor, the vertical direction of both ionic scattering rings from GISAXS was enhanced at an incident angle below the critical angle of Nafion. This suggests that the micelle bundles are parallel aligned to the substrate, which is in agreement with the results from Dura and co-workers.⁵⁰ When the

film casted onto C18-capped Si substrate was treated in water, the ionic scattering ring was clearly weakened in the vertical direction when the incident angle was below the critical angle of Nafion. This indicates that the bundles of Nafion are self-aligned perpendicular to the substrate, but the micelles would partially disentangle and one end of the film would be capped or anchored when contacting with water as shown in Figure 2.16.

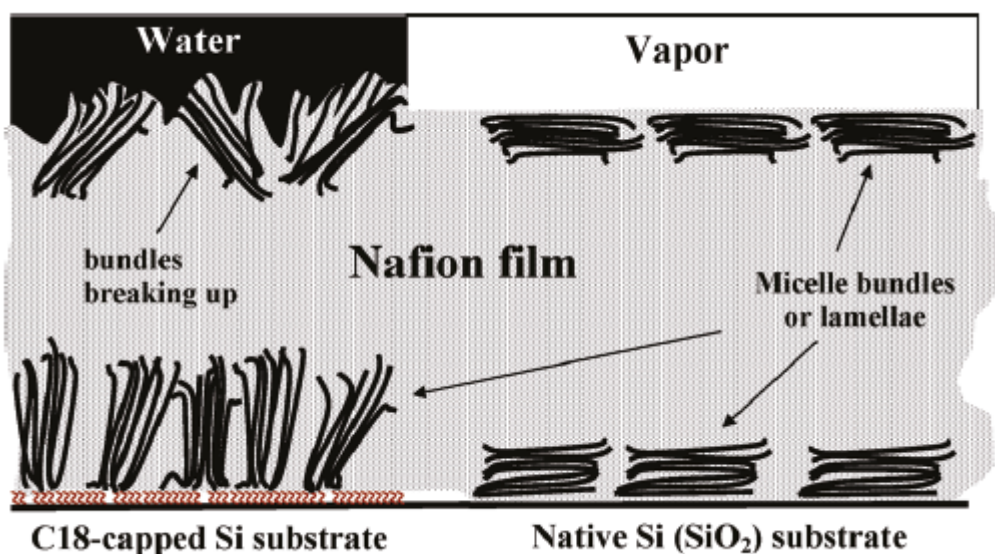


Figure 2.16. Schematic representation of micelle arrangement within Nafion cast onto different substrates (Reprinted with permission from *Macromolecules* **2011**, *44*, 2893. Copyright, The American Chemistry Society, 2011)

Modestino and co-workers⁵³ utilized in-situ GISAXS to correlate surface morphology with water uptake within Nafion. GISAXS scattering patterns showed a clear anisotropic behavior for Nafion film cast onto a hydrophobic substrate, which indicates the hydrophilic domains are oriented parallel to the substrate. When Nafion film was cast onto a hydrophilic substrate, isotropic scattering behavior was observed, which suggests that hydrophilic domains are randomly distributed. When swelling with water, a larger change for the ionic peak was observed when Nafion film was cast onto hydrophilic substrate compared to that cast onto hydrophobic substrate, which indicates film cast onto

hydrophilic substrate undergoes a faster swelling of water. This is attributed to the fact that the parallel morphology will resist the water uptake in that drastic morphological reorganization would have to be required for more swelling. Furthermore, they showed that the degree of crystallinity increases after annealing, and the formation of these crystallites upon annealing would stay near the substrate interface, which could lead to a decrease in water uptake.

2.6 Studies of Nafion via Orientation

The studies of Nafion using “as-received” extruded Nafion and dispersed-cast Nafion provide much information of the morphology and properties of Nafion. Moreover, orientation of polymers has been proved be an important process to provide a means to produce and control anisotropic morphology and properties of polymers. This process has also been widely applied by many researchers to facilitate the morphological and property studies of Nafion.^{18,31,46,62,63}

Fujimura and co-workers³¹ performed SAXS studies on oriented Nafion with draw ratios from 1.0 to 1.5. They calculated the macroscopic expansion (λ_d) and microscopic expansion (λ_b) by using $\lambda_d = d / d_0$ and $\lambda_b = l / l_0$, respectively, where d and d_0 are the spacing calculated using Bragg’s equation, respectively, and l and l_0 are the dimensions of the membrane under wet state and dry state, respectively. The results showed that λ_d tends to increase with increasing λ_b at the polar zone, but it tends to decrease at the equatorial zone. Since affine deformation models would predict a larger variation of λ_d with λ_b , it suggests that the two-phase model would not be an accurate model to describe the

morphology of Nafion in that this model would have a λ_d value close to that of λ_B . Instead, it would suggest a core-shell model where the core that contains ionic aggregates may be more rigid than the matrix containing PTFE backbone of Nafion, and this would result in a variation of λ_d with λ_B .

Heijden and co-workers^{45,64} studied the orientation of drawn Nafion at both molecular and mesoscopic scales. The changes in the peak positions of crystalline, ionic, and amorphous peaks were obtained as a result of drawing between 1.0 and 2.7. The results showed that α , which is the ratio between crystalline and ionomer orientation factors, increased from 0.5 to 1.0 as a function of draw ratio. The authors also calculated the Herman's orientation parameter, f , to facilitate the analysis. The values of α close to 1 and f close 1 were achieved at large draw ratios, which indicates complete orientation of the scattering particles parallel to the director. These results showed that Gierke's cluster-network model with spherical clusters within Nafion²⁵ could not be accurate in describing Nafion structure. Instead, a fibrillar structure could be developed to better describe the experimental observations (Figure 2.17). This model shows that Nafion has elongated aggregates, and they form bundles which are randomly distributed within Nafion. Under small draw ratio, the bundles will rotate and align along the drawing direction. When the draw ratio is large, the individual aggregates may slide or disentangle from each other.

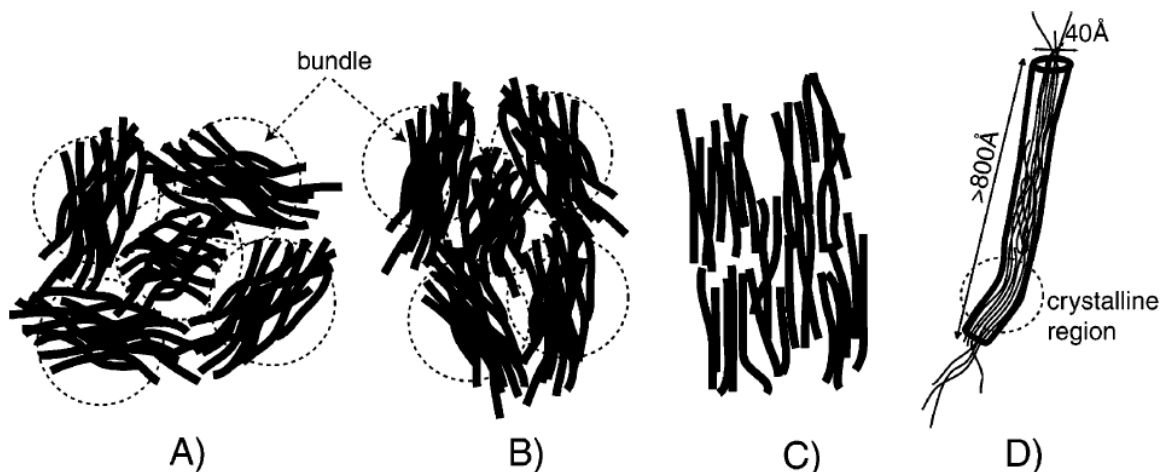


Figure 2.17. Sketch of fibrillar structure of Nafion proposed by Heijden and co-workers (Reprinted with permission from *Macromolecules* **2004**, *37*, 5327. Copyright, The American Chemistry Society, 2004)

Upon stretching Nafion, Page and co-workers¹⁸ studied the thermal relaxation behavior of oriented Nafion films using SAXS under different temperatures. By neutralizing Nafion with various alkylammonium counterions (TMA^+ , TEA^+ , TPA^+ , TBA^+), the authors were able to study the effect of the size of counterions on the thermal relaxation of Nafion. It was observed that the Herman's orientation, f , increases with decreasing counterion size, which demonstrates that smaller counterions would result in higher degrees of orientation. Besides, variable temperature SXAS data for all the different counterion forms Nafion plotted as scattering intensity vs. azimuthal angle showed strong equatorial ionic scattering peaks at 90° and 270° ; which indicates stretching induces strong alignment of ionic domains along the stretching direction. Furthermore, it was observed that the strong anisotropic morphologies would change to isotropic morphologies with increasing temperatures, and the transition appears at a lower temperature for TBA^+ -Nafion. This suggests that larger counterion will facilitate greater chain mobility,¹⁷ which will result in a larger degree of stress relaxation.

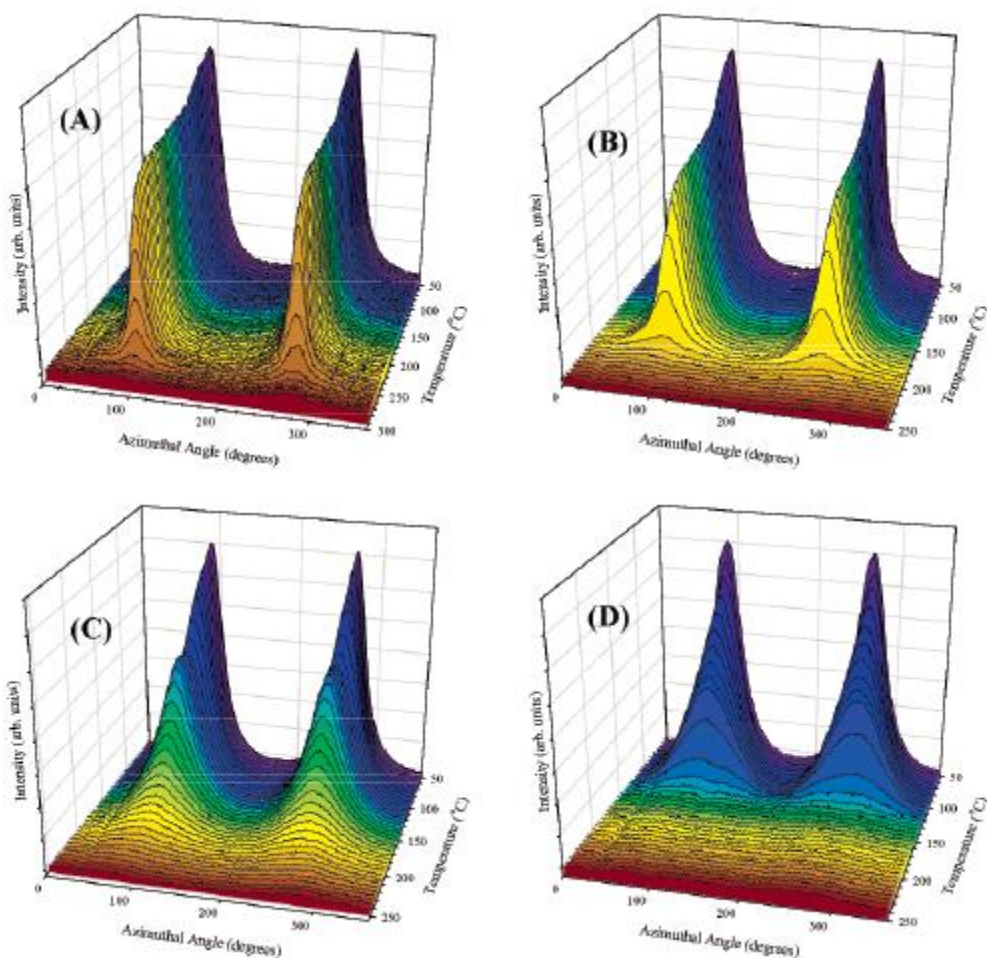


Figure 2.18. Variable temperature SAXS of TMA⁺(A), TEA⁺(B), TPA⁺(C), TBA⁺(D)-Nafion (Reprinted with permission from *Macromolecules* **2006**, *39*, 3939. Copyright, The American Chemistry Society, 2006)

Drawing experiments on Nafion were also performed by Rubatat and Diat⁴⁶ to further investigate the stretching effect on Nafion structure. The authors applied contrast variation technique in SANS by swelling Nafion with mixture of D₂O and H₂O in order to cancel the structure factor, and the results showed that the scattering objects were oriented even without significant orientation, which is in agreement with the elongated polymeric aggregates model.^{44,48} Furthermore, the authors assumed a model with oriented cylinders and simulated SAXS data based on this model. The simulated data showed that the intensity and peak position of the ionic peak are in agreement with the experimental results. These

results demonstrate that Nafion have fibrillar structures with an average diameter of 3.5 nm.

Combining SAXS and NMR data, Li and co-workers⁶² suggested that stretching membrane would not affect the nanometer-scale channel dimensions or the boundary at domain interface. Based on ²H-NMR results, diffusion anisotropy increases significantly with increasing draw ratio. However, the average diffusions in both parallel and perpendicular directions are the same for all draw ratios as a function of water content. These results indicate that stretching will not result in a significant change in the size of the hydrophilic channel or channel connectivity. Furthermore, a linear relationship between diffusion anisotropy and the degree of partial ordering of ²H₂O molecules was observed, which further demonstrates that stretching will not affect junction and defect densities. Thus, macroscopic stretching will only cause a change in the orientation of existing ionic aggregates without a perturbation in size, shape, spatial distribution, or connectivity of nano-scale hydrophilic domains. (Figure 2.19)

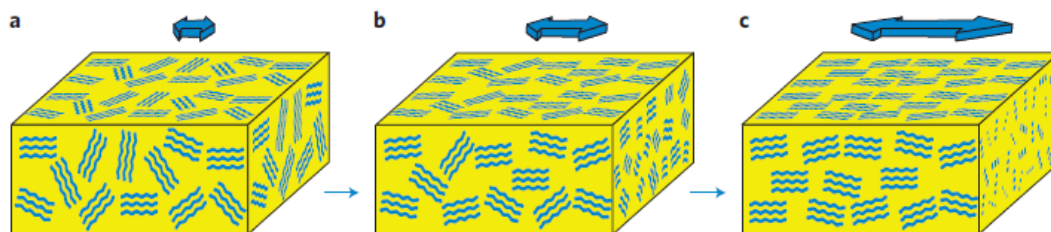


Figure 2.19. Hydrophilic channel domain alignment modes for uniaxially stretched membranes. The double arrows indicate the stretching direction. **a**, Extruded, as received. **b**, Draw ratio 2:1. **c**, Draw ratio 4:1 (Reprinted with permission from *Nat Mater* **2011**, *10*, 507. Copyright, Nature Publishing Group, 2011)

A followed-up study by Park and co-workers⁶³ revealed the relationship between the morphology and transportation properties of Nafion. The Herman's orientation parameters were calculated for both dry Nafion and hydrated Nafion under stretching, which showed

no significant difference between dry and hydrated Nafion. This indicates that swelling process will not result in a significant morphological change within Nafion. It was also observed that scattering invariant does not change significantly upon stretching, which suggests that stretching will not lead to a change in the degree of overall phase separation. Furthermore, it was observed that orientation enhances water transport and proton conductivity only in the direction parallel to the draw direction, but reduces them in the perpendicular direction, which indicates a reorientation of elongated hydrophilic channels upon stretching.

2.7 Further Study of Nafion and Nafion-like Materials

While there has been significant progress for understanding the morphology of Nafion during the past decades, still there are several outstanding questions need to be answered. For instance, detailed studies on the crystalline morphology in Nafion need to be performed in order to reveal the roles of crystallinity in the properties and performance of Nafion membranes, and the interactions between crystallites and ionic domains. Moreover, methods to manipulate the crystalline order within Nafion also need to be developed. Besides, the effect of water on the transport properties needs to be further addressed. These remaining questions still need further studies on the morphology and structure-property relationship of Nafion.

2.8 References

- (1) Mauritz, K. A.; Moore, R. B. *Chemical Reviews* **2004**, *104*, 4535.
- (2) Mohsen, S.; Kwang, J. K. *Smart Materials and Structures* **2001**, *10*, 819.

- (3) Grot, W. G.; COMPANY, E. I. D. P. D. N. A., Ed. 198 Vol. EP0066369
- (4) Martin, C. R.; Rhoades, T. A.; Ferguson, J. A. *Analytical Chemistry* **1982**, *54*, 1639.
- (5) Yeo, R. S. *Polymer* **1980**, *21*, 432.
- (6) Moore, R. B.; Martin, C. R. *Analytical Chemistry* **1986**, *58*, 2569.
- (7) Moore, R. B.; Martin, C. R. *Macromolecules* **1988**, *21*, 1334.
- (8) C. Preischl, P. H., A. Hahn 2001; Vol. 6,291,091 B1.
- (9) Curtin, D. E.; Lousenberg, R. D.; Henry, T. J.; Tangeman, P. C.; Tisack, M. E. *Journal of Power Sources* **2004**, *131*, 41.
- (10) Joachim Köhler, K.-A. S., Sandra Wittpahl, Manfred Diehl 2002; Vol. 2002/0064593 A1 (30 May, 2002).
- (11) Lin, H.-L.; Yu, T. L.; Huang, C.-H.; Lin, T.-L. *Journal of Polymer Science Part B: Polymer Physics* **2005**, *43*, 3044.
- (12) Ma, C.-H.; Yu, T. L.; Lin, H.-L.; Huang, Y.-T.; Chen, Y.-L.; Jeng, U. S.; Lai, Y.-H.; Sun, Y.-S. *Polymer* **2009**, *50*, 1764.
- (13) Park, J. K., Virginia Tech, 2009.
- (14) Kim, M.-H.; Glinka, C. J.; Grot, S. A.; Grot, W. G. *Macromolecules* **2006**, *39*, 4775.
- (15) Kyu, T.; Hashiyama, M.; Eisenberg, A. *Canadian Journal of Chemistry* **1983**, *61*, 680.
- (16) Yeo, S. C.; Eisenberg, A. *Journal of Applied Polymer Science* **1977**, *21*, 875.
- (17) Page, K. A.; Cable, K. M.; Moore, R. B. *Macromolecules* **2005**, *38*, 6472.

- (18) Page, K. A.; Landis, F. A.; Phillips, A. K.; Moore, R. B. *Macromolecules* **2006**, *39*, 3939.
- (19) Osborn, S. J.; Hassan, M. K.; Divoux, G. M.; Rhoades, D. W.; Mauritz, K. A.; Moore, R. B. *Macromolecules* **2007**, *40*, 3886.
- (20) Phillips, A. K.; Moore, R. B. *J Polym Sci Pol Phys* **2006**, *44*, 2267.
- (21) Park, J. K.; Spano, J.; Moore, R. B.; Wi, S. *Polymer* **2009**, *50*, 5720.
- (22) Page, K. A.; Park, J. K.; Moore, R. B.; Garcia Sakai, V. *Macromolecules* **2009**, *42*, 2729.
- (23) Lee, K.; Ishihara, A.; Mitsushima, S.; Kamiya, N.; Ota, K.-i. *Journal of The Electrochemical Society* **2004**, *151*, A639.
- (24) Hensley, J. E.; Way, J. D.; Dec, S. F.; Abney, K. D. *Journal of Membrane Science* **2007**, *298*, 190.
- (25) Gierke, T. D.; Munn, G. E.; Wilson, F. C. *Journal of Polymer Science: Polymer Physics Edition* **1981**, *19*, 1687.
- (26) Hsu, W. Y.; Gierke, T. D. *Journal of Membrane Science* **1983**, *13*, 307.
- (27) A. Eisenberg, B. H., and R. B. Moore *Macromolecules* **1990**, *23*, 4098.
- (28) Roche, E. J.; Stein, R. S.; MacKnight, W. J. *Journal of Polymer Science: Polymer Physics Edition* **1980**, *18*, 1035.
- (29) Roche, E. J.; Pineri, M.; Duplessix, R.; Levelut, A. M. *Journal of Polymer Science: Polymer Physics Edition* **1981**, *19*, 1.
- (30) Fujimura, M.; Hashimoto, T.; Kawai, H. *Macromolecules* **1981**, *14*, 1309.
- (31) Fujimura, M.; Hashimoto, T.; Kawai, H. *Macromolecules* **1982**, *15*, 136.

- (32) Kao, J.; Stein, R. S.; MacKnight, W. J.; Taggart, W. P.; Cargill, G. S. *Macromolecules* **1974**, *7*, 95.
- (33) W. J. Macknight, W. P. T., and R. S. Stein *H. Polymer Sci. : Symposium* **1974**, *45*, 113.
- (34) Marx, C. L.; Caulfield, D. F.; Cooper, S. L. *Macromolecules* **1973**, *6*, 344.
- (35) Dreyfus, B.; Gebel, G.; Aldebert, P.; Pineri, M.; Escoubes, M.; Thomas, M. *J. Phys. France* **1990**, *51*, 1341.
- (36) Gebel, G.; Lambard, J. *Macromolecules* **1997**, *30*, 7914.
- (37) Bueche, P. D. a. A. M. *Journal of Applied Physics* **1949**, *20*, 518.
- (38) Debye, P.; Anderson, H. R.; Brumberger, H. *Journal of Applied Physics* **1957**, *28*, 679.
- (39) Litt, M. *Polymm. Prepr.* **1997**, *38*, 80.
- (40) Haubold, H. G.; Vad, T.; Jungbluth, H.; Hiller, P. *Electrochimica Acta* **2001**, *46*, 1559.
- (41) Gebel, G. *Polymer* **2000**, *41*, 5829.
- (42) Loppinet, B.; Gebel, G.; Williams, C. E. *The Journal of Physical Chemistry B* **1997**, *101*, 1884.
- (43) Loppinet, B.; Gebel, G. *Langmuir* **1998**, *14*, 1977.
- (44) Rubatat, L.; Gebel, G.; Diat, O. *Macromolecules* **2004**, *37*, 7772.
- (45) van der Heijden, P. C.; Rubatat, L.; Diat, O. *Macromolecules* **2004**, *37*, 5327.
- (46) Rubatat, L.; Diat, O. *Macromolecules* **2007**, *40*, 9455.
- (47) Schmidt-Rohr, K.; Chen, Q. *Nat Mater* **2008**, *7*, 75.

- (48) Rubatat, L.; Rollet, A. L.; Gebel, G.; Diat, O. *Macromolecules* **2002**, *35*, 4050.
- (49) Elliott, J. A.; Wu, D.; Paddison, S. J.; Moore, R. B. *Soft Matter* **2011**.
- (50) Dura, J. A.; Murthi, V. S.; Hartman, M.; Satija, S. K.; Majkrzak, C. F. *Macromolecules* **2009**, *42*, 4769.
- (51) Bass, M.; Berman, A.; Singh, A.; Konovalov, O.; Freger, V. *The Journal of Physical Chemistry B* **2010**, *114*, 3784.
- (52) Bass, M.; Berman, A.; Singh, A.; Konovalov, O.; Freger, V. *Macromolecules* **2011**, *44*, 2893.
- (53) Modestino, M. A.; Kusoglu, A.; Hexemer, A.; Weber, A. Z.; Segalman, R. A. *Macromolecules* **2012**, *45*, 4681.
- (54) Affoune, A. M.; Yamada, A.; Umeda, M. *Langmuir* **2004**, *20*, 6965.
- (55) Affoune, A. M.; Yamada, A.; Umeda, M. *Journal of Power Sources* **2005**, *148*, 9.
- (56) Kwon, O.; Wu, S.; Zhu, D.-M. *The Journal of Physical Chemistry B* **2010**, *114*, 14989.
- (57) Aleksandrova, E.; Hiesgen, R.; Eberhard, D.; Friedrich, K. A.; Kaz, T.; Roduner, E. *ChemPhysChem* **2007**, *8*, 519.
- (58) Aleksandrova, E.; Hiesgen, R.; Friedrich, K. A.; Roduner, E. *Physical Chemistry Chemical Physics* **2007**, *9*, 2735.
- (59) Hiesgen, R.; Aleksandrova, E.; Meichsner, G.; Wehl, I.; Roduner, E.; Friedrich, K. A. *Electrochimica Acta* **2009**, *55*, 423.

- (60) Takimoto, N.; Wu, L.; Ohira, A.; Takeoka, Y.; Rikukawa, M. *Polymer* **2009**, *50*, 534.
- (61) Elliott, J. A.; Hanna, S.; Elliott, A. M. S.; Cooley, G. E. *Macromolecules* **2000**, *33*, 4161.
- (62) Li, J.; Park, J. K.; Moore, R. B.; Madsen, L. A. *Nat Mater* **2011**, *10*, 507.
- (63) Park, J. K.; Li, J.; Divoux, G. M.; Madsen, L. A.; Moore, R. B. *Macromolecules* **2011**, *44*, 5701.
- (64) Heijden, P. C. v. d.; Rosa, A. d. l.; Gebel, G.; Diat, O. *Polymers for Advanced Technologies* **2005**, *16*, 102.

in Nafion. In 1981, Gierke and co-workers described a cluster-network model,¹ which was later improved by Roche and co-workers.³ Later on several other models, such as core-shell model by Fujimura and co-workers,^{4,5} lamellar model by Litt,²² sandwich-like model by Haubold and co-workers,⁹ were also proposed to explain the morphology of Nafion. In 2002, a rod-like aggregates model was proposed by Rubatat and co-workers.^{11,13,23,24} Kim and co-workers developed a fringed-micelle model to explain the crystalline order within the proximity of the ionic domains.²¹ Applying fast Fourier transformation, Schmidt-Rohr and Chen described a parallel cylindrical water-channel model of Nafion to correlate the SAXS and SANS data with the morphological behavior and transport properties in Nafion.¹⁷ Recently, Elliott and co-workers²⁵ combined statistical analysis of SAXS data and thermodynamic simulations to study the complex morphology of Nafion and proposed a model of bicontinuous network of ionic clusters embedded in a matrix of fluorocarbon chains within Nafion.

Contrast variation (CV) technique is mostly applied in neutron scattering due to the large difference in scattering length densities between hydrogen and deuterium,²⁶ which makes it possible to use a mixture of light and heavy water to match the scattering length densities of most polymer systems. This technique has been applied by some researchers to study the morphology of Nafion in solution by SANS.^{3,11} Roche and co-workers³ were able to demonstrate the presence of two phases in Nafion membranes that were hydrated. Using different mixtures of protonated and deuterated methanol to prepare H⁺-form Nafion solutions for SANS experiments, Rubatat and co-workers¹¹ demonstrated the existence of elongated polymeric aggregates in Nafion.

Contrast variation technique has also been applied in SAXS to study the internal structure of polymer latexes in solution.^{27,28} However, this technique is seldom applied to study the morphology of Nafion solution using SAXS due to the difficulty in finding a mixture of a specific solvent and water to match the electron densities of different regions within Nafion. Furthermore, there also lacks a systematic study of applying CV technique to probe the morphology of Nafion in solid state using SAXS.

The present study applies CV technique to better understand the morphological features observed in Nafion membranes in solid state using SAXS. Using different inorganic counterions provides a means to alter the electron densities of ionic domains and allows matching of the electron densities of the amorphous phase or the crystalline phase, which would make either the crystalline peak or the ionic peak indiscernible to X-rays. Utilizing variable temperature SAXS, the scattering behavior of Nafion due to changes in electron densities was studied in more details. One-dimensional correlation function was applied to show the significance of using CV method to study the morphology of Nafion, and it gives a long periodicity of around 9 nm within Nafion.

3.2 Experimental Section

3.2.1 Materials

Nafion 117CS (1100EW, sulfonic acid form) was purchased from E. I. DuPont Company. Lithium hydroxide, sodium hydroxide, potassium hydroxide, rubidium hydroxide, and cesium hydroxide were obtained from Aldrich Chemical Co., and used as-received without further purification.

3.2.2 Preparation of Neutralized Perfluorinated Sulfonic Acid (PFSA) Membranes

Nafion 117CS membranes were cleaned by refluxing them in HNO₃ (8M) for 2 h to remove impurities, then washed with deionized (DI) water three times, and boiled in DI water for 1 h. The cleaned membranes were first immersed in 1 M either lithium hydroxide, sodium hydroxide, potassium hydroxide, rubidium hydroxide or cesium hydroxide solution overnight at room temperature, then heated up to 70 °C for 2 h. Membranes were washed and then boiled in DI water for another hour. Finally all membranes were dried at room temperature between Kim wipes for an hour and placed in a vacuum oven for 12 h at 70 °C.

3.2.3 SAXS Instrument

SAXS experiments were performed using a Rigaku S-Max 3000 3 pinhole SAXS system, equipped with a rotating copper anode emitting X-rays with a wavelength of 0.154 nm (Cu K_α). Two-dimensional SAXS patterns were obtained using a fully integrated 2D multiwire, proportional counting, gas-filled detector, with an exposure time of 1 hour. All SAXS data were analyzed using the SAXSGUI software package to obtain radially integrated SAXS intensity versus scattering vector q , where $q=(4\pi/\lambda)\sin(\theta)$, θ is half of the scattering angle and λ is the wavelength of X-ray, which is 0.154 nm. For all scattering experiments the sample-to-detector distance was 1603 mm, and the q -range was calibrated using a silver behenate standard.

For variable temperature SAXS experiments, samples were heated using a Linkam hot stage positioned in the sample chamber at a heating rate of 20 °C/s and held for 30 min to equilibrate at a given temperature before data acquisition. An exposure time of 1 h to collect SAXS data was used for all samples.

Absolute intensities were obtained by first determining the calibration scale factor. This factor was obtained by comparing the scattering pattern of a glassy carbon sample and the calibrated intensity of glass carbon from Argonne Photon Source (APS),²⁹

$$\text{Scale Factor} = \left(\frac{\partial \Sigma}{\partial \Omega} \right)_{st} \bigg/ \frac{(I_{st}(q) - BG_{st})}{d_{st} T_{st}} \quad (3.1)$$

where d_{st} is the thickness of glass carbon, T_{st} is the transmission of glassy carbon, and BG_{st} is the background scattering.

Thus, absolute intensities of all the Nafion samples were obtained using the following equation, where d_s is the thickness of the sample, and T_s is the transmission of the sample.

$$\text{Absolute intensity} = \left(\frac{\partial \Sigma}{\partial \Omega} \right)_{st} \frac{(I_s(q) - BG_s)}{d_s T_s} \bigg/ \frac{(I_{st}(q) - BG_{st})}{d_{st} T_{st}} \quad (3.2)$$

3.3 Data Analysis

One-dimensional correlation function was applied to calculate the long periodicity within Nafion. Fourier transformation of the experimental scattering curve gives the one-dimensional correlation function,³⁰ $\gamma_1(r)$,

$$\gamma_1(r) = \frac{\int_0^\infty [I - I_b] q^2 \cos(qr) dq}{\int_0^\infty [I - I_b] q^2 dq} \quad (3.3)$$

where I_b is the scattering of local electron density fluctuation in the amorphous phase,

$$\lim_{q \rightarrow \infty} [K_p - (I - I_b) q^4 (\sigma^2 q^2)] = 0 \quad (3.4)$$

and I_b could be obtained from Porod's law as illustrated in Eqn. 3.4, where K_p is the Porod constant, and σ is also a constant associated with the thickness between crystalline and

amorphous phases.³¹ Thus, I_b is estimated as the slope of the straight line plot of Iq^4 versus q^4 .

3.4 Results and Discussion

SAXS profiles of Nafion 117CS containing alkali metal ions are shown in Figure 3.2. Clearly, there was no crystalline peak observed at $q=0.5 \text{ nm}^{-1}$ for Cs^+ -form Nafion, while there was no ionic peak observed at around $q=2.0 \text{ nm}^{-1}$ for both Li^+ and Na^+ -form Nafion. However, a relatively broad peak at around $q=2.5 \text{ nm}^{-1}$ was observed for H^+ -form Nafion, which is believed to be the ionic peak as evidenced in other studies.^{4,5} For K^+ -form Nafion, both a crystalline peak and a small ionic peak were observed, while a large ionic peak and a relatively small crystalline peak were observed for Rb^+ -form Nafion. Since there is little change in the positions of these peaks, negligible morphological change with the various counterions can be presumed,³ and the different behaviors of crystalline and ionic scattering peaks can only be attributed to the electron density differences associated with the various alkali metal ion forms of Nafion.

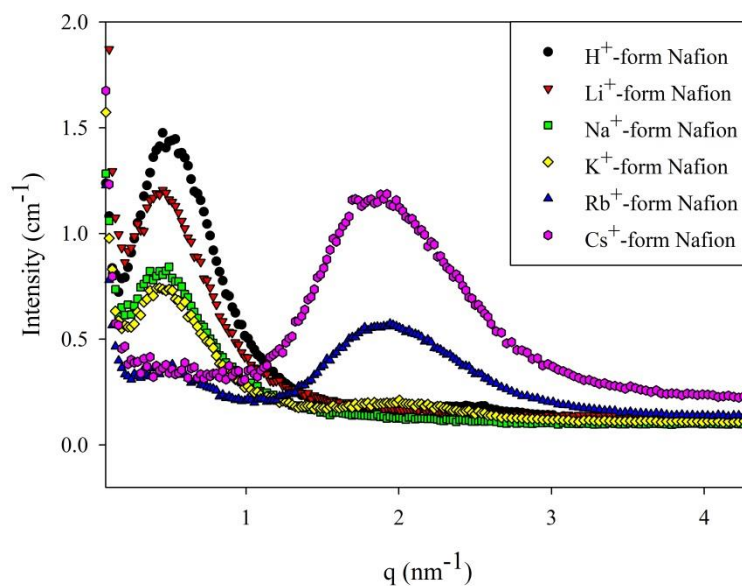


Figure 3.2. SAXS data of Nafion 117CS containing alkali metal ions

The electron densities of the crystalline region, the amorphous region, and the ionic region in Cs^+ and Na^+ -form Nafion are presented in Figure 3.3. The observed scattering peaks in the SAXS profiles are due to the electron density differences among the crystalline region, the amorphous region, and the ionic region within Nafion. A scattering peak is observed whenever there is a difference in electron densities between the different regions. The larger the difference in electron density, the larger the magnitude of the scattering peak. For Nafion, the ionic peak is dependent on the electron density difference between the amorphous region, ρ_a and the ionic region, ρ_i . While the crystalline peak finds its origin in the difference of the electron densities between the crystalline region and the non-crystalline region, which would encompass the amorphous region and ionic region. In this case, the electron density of the non-crystalline region can be written as the average electron density of amorphous region and that of ionic region, $\rho_c = \langle \rho_a + \rho_i \rangle$. Figure 3.3 clearly illustrates the scattering phenomenon in Figure 3.2. In Na^+ -form Nafion, the

ionic region becomes indiscernible to X-rays because the electron density of Na⁺-containing ionic region and that of the amorphous region are almost the same ($\rho_i \cong \rho_a$), which leads to a zero electron density difference between these two different regions. Thus, only a crystalline peak could be observed. On the contrary, Cs⁺-form Nafion did not show a crystalline peak. As the electron density of Cs⁺ is much higher, it increases the electron densities of both ionic region and the non-crystalline region, which results in an identical electron density between the crystalline and non-crystalline regions ($\rho_c \cong \langle \rho_a + \rho_i \rangle$). In this case, only the ionic peak was observed as there is still a large difference in the electron densities between the amorphous region and ionic region, while the crystalline peak was indistinguishable to X-rays.

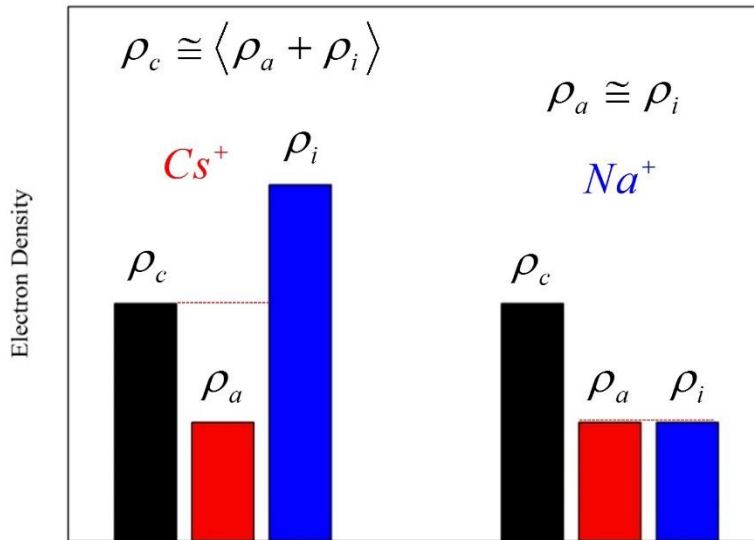


Figure 3.3. Electron densities of crystalline, amorphous, and ionic regions in Cs⁺ and Na⁺-form Nafion

To further understand how electron density differences affect scattering behaviors, variable temperature SAXS experiments were performed on both Na⁺ and Cs⁺-form

Nafion. Figure 3.4 presents the variable temperature SAXS profiles of Na⁺-form Nafion. It can be observed that the ionic peak of Na⁺-form Nafion began to appear when the temperature was at around 50 °C. Since the sample was heated, both the crystalline region and amorphous region would expand, which resulted in changes of volumes of these different regions. Because the amorphous region of Nafion has a larger thermal expansion coefficient than that of the ionic region containing Na⁺ ions,³² the change in volume was larger for the amorphous region than that of the ionic region, which results in a larger change in electron density for the amorphous region. This leads to an unequal relationship between ρ'_a and ρ'_i , which is illustrated in Figure 3.5. Thus the ionic peak reappears as a result of changes in electron densities of amorphous and ionic regions within Nafion upon heating.

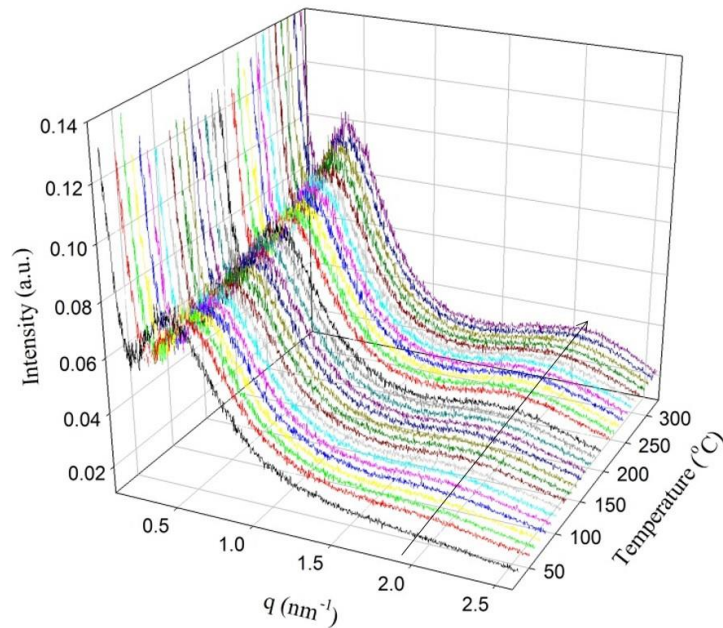


Figure 3.4. Variable temperature SAXS of Na⁺-form Nafion

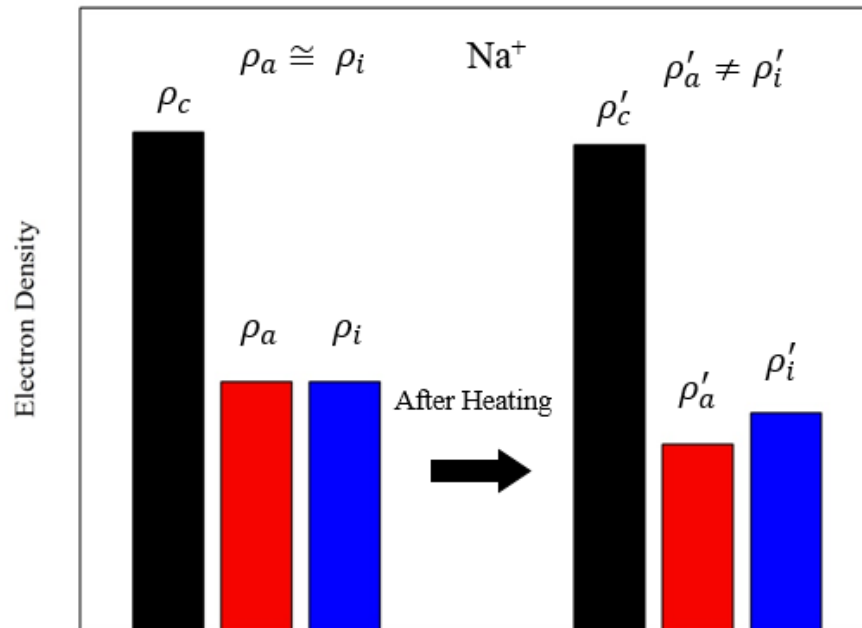


Figure 3.5. Electron densities of crystalline, amorphous, and ionic regions in Na⁺-form Nafion before and after heating

Figure 3.6 presents variable temperature SAXS profiles of Cs⁺-form Nafion. The crystalline peak of Cs⁺-form Nafion was observed when the temperature was from 210 °C to 300 °C. Since the sample was also heated, the crystalline region, ionic region and amorphous region would also expand, which resulted in an increase in the volumes of these regions. Since the amorphous region has a larger thermal expansion coefficient than that of the crystalline region,³² while the ionic region containing Cs⁺ has the smallest thermal expansion coefficient, the change in electron density would be the largest for the amorphous region and smallest for the ionic region,³³ and this is illustrated in Figure 3.7. This results in an unbalanced relationship in the electron densities between the crystalline region and non-crystalline region, which contains both the amorphous region and ionic

region ($\rho'_c \neq \rho'_a + \rho'_i$). Thus, it leads to the appearance of the crystalline peak in Cs⁺-form Nafion.

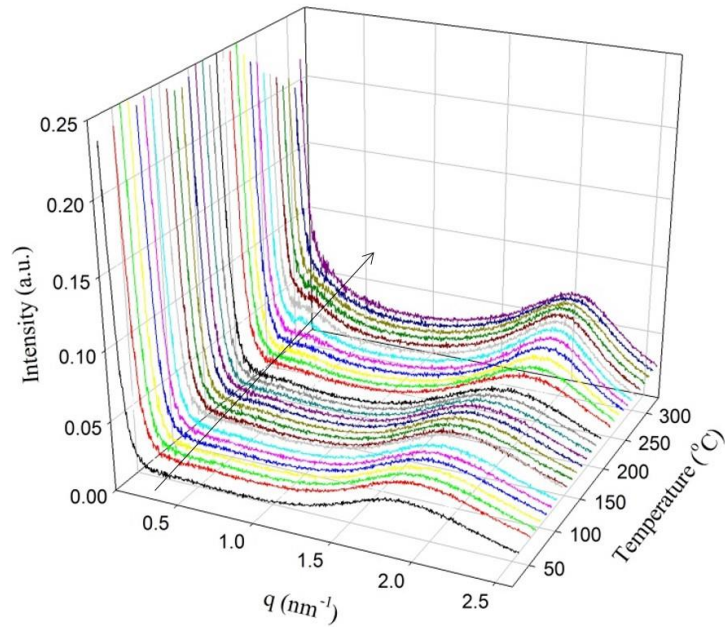


Figure 3.6. Variable temperature SAXS of Cs⁺-form Nafion

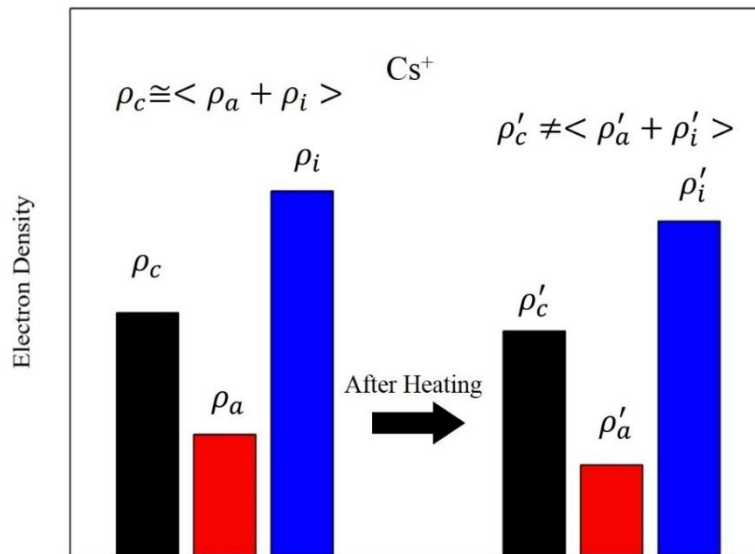


Figure 3.7. Electron densities of crystalline, amorphous, and ionic regions in Cs⁺-form Nafion before and after heating

It was also observed that the magnitudes of the scattering intensities of both the crystalline peak in Na⁺-form Nafion and the ionic peak in Cs⁺-form Nafion increased when the samples were heated. This is in part due to the fact that the electron density differences between the different domains, i.e. $\Delta\rho = \rho_c - \langle \rho_a + \rho_i \rangle$ for crystalline peak in Na⁺-Nafion, and $\Delta\rho = \rho_i - \rho_a$ for ionic peak in Cs⁺-Nafion, both increased as a result of heating and thus lead to an increase in the magnitudes of the scattering profiles.

Analysis of SAXS data using one-dimensional correlation function was performed to obtain the long periodicity of the crystalline region within Nafion.^{30,31} The 1-D correlation function results for Li⁺ and Na⁺-form Nafion are shown in Figure 3.7. The first peak observed in the 1-D correlation function defines the long periodicity, L , and L for Li⁺ and Na⁺-form Nafion was found to be 8.5 nm and 9.2 nm, respectively. It is notable that low degrees of crystallinity in Nafion lead to the weak maxima in 1-D correlation curves of Li⁺

and Na⁺-form Nafion. On the other hand, the 1-D correlation function of K⁺-form Nafion is showed in Figure 3.8. Because of the existence of the ionic peak in K⁺-form Nafion, the 1-D correlation function fluctuates, signifying that one-dimensional correlation function should not be applied to analyze the scattering data that contain extra scattering peaks other than crystalline peak. These results demonstrate that making the ionic peak indistinguishable to X-ray is necessary in order to study the long periodicity of the crystalline region in Nafion. Moreover, the long period distance is almost the same for both the Li⁺ and Na⁺-Nafion samples, which further demonstrates that the morphology of Nafion remains the same after neutralizing with various alkali metals.

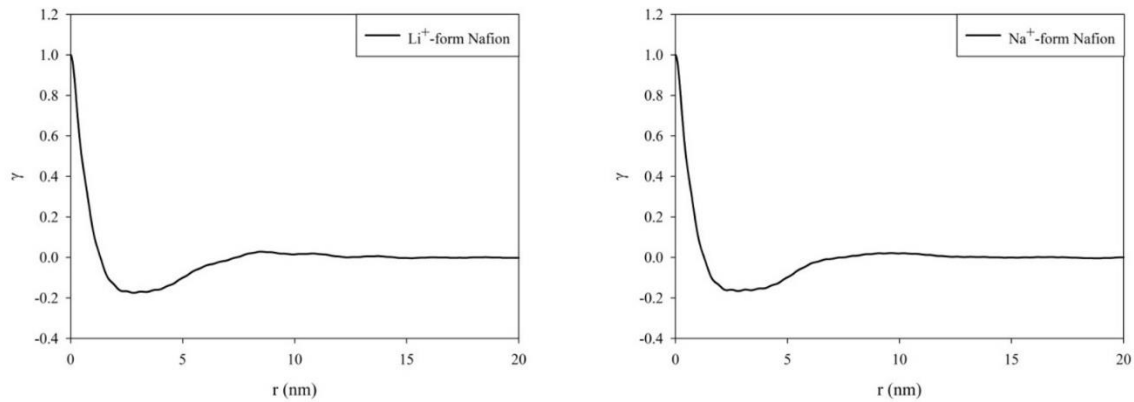


Figure 3.8. One-dimensional correlation data of Li⁺ and Na⁺-form Nafion

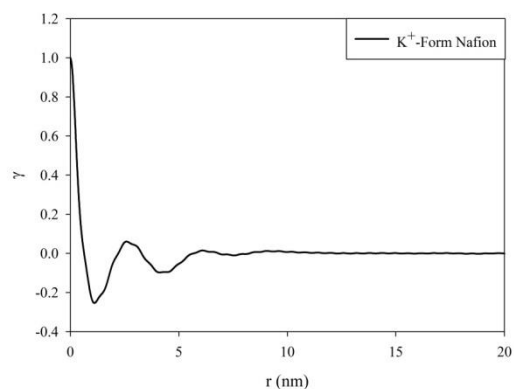


Figure 3.9. One-dimensional correlation data of K^+ -form Nafion

3.5 Conclusions

For the first time, a systematic study of applying CV in SAXS to probe the morphology of Nafion in the solid state was performed. It was clearly observed that when H^+ -Nafion was neutralized with cesium hydroxide, the crystalline peak was indistinguishable. While the ionic peak was invisible to X-rays when H^+ -Nafion was neutralized with sodium hydroxide. Variable temperature SAXS experiments further demonstrate that these scattering behaviors are due to the electron densities of different domains within Nafion. The feasibility of separating the crystalline and ionic regions provides a means to probe the morphology of Nafion more extensively. Using one-dimensional correlation function for Li^+ and Na^+ -form Nafion, the long periodicity of the crystalline region of Nafion was found to be around 9 nm. While for K^+ -form Nafion, the one-dimensional correlation functioned ineffective because of the existence of the ionic peak. Our research shows the applicability of the CV method on the study of Nafion morphology, and this method could also apply to other ionomers.

3.6 Acknowledgement

The authors gratefully acknowledge the financial support from ITACS. The authors also thank Dr. Jan Ilavsky for providing standard glassy carbon to obtain absolute intensity. This material is partially based upon work supported by the National Science Foundation under Grant No. DMR-0923107.

3.7 References

- (1) Gierke, T. D.; Munn, G. E.; Wilson, F. C. *Journal of Polymer Science: Polymer Physics Edition* **1981**, *19*, 1687.
- (2) Roche, E. J. S., R. S.; Russell, T. P.; MacKnight, W. J. *J. Polym. Sci., Polym. Phys. Ed.* **1980**, *18*, 1497.
- (3) Roche, E. J.; Pineri, M.; Duplessix, R.; Levelut, A. M. *Journal of Polymer Science: Polymer Physics Edition* **1981**, *19*, 1.
- (4) Fujimura, M.; Hashimoto, T.; Kawai, H. *Macromolecules* **1981**, *14*, 1309.
- (5) Fujimura, M.; Hashimoto, T.; Kawai, H. *Macromolecules* **1982**, *15*, 136.
- (6) Roche, E. J.; Pineri, M.; Duplessix, R. *Journal of Polymer Science: Polymer Physics Edition* **1982**, *20*, 107.
- (7) Moore, R. B.; Martin, C. R. *Macromolecules* **1988**, *21*, 1334.
- (8) Gebel, G.; Aldebert, P.; Pineri, M. *Polymer* **1993**, *34*, 333.
- (9) Haubold, H. G.; Vad, T.; Jungbluth, H.; Hiller, P. *Electrochimica Acta* **2001**, *46*, 1559.
- (10) Rollet, A.-L.; Diat, O.; Gebel, G. *The Journal of Physical Chemistry B* **2002**, *106*, 3033.

- (11) Rubatat, L.; Rollet, A. L.; Gebel, G.; Diat, O. *Macromolecules* **2002**, *35*, 4050.
- (12) Mauritz, K. A.; Moore, R. B. *Chemical Reviews* **2004**, *104*, 4535.
- (13) Rubatat, L.; Gebel, G.; Diat, O. *Macromolecules* **2004**, *37*, 7772.
- (14) Page, K. A.; Cable, K. M.; Moore, R. B. *Macromolecules* **2005**, *38*, 6472.
- (15) Page, K. A.; Landis, F. A.; Phillips, A. K.; Moore, R. B. *Macromolecules* **2006**, *39*, 3939.
- (16) Osborn, S. J.; Hassan, M. K.; Divoux, G. M.; Rhoades, D. W.; Mauritz, K. A.; Moore, R. B. *Macromolecules* **2007**, *40*, 3886.
- (17) Schmidt-Rohr, K.; Chen, Q. *Nat Mater* **2008**, *7*, 75.
- (18) Page, K. A.; Park, J. K.; Moore, R. B.; Garcia Sakai, V. *Macromolecules* **2009**, *42*, 2729.
- (19) Song, J. M., Park, Jong Keun, Moore, Robert B. *To be submitted* **2012**.
- (20) Park, J. K.; Li, J.; Divoux, G. M.; Madsen, L. A.; Moore, R. B. *Macromolecules* **2011**, *44*, 5701.
- (21) Kim, M.-H.; Glinka, C. J.; Grot, S. A.; Grot, W. G. *Macromolecules* **2006**, *39*, 4775.
- (22) Litt, M. *Polym. Prepr.* **1997**, *38*, 80.
- (23) van der Heijden, P. C.; Rubatat, L.; Diat, O. *Macromolecules* **2004**, *37*, 5327.
- (24) Rubatat, L.; Diat, O. *Macromolecules* **2007**, *40*, 9455.
- (25) Elliott, J. A.; Wu, D.; Paddison, S. J.; Moore, R. B. *Soft Matter* **2011**.

- (26) Glatter, O.; Kratky, O. *Small angle x-ray scattering*; Academic Press, 1982.
- (27) Dingenouts, N.; Ballauff, M. *Acta Polymerica* **1993**, *44*, 178.
- (28) Grunder, R.; Urban, G.; Ballauff, M. *Colloid & Polymer Science* **1993**, *271*, 563.
- (29) Fan, L.; Degen, M.; bendle, S.; Grupido, N.; Ilavsky, J. *Journal of Physics: Conference Series* **2010**, *247*, 012005.
- (30) Vonk, C. G.; Kortleve, G. *Colloid & Polymer Science* **1967**, *220*, 19.
- (31) Koberstein, J. T.; Stein, R. S. *Journal of Polymer Science: Polymer Physics Edition* **1983**, *21*, 2181.
- (32) Araki, Y. *Journal of Applied Polymer Science* **1965**, *9*, 421.
- (33) Bradstreet, S. W.; Davis, L. W. *AIP Conference Proceedings* **1972**, *3*, 287.

Numerical studies have been performed to understand the structures of Nafion in order to explain its excellent water uptake, gas transport, proton conductivity, and mechanical stability.³⁻¹⁸ Several morphological models have also been proposed to account for the origins of the crystalline and ionic peaks, such as the cluster-network model proposed by Gierke and co-workers,^{17,18} core-shell model developed by Fujimura and co-workers,^{9,10} lamellar model proposed by Litt,¹⁹ sandwich-like model proposed by Haubold and co-workers,¹² fibrillar nanostructure model by Rubatat and co-workers,^{6,20,21} worm-like model by Kim and co-workers,⁷ parallel cylindrical water nanochannel model proposed by Schmidt-Rohr and Chen,²² and bicontinuous network of ionic clusters embedded in a matrix of fluorocarbon chains within Nafion recently proposed by Elliott and co-workers.²³ Besides these steady state morphological studies, Gebel²⁴ fully studied the morphological evolution of Nafion from dry state to solution state by the means of SAXS and SANS, which further demonstrated the morphological transition of reverse micellar structure in swollen membranes to the rod-like structure in PFSI dispersions that were evidenced in the other studies.^{25,26} Some researchers have also been working on studying how casting procedures (i.e. temperatures,^{27,28} solvents^{11,29-32}) affect the morphology of Nafion in order to probe the structure-properties relationship within Nafion. However, there still lacks a crucially fundamental understanding of the morphological development of these nanostructured features within Nafion, as well as the role of crystallinity, during solution processing.

Time resolved small angle X-ray scattering (SAXS) has been proved to be an excellent technique to probe the nano-scale morphological changes in real time.³³⁻³⁷ In this work, with the use of time resolved SAXS, we were able to probe the morphological development

during solvent evolution as the Nafion dispersion was converted to a solid nanostructured film. We were also able to show that crystallinity within Nafion develops later than the formation of ionic domains, and the crystallites are not confined in the cylindrical particles, but dispersed in solution. This work further demonstrates that the crystalline and ionic domains are intimately linked through complex self-assembly during membrane processing.

4.2 Experimental Section

4.2.1 Materials

Nafion 117CS (1100EW, sulfonic acid form) was purchased from E. I. DuPont Company. Dimethyl sulfoxide (DMSO) was purchased from Aldrich Chemical Co., and used as-received without further purification.

4.2.2 Preparation of Neutralized Perfluorinated Sulfonic Acid (PFSA) Membranes

Nafion 117CS membranes were cleaned by refluxing them in HNO₃ (8M) for 2 h to remove impurities, then washed with deionized (DI) water three times, and boiled in DI water for 1 h. Then membranes were dried at room temperature between Kim wipes for an hour and placed in a vacuum oven for 12 h at 70 °C.

4.2.3 Preparation of Nafion Dispersion

14 g of H⁺-Nafion membrane was dissolved in 300 ml of water and ethanol mixture (50/50 in volume) at 200 °C for 2 h in a PARR pressure reactor to yield 5% w/v Nafion dispersion. The obtained solutions were first filtered through 5 μm pore size filter paper in order to remove dust particles and aggregates. Then DMSO was added to this Nafion

dispersion, and the solution was put under 70 °C to slowly evaporate the solvent to achieve desired concentrations.

4.2.4 Solution Processing Procedure

H⁺-Nafion dispersion was confined in a solvent-casting cell made of stainless with two Kapton sheets as windows for X-ray beam to travel through. The solvent-casting cell shown in Figure 4.2 was heated from room temperature to a final temperature of 200 °C in the air and held at that temperature until the end of the experiment. Nitrogen gas was used to purge the system during the casting process. The whole experiment lasted for around 10 minutes for each sample.

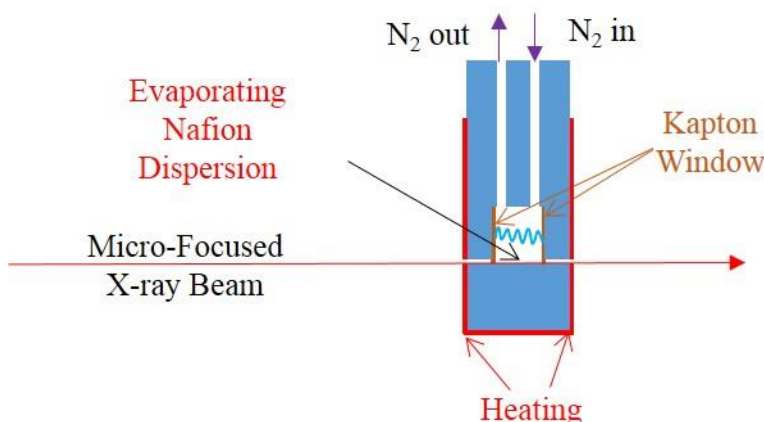


Figure 4.2. Solvent-casting cell for synchrotron SAXS studies of *in-situ* film formation

4.2.5 Small Angle X-ray Scattering Experiment

Time resolved SAXS experiments were performed at Advanced Photon Source (APS), Argonne National Laboratory (Beamline 5-ID DND-CAT). The wavelength of X-ray was 0.07293 nm. Scattering from a silver behenate standard was used to calibrate the sample-to-detector distance, and the sample-to-detector distance was 2974 mm. SAXS images were obtained using a low-noise, Mar USA Inc, 162 mm, marCCD camera, with a 4 second

exposure time. All SAXS data were analyzed using the in-house software package provided in APS to obtain radially integrated SAXS intensity versus scattering vector q , where $q=(4\pi/\lambda)\sin(\theta)$, θ is one half of the scattering angle and λ is the wavelength of X-ray. The profiles were vertically shifted to facilitate a comparison of the peak positions. SAXS data were collected as soon as the solution processing procedure started and lasted during the whole experiment. In the 3-dimensional plot, another axis indicates the time at which SAXS data were collected was used. It needs to point out here that the absolute value of time may not be very accurate given that the accurate experiment time was hard to obtain, but still it serves the purpose in this paper. Solution samples were measured in a glass capillary with a diameter of 1.5 mm and wall thickness of 0.01 mm. The measured intensity had been corrected for sample transmission, solvent scattering and background scattering.

In-house SAXS experiments were performed using a Rigaku S-Max 3000 3 pinhole SAXS system, equipped with a rotating anode emitting X-ray with a wavelength of 0.154 nm (Cu $K\alpha$). The sample-to-detector distance was 1603 mm, and q -range was calibrated using a silver behenate standard. Two-dimensional SAXS patterns were obtained using a fully integrated 2D multiwire, proportional counting, gas-filled detector, with an exposure time of 1 hour. All the SAXS data were analyzed using the SAXSGUI software package to obtain radially integrated SAXS intensity versus scattering vector q . The measured intensity had also been corrected for sample transmission, solvent scattering and background scattering.

4.3 Results and Discussion

Figure 4.3 presents the SAXS profiles of H⁺-Nafion dissolved in DMSO solution with various polymer volume fractions (ϕ_p). A scattering maxima was observed for all these solutions, and this maxima shifts to lower q value as the concentration of Nafion in DMSO increases. This is in agreement with Gebel and co-workers' results^{24,25} that the distance between cylindrical particles in Nafion dispersion decreases with increasing concentration. Furthermore, the calculated full width at half maximum (FWHM) listed in Table 4.1 for these maxima shows that this scattering peak becomes broader as concentration increases, indicating a more random distribution of these cylindrical particles when they are approaching to each other as structure factor is playing a more important role in the scattering profile.

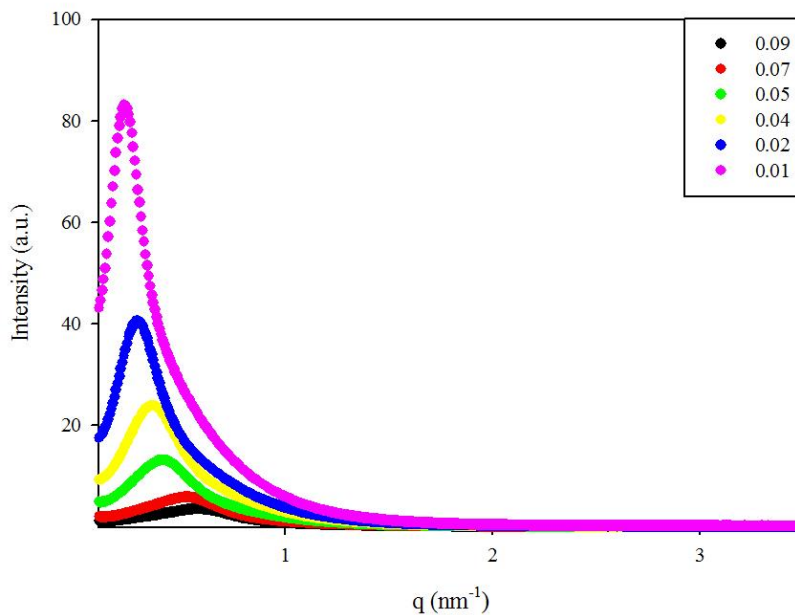


Figure 4.3. SAXS profiles of Nafion dissolved in DMSO solution with various polymer volume fraction (ϕ_p) (the curves have been vertically shifted to facilitate a comparison of the peak positions)

Table 4.1. Detailed information for the SAXS data shown in Figure 4.2

ϕ_p	q (nm ⁻¹)	d (nm)	FWHM (nm ⁻¹)
0.09	0.56	11	0.50
0.07	0.53	12	0.46
0.05	0.41	15	0.43
0.04	0.36	17	0.35
0.02	0.28	22	0.28
0.01	0.22	28	0.22

Since Nafion solution in DMSO begins to form a gel when volume fraction of Nafion is above around 0.2, time-resolved SAXS experiments were started by using a Nafion dispersion with volume fraction of 0.14 in order to cover the morphological development from solution to gel state and finally to solid state membrane, as well as to yield a good thickness of membrane for SAXS measurements. Three-dimensional data were plotted and presented in Figure 4.4. The scattering data can be divided into three distinct regions, with the first region (Region I) from 0 to 2 min where Nafion was still in the solution, the second region (Region II) from 2 min to 8 min where Nafion gel started to form and dried out, and the third region (Region III) from 8 min to the end where a dry membrane was already formed.

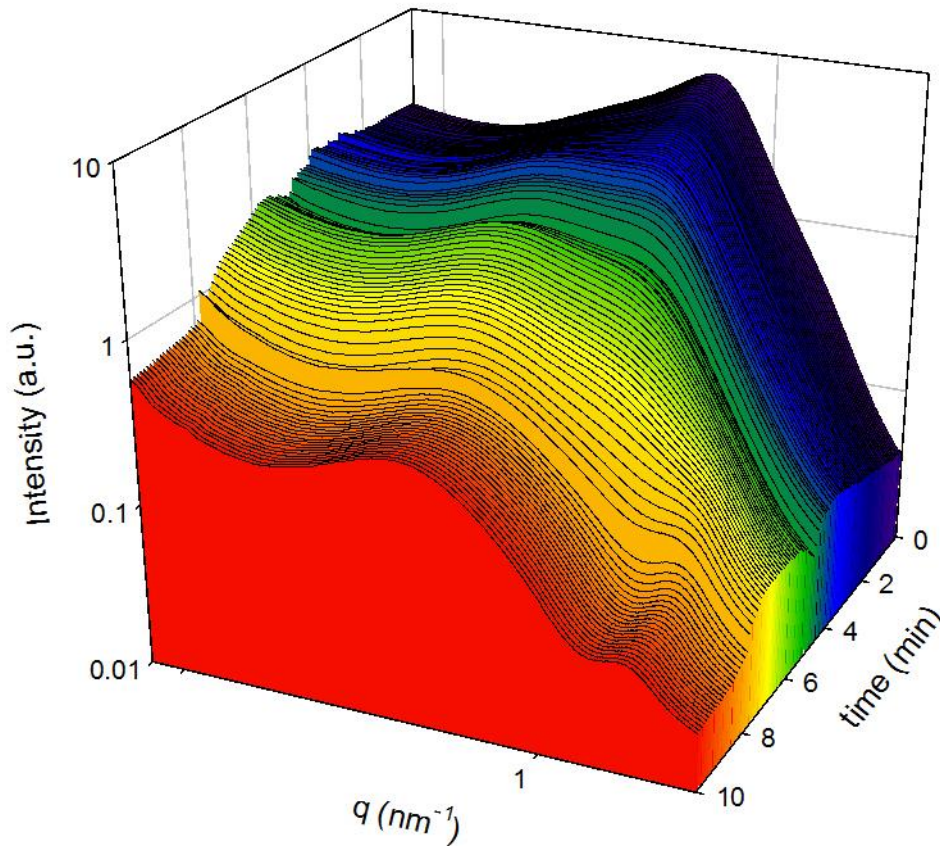


Figure 4.4. Three-dimensional SAXS profiles for solution processing Nafion in DMSO

For Region I, it was still a continuous process of solvent evolution following the data shown in Figure 4.3. In this region. The cylindrical particles were approaching to each other with increasing concentration. At this stage, no crystalline peak was observed, indicating that crystallinity was not yet formed.

For Region III, Nafion was already in solid state as a dry membrane, and both the crystalline peak and ionic peak could be observed and the shapes of these two scattering peaks were also well defined. In this region, the scattering profile is very similar to that of dry H⁺-Nafion in other scattering studies.^{6,8-16}

However, the scattering behavior in Region II caused interest since it has never been observed in previous studies. In order to obtain the accurate volume fractions of Nafion in Region II, several individual scattering experiments using in-house SAXS were prepared on solution processing Nafion with accurate volume fraction information in order to match the scattering profiles in Figure 4.4, and the SAXS data on these samples are presented in Figure 4.5. As mentioned in the previous study, when volume fraction of Nafion is above 0.2, it starts to form gel. Thus, Nafion samples with volume fraction of 0.21, 0.22, 0.24 and 0.37 were all in gel forms. However, these samples are very different from the Nafion samples that are swollen with different solvents as performed in Gebel and co-workers' studies^{17,24,38} even though the volume fractions of Nafion are the same. Thus, it would not be surprising to see these unique scattering profiles for the first time. These data in Figure 4.5 correspond well with the data shown in Region II in Figure 4.4 that two scattering peaks could be observed. The peak at lower q value, which is the typical peak position of the "crystalline peak" in Nafion was not observed in Gebel's study²⁴ for swollen Nafion membrane when the volume fraction of Nafion in his study is close to the volume fraction of Nafion in this work, and this may be due to low scattering contrast in Gebel's study. In fact, the role of crystallinity during structural evolution was not considered in his study. In both Figure 4.4 and Figure 4.5, it was clearly observed that the crystalline peak starts to appear while the solution maxima that characterizes cylindrical particles in solution maintains and continues to shift to higher q values. Unlike the model proposed by Aldebert and co-workers³⁹ assuming that crystalline domains reside within the rod-like particles in solution, this scattering behavior first clearly demonstrates that the crystallinity develops

later than ionic aggregates do, which indicates that crystalline domains are dispersed in solution rather than residing within the cylindrical particles.

The solution maxima continues to shift to higher q values with increasing concentration and finally evolves into the dry-state ionic peak. This indicates that the ionic peak in the dry form originates through a morphological continuity from the rod like structures in solution. At the same time the crystallinity peak shifted slightly to higher q value (smaller dimension) as can be better observed in the two-dimensional plot shown in Figure 4.6. This slight change is probably due to a further formation of crystallites that results in an increase in both the number and thickness of the crystallites. As the crystallites co-exist in solution with the cylindrical particles during solution processing, it would be expected that ionic aggregates would affect the formation of crystallites in some extent, though the complex self-assembly that link the crystalline and ionic domains through during membrane processing still needs to be further studied. As the dry-state ionic peak starts to appear, a power law of -4 in the log-log plot of intensity versus q value in the region between the crystalline peak and ionic peak begins to appear, indicating the formation of sharp interface between crystallites and ionic domains in dry state Nafion.

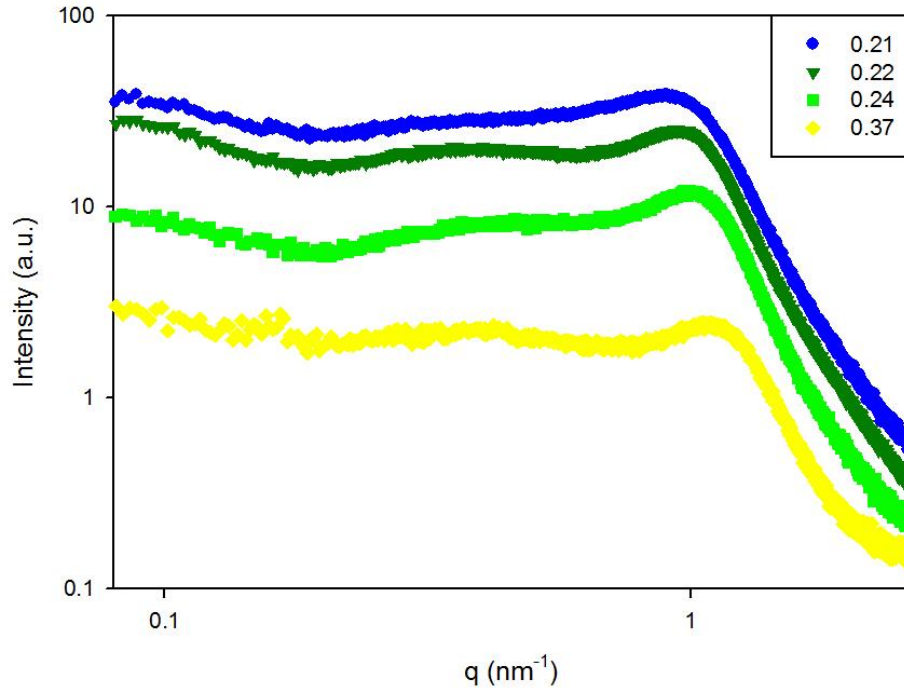


Figure 4.5. SAXS profiles of Nafion, from gel to dry membrane

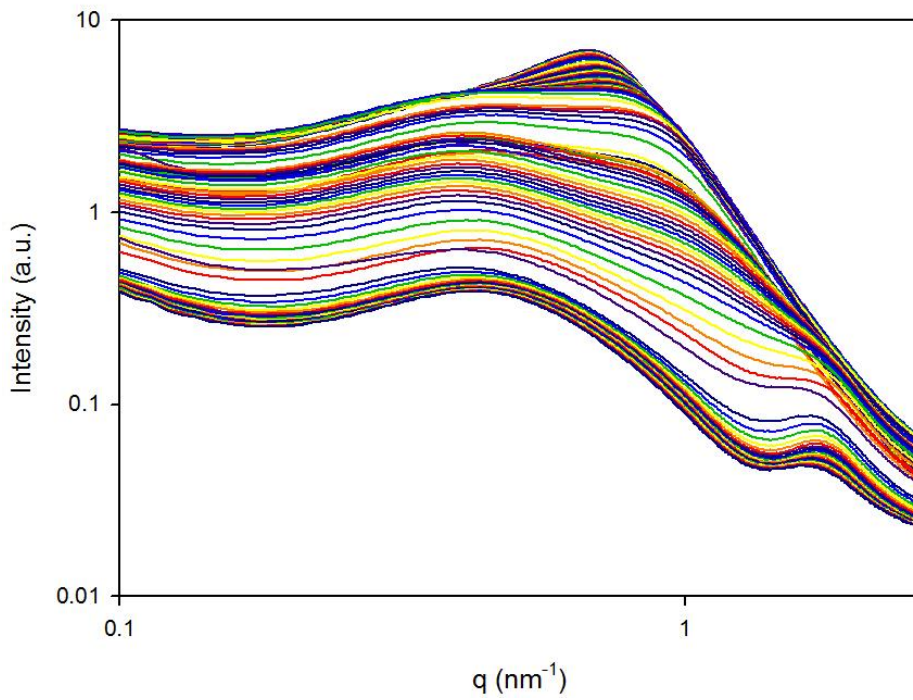


Figure 4.6. Two-dimensional SAXS plots for solution processing Nafion in DMSO

4.4 Conclusion

For the first time the structural evolution during solution processing Nafion was studied in this work, which shows that the morphological development of solution processing Nafion is not a reverse process of the structural evolution process of Nafion swollen with water. The crystallites are demonstrated to develop later than the formation of ionic domains, and they do not reside in the cylindrical particles, but are dispersed in solution. Through this fundamental study, it further demonstrate that the crystalline and ionic domains are intimately linked through complex self-assembly during membrane processing. Base on this time-resolved details of morphological development probed by SAXS, we could further control the formation of crystallinity and ionic domains by using different solvents or different casting procedures to yield desired morphology of Nafion and other fuel cell materials for better energy needs.

4.5 Acknowledgement

We acknowledge the Advanced Photon Source supported by the U. S. Department of Energy, Office of Science, Office of Basic Energy Sciences, under Contract No. W-31-109-Eng-38, for access to the beamtime 5ID-D, operated by DND-CAT. The DND-CAT is supported by the E.I. DuPont de Nemours & Co., The Dow Chemical Company, the U.S. National Science Foundation through Grant DMR-9304725 and the State of Illinois through the Department of Commerce and the Board of Higher Education Grant IBHE HECA NWU 96. The diode beam stops were constructed at DuPont by Robert F. Knox

and Mark G. Bradigan under J. David Londono's direction. This material is partially based upon work supported by the National Science Foundation under Grant No. DMR-0923107.

4.6 References

- (1) Mauritz, K. A.; Moore, R. B. *Chemical Reviews* **2004**, *104*, 4535.
- (2) Mohsen, S.; Kwang, J. K. *Smart Materials and Structures* **2001**, *10*, 819.
- (3) Roche, E. J.; Pineri, M.; Duplessix, R.; Levelut, A. M. *Journal of Polymer Science: Polymer Physics Edition* **1981**, *19*, 1.
- (4) Rollet, A.-L.; Diat, O.; Gebel, G. *The Journal of Physical Chemistry B* **2002**, *106*, 3033.
- (5) Rubatat, L.; Rollet, A. L.; Gebel, G.; Diat, O. *Macromolecules* **2002**, *35*, 4050.
- (6) Rubatat, L.; Gebel, G.; Diat, O. *Macromolecules* **2004**, *37*, 7772.
- (7) Kim, M.-H.; Glinka, C. J.; Grot, S. A.; Grot, W. G. *Macromolecules* **2006**, *39*, 4775.
- (8) Roche, E. J. S., R. S.; Russell, T. P.; MacKnight, W. J. *J. Polym. Sci., Polym. Phys. Ed.* **1980**, *18*, 1497.
- (9) Fujimura, M.; Hashimoto, T.; Kawai, H. *Macromolecules* **1981**, *14*, 1309.
- (10) Fujimura, M.; Hashimoto, T.; Kawai, H. *Macromolecules* **1982**, *15*, 136.
- (11) Moore, R. B.; Martin, C. R. *Macromolecules* **1988**, *21*, 1334.
- (12) Haubold, H. G.; Vad, T.; Jungbluth, H.; Hiller, P. *Electrochimica Acta* **2001**, *46*, 1559.
- (13) Page, K. A.; Cable, K. M.; Moore, R. B. *Macromolecules* **2005**, *38*, 6472.

- (14) Page, K. A.; Landis, F. A.; Phillips, A. K.; Moore, R. B. *Macromolecules* **2006**, *39*, 3939.
- (15) Song, J. M., Park, Jong Keun, Moore, Robert B. *To be submitted* **2012**.
- (16) Park, J. K.; Li, J.; Divoux, G. M.; Madsen, L. A.; Moore, R. B. *Macromolecules* **2011**, *44*, 5701.
- (17) Gierke, T. D.; Munn, G. E.; Wilson, F. C. *Journal of Polymer Science: Polymer Physics Edition* **1981**, *19*, 1687.
- (18) Hsu, W. Y.; Gierke, T. D. *Journal of Membrane Science* **1983**, *13*, 307.
- (19) Litt, M. *Polym. Prepr.* **1997**, *38*, 80.
- (20) van der Heijden, P. C.; Rubatat, L.; Diat, O. *Macromolecules* **2004**, *37*, 5327.
- (21) Rubatat, L.; Diat, O. *Macromolecules* **2007**, *40*, 9455.
- (22) Schmidt-Rohr, K.; Chen, Q. *Nat Mater* **2008**, *7*, 75.
- (23) Elliott, J. A.; Wu, D.; Paddison, S. J.; Moore, R. B. *Soft Matter* **2011**.
- (24) Gebel, G. *Polymer* **2000**, *41*, 5829.
- (25) Loppinet, B.; Gebel, G.; Williams, C. E. *The Journal of Physical Chemistry B* **1997**, *101*, 1884.
- (26) Loppinet, B.; Gebel, G. *Langmuir* **1998**, *14*, 1977.
- (27) Silva, R. F.; De Francesco, M.; Pozio, A. *Electrochimica Acta* **2004**, *49*, 3211.
- (28) Vengatesan, S.; Cho, E.; Kim, H.-J.; Lim, T.-H. *Korean J. Chem. Eng.* **2009**, *26*, 679.

- (29) Grot, W. G.; COMPANY, E. I. D. P. D. N. A., Ed. 1985 Vol. EP0066369
- (30) Moore, R. B.; Martin, C. R. *Analytical Chemistry* **1986**, *58*, 2569.
- (31) Lin, H.-L.; Yu, T. L.; Huang, C.-H.; Lin, T.-L. *Journal of Polymer Science Part B: Polymer Physics* **2005**, *43*, 3044.
- (32) Ma, C.-H.; Yu, T. L.; Lin, H.-L.; Huang, Y.-T.; Chen, Y.-L.; Jeng, U. S.; Lai, Y.-H.; Sun, Y.-S. *Polymer* **2009**, *50*, 1764.
- (33) Hsiao, B. S.; Verma, R. K. *Journal of Synchrotron Radiation* **1998**, *5*, 23.
- (34) Nojima, S.; Kato, K.; Ono, M.; Ashida, T. *Macromolecules* **1992**, *25*, 1922.
- (35) Akpalu, Y.; Kielhorn, L.; Hsiao, B. S.; Stein, R. S.; Russell, T. P.; van Egmond, J.; Muthukumar, M. *Macromolecules* **1999**, *32*, 765.
- (36) Hsiao, B. S.; Sauer, B. B.; Verma, R. K.; Zachmann, H. G.; Seifert, S.; Chu, B.; Harney, P. *Macromolecules* **1995**, *28*, 6931.
- (37) Lee, C. H.; Saito, H.; Inoue, T.; Nojima, S. *Macromolecules* **1996**, *29*, 7034.
- (38) Gebel, G.; Moore, R. B. *Macromolecules* **2000**, *33*, 4850.
- (39) Aldebert, P.; Dreyfus, B.; Gebel, G.; Nakamura, N.; Pineri, M.; Volino, F. *J. Phys. France* **1988**, *49*, 2101.

clusters, and is defined as the “ionic peak”. Several morphological models have been proposed based on the scattering data, such as the cluster-network model proposed by Gierke and co-workers,^{17,18} core-shell model developed by Fujimura and co-workers,^{9,10} lamellar model proposed by Litt,¹⁹ sandwich-like model proposed by Haubold and co-workers,¹² fibrillar nanostructure model by Rubatat and co-workers,^{6,20,21} worm-like model by Kim and co-workers,⁷ parallel cylindrical water nanochannel model proposed by Schmidt-Rohr and Chen,²² and bicontinuous network of ionic clusters embedded in a matrix of fluorocarbon chains within Nafion recently proposed by Elliott and co-workers.²³

Besides bulk morphology, surface morphology of Nafion has also caused researchers’ interest in that surface morphology and properties of PEMs that consist of Nafion film is crucial in determining PEMFC performance.^{24,25} A powerful technique to study the surface morphology is Grazing Incident SAXS (GISAXS).^{26,27} By utilizing GISAXS, Bass and co-workers^{28,29} found that spin coated Nafion would form micelles, and the orientation of these micelles would be affected by both the substrate and phase of water. Dura and co-workers³⁰ also investigated the interface structures in Nafion, and observed alternating water-rich and Nafion-rich multilamellar structures when Nafion was cast onto SiO₂ surface. While these multilamellar structures were not observed for Nafion cast onto Au or Pt surface due to a lower affinity to the sulfonic acid/water phase. A recent study by Modestino and co-workers³¹ using in-situ GISAXS showed that the surface structure of Nafion could be manipulated via wetting interactions on different substrates, and also confirmed that the surface structure of Nafion is dependent on the properties of the substrate.

In the above studies, the sulfonic acid groups within Nafion were either used as acidic form or generally neutralized with small inorganic counterions that formed strong

electrostatic cross-links. These strong electrostatic cross-links prevent further melt processing and thermal disruption of the ionic domain structures. However, utilization of large tetra alkyl ammonium counterions greatly reduces electrostatic interactions within the ionic networks, so greater chain mobility and flow can be achieved.^{14,32,33} The enhanced mobility allows melt processing of Nafion and also provides additional methods to probe and manipulate the bulk and surface morphology of Nafion.

In this work, the surface structures of Nafion neutralized with large tetra alkyl ammonium counterions were studied in details. Thermal annealing effect on the surface morphology of Nafion was also investigated. This work demonstrates that surface morphology of Nafion can be controlled by varying counterions within Nafion, as well as thermal annealing processes.

5.2 Experimental Section

5.2.1 Materials

Nafion 117CS (1100EW, sulfonic acid form) was purchased from E. I. DuPont Company. Tetramethyl ammonium hydroxide and tetrabutyl ammonium hydroxide were purchased from Aldrich Chemical Co., and used as-received without further purification.

5.2.2 Preparation of Neutralized Perfluorinated Sulfonic Acid (PFSA) Membranes

Nafion 117CS membranes were cleaned by refluxing them in HNO₃ (8M) for 2 h to remove impurities, then washed with deionized (DI) water three times, and boiled in DI water for 1 h. The cleaned membranes were first immersed in 1 M tetramethylammonium (TMA) hydroxide or tetrabutylammonium (TBA) hydroxide overnight at room temperature, then heated up to 70 °C for 2 h. Membranes were washed and then boiled in

DI water for another hour. Finally all membranes were dried at room temperature between Kim wipes for an hour and placed in a vacuum oven for 12 h at 70 °C.

5.2.3 Preparation of Nafion Dispersion

14 g of TMA⁺-Nafion membrane was dissolved in 300 ml of water and ethanol mixture (50/50 in volume) at 200 °C for 2 h in a PARR pressure reactor to yield 5% w/v solution. For TBA⁺-Nafion, 300 ml of water, methanol, and isopropanol (40/30/30 in volume) mixture was used as the solvent and it followed the same procedure as the preparation of TMA⁺-Nafion dispersion. The obtained solutions were filtered through 5 µm pore size filter paper to remove dust particles and aggregates.

5.2.4 Thin Film Preparation

Silicon substrates were cleaned by immersing into a 7/3 v/v solution of sulfuric acid/hydrogen peroxide, followed by a rinse with ultrapure water and drying with nitrogen. The Nafion dispersion was spin coated onto silicon substrate at a spinning speed of 3000 rpm for 1 min.

For the annealing samples, the films were annealed under the specific annealing temperature in a high-vacuum oven for desired time.

5.2.5 SAXS/GISAXS

SAXS/GISAXS experiments were performed using a Rigaku S-Max 3000 3 pinhole SAXS system, equipped with a station for grazing experiments. The X-rays had a wavelength of 0.154 nm (Cu K_α), and two-dimensional SAXS/GISAXS patterns were obtained using a fully integrated 2D multiwire, proportional counting, gas-filled detector, with an exposure time of 2 h. For all scattering experiments the q-range was calibrated using a silver behenate standard. All SAXS/GISAXS data were analyzed using the

SAXSGUI software package to obtain radially integrated intensity versus scattering vector q , where $q=(4\pi/\lambda)\sin(\theta)$, θ is half of the scattering angle and λ is the wavelength of X-ray.

5.3 Results and Discussion

An incident angle 0.2° , which is above the critical angle of Nafion films,²⁸ and below that of silicon, was used to probe the morphological differences between different forms of Nafion under different conditions. Figure 5.2 presents a series of GISAXS scattering patterns obtained from TMA⁺-Nafion films spin coated onto silicon substrates. All of these patterns showed a scattering halo at $q \approx 0.2 \text{ nm}^{-1}$, which is the typical peak position of the ionic peak within Nafion.^{9,10} However, it is also noticeable here that the scattering halo became more anisotropic as annealing temperature increased. The Herman's orientation function^{34,35} was calculated using Eqn. 5.1 to further prove this anisotropic behavior in these scattering patterns,

$$f = \frac{3\langle \cos^2 \chi \rangle - 1}{2} \quad (5.1)$$

where χ is the azimuthal angle and $\langle \cos^2 \chi \rangle$ can be calculated using the following equation,

$$\langle \cos^2 \chi \rangle = \frac{\int_{\chi_1}^{\chi_2} I(\chi) \cos^2 \chi \sin \chi d\chi}{\int_{\chi_1}^{\chi_2} I(\chi) \sin \chi d\chi} \quad (5.2)$$

An f value of 1 indicates a system with perfect orientation of the scattering entities parallel to the director, an f value of -0.5 indicates that orientation of the scattering entities is perpendicular to the director, and an f value of 0 indicates an isotropic sample.^{9,10} The results listed in Table 5.1 show that f value decreases and approaches to -0.5, indicating

that the ionic domains are more preferred to align parallel to the substrate surface under high annealing temperature, which is in agreement with the atomic force microscopic (AFM) and conductivity results by Kwon and co-workers.³⁶

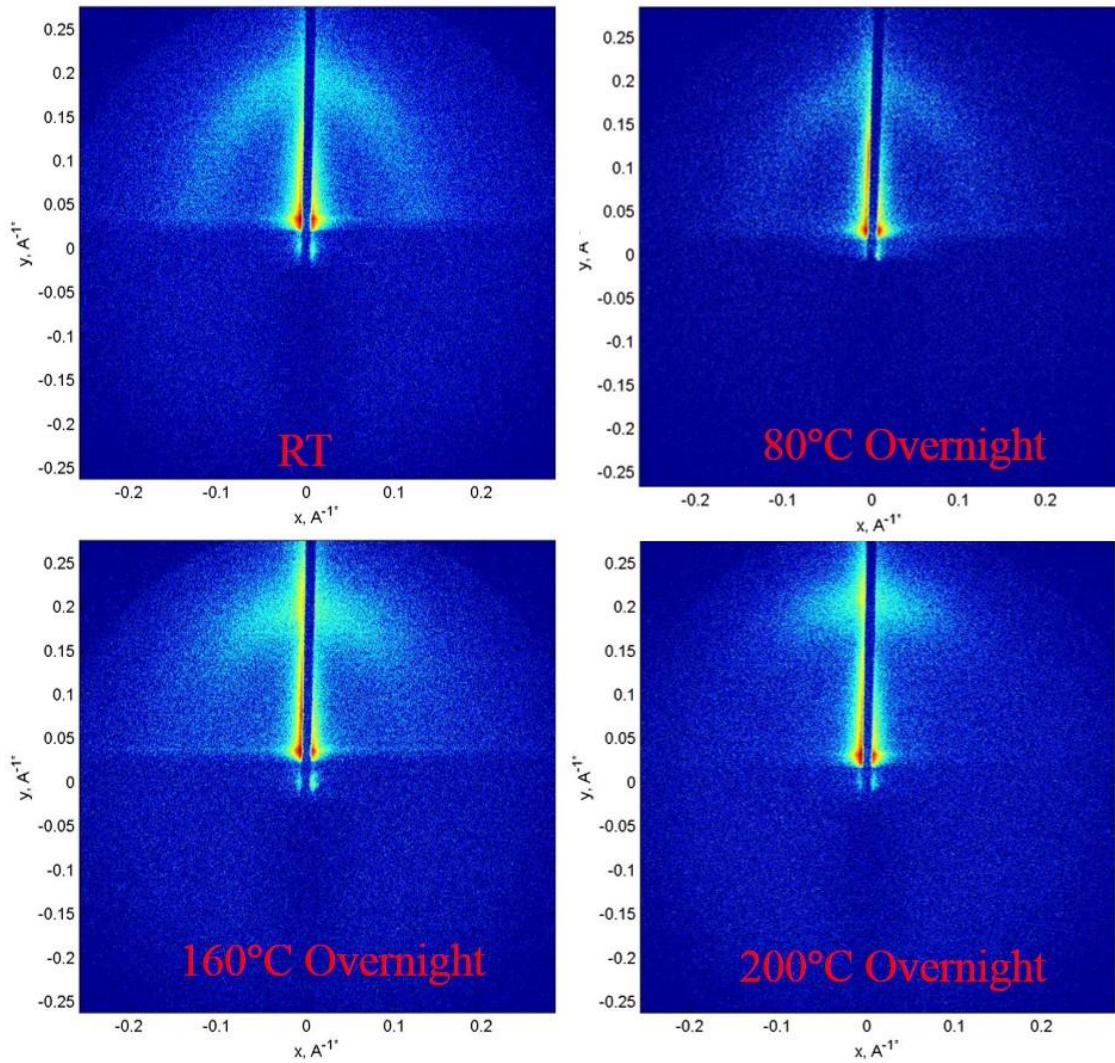


Figure 5.2. TMA⁺-Nafion films annealed at different temperatures overnight

Table 5.1. Herman's orientation f vs. annealing temperature for TMA⁺-Nafion

Annealing Temperature	Room Temperature (25 °C)	80 °C	160 °C	200 °C
f	-0.20	-0.23	-0.25	-0.30

To further examine thermal annealing effect on the surface structure of Nafion thin films, GISAXS scattering patterns were also obtained for TMA⁺-Nafion samples annealed under 200 °C for different time (Figure 5.3). It was observed that the scattering patterns of Nafion films annealed for 1 min, 2 min, 4 min, 16 min, 32 min and 64 min were almost identical. Furthermore, GISAXS scattering patterns of TMA⁺-Nafion were also obtained for samples annealed for 1 min and 10 min under different temperatures as shown in Figure 5.4. When Nafion films were annealed under the same temperatures, no clear difference in scattering patterns was observed between samples annealed for 1 min and 10 min. These patterns also showed a gradual increase in the anisotropy of the ionic peak as annealing temperature was increased, which is consistent with the observations in Figure 5.2 for samples annealed overnight. GISAXS patterns obtained on TBA⁺-Nafion thin films showed similar scattering behaviors, which suggests that annealing time does not act as a crucial factor on morphological rearrangement due to the great chain mobility in both TMA⁺ and TBA⁺-Nafion.^{14,32} However, the scattering patterns of TBA⁺-Nafion are more isotropic compared with those of TMA⁺-Nafion, indicating that a more random distribution of the ionic domains was formed when TBA⁺-Nafion film was spin coated onto silicon substrate. Since TBA⁺ ions are more hydrophobic than TMA⁺ ions, this may suggest that the interactions between the hydrophilic silicon substrate and the ionic domains within

Nafion would strongly affect the morphology of Nafion thin film, which is in agreement with previous work by Bass and co-workers.^{28,29}

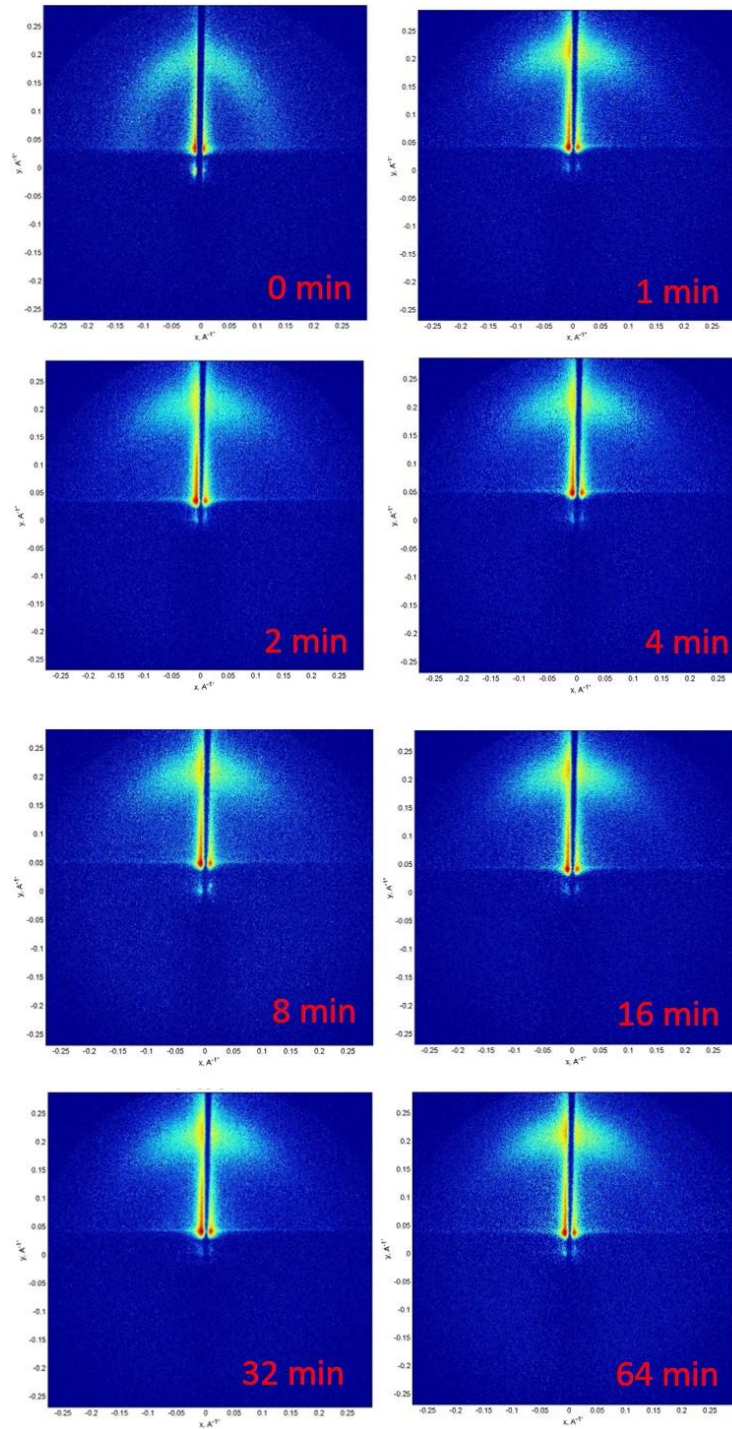


Figure 5.3. TMA⁺-Nafion films annealed under 200 °C for different time

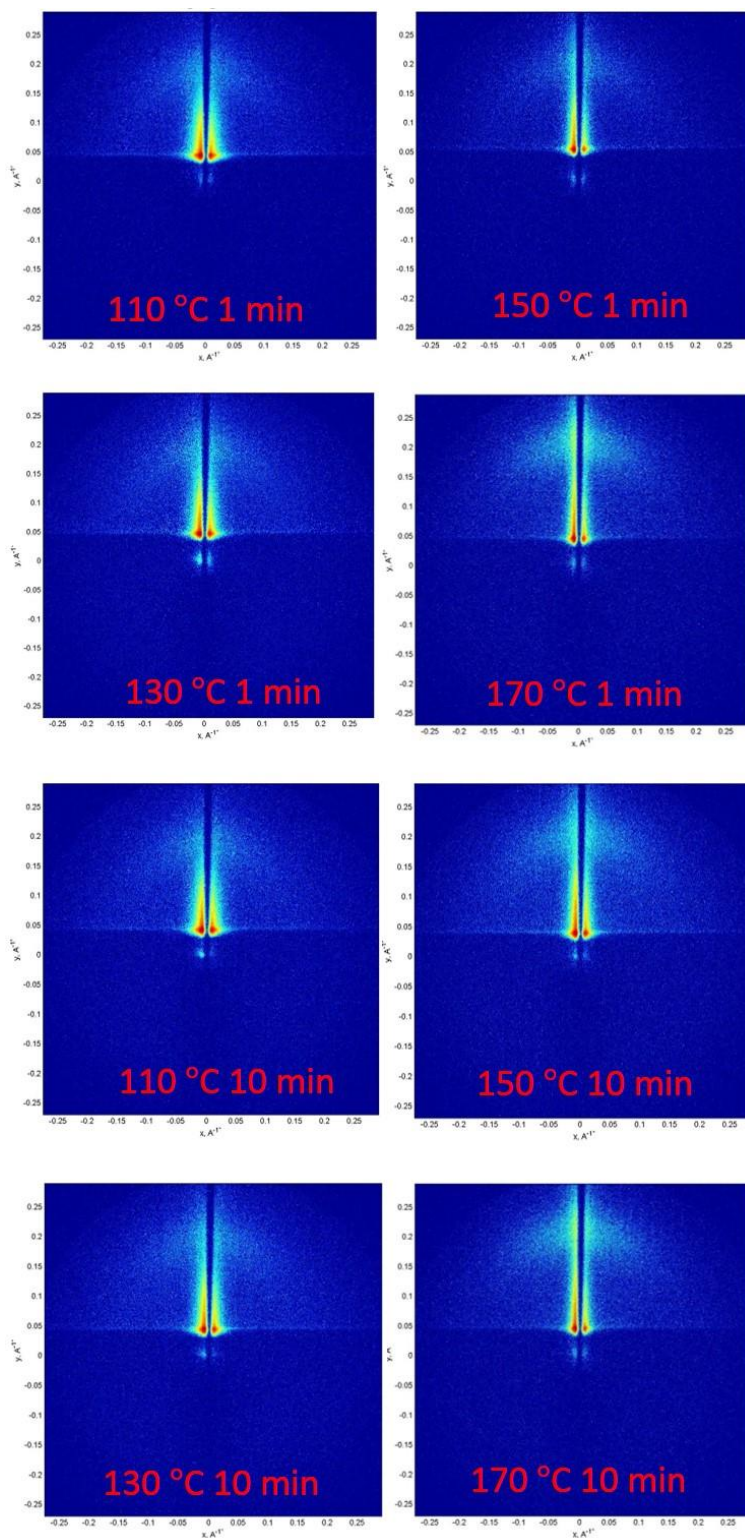


Figure 5.4. TMA⁺-Nafion films annealed for 1m under different temperatures

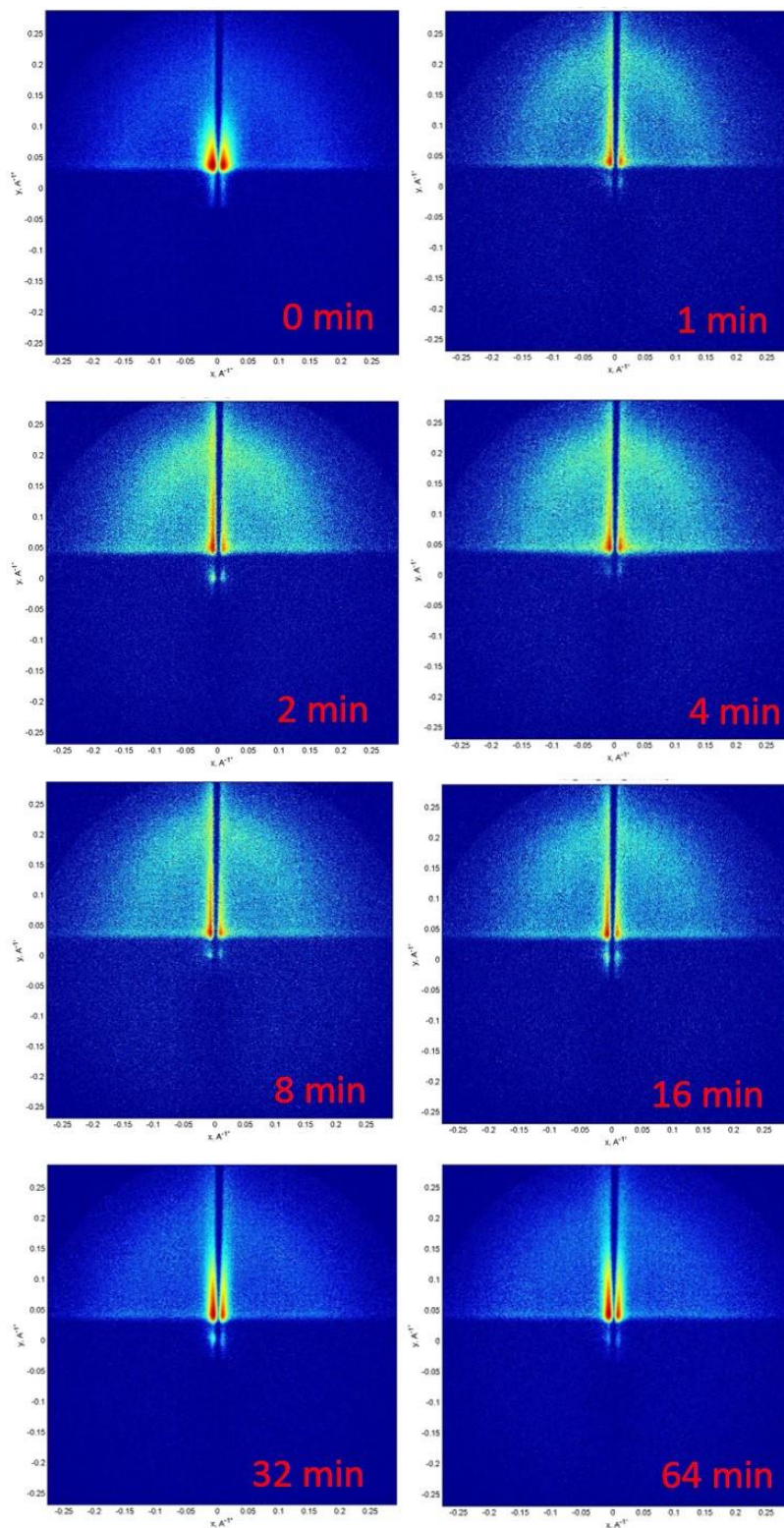


Figure 5.5. TBA⁺-Nafion films annealed under 90 °C for different time

To further examine thermal annealing effect on the morphology of Nafion, TMA⁺- and TBA⁺-Nafion 117 membranes annealed for different time under 200 °C, and 90 °C, respectively, were prepared for SAXS measurement. The GISAXS and SAXS scattering profiles (Figure 5.6) show that the ionic peak positions for TMA⁺-Nafion thin film and TMA⁺-Nafion 117 membrane are almost identical, which suggests that the average dimensions between the ionic domains are the same for both TMA⁺-Nafion thin film and TMA⁺-Nafion 117 membrane. For TBA⁺-Nafion (Figure 5.7), identical ionic peak positions for TBA⁺-Nafion thin film and TBA⁺-Nafion 117 membrane were also observed. It needs to point out that for TMA⁺-Nafion, SAXS data for both thin film and membrane show a sharper ionic peak when annealed at 200 °C, which is due to thermally induced ordering effect. This is because of narrower distribution of the ionic domain separations as sample temperature approaches the α -relaxation temperature of TMA⁺-Nafion as discussed in Park and co-workers' study.³⁷ While for TBA⁺-Nafion, this thermally induced ordering effect was neither observed in TBA⁺-Nafion thin film nor TBA⁺-Nafion 117 membrane, which is also consistent with Park and co-workers' work.

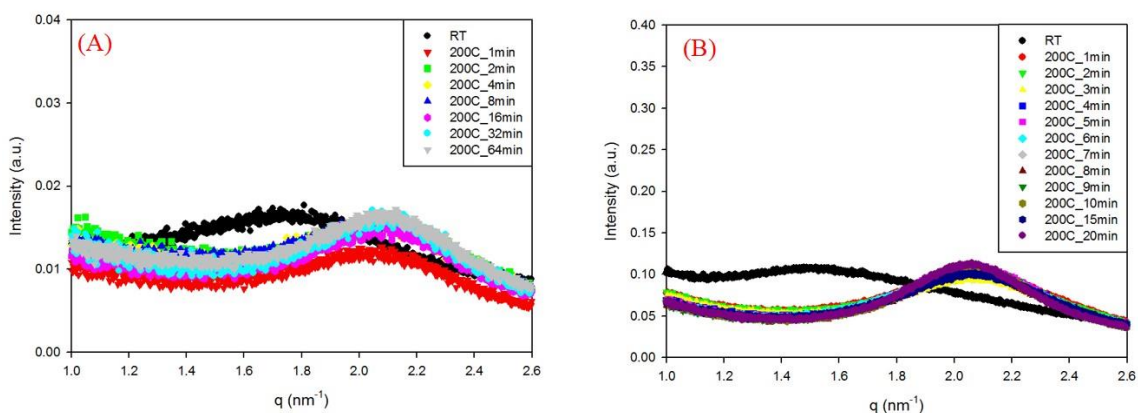


Figure 5.6. GISAXS and SAXS scattering files of TMA⁺-Nafion thin film spin coated on silicon(A), and TMA⁺-Nafion 117 membrane(B) annealed under 200 °C for different time

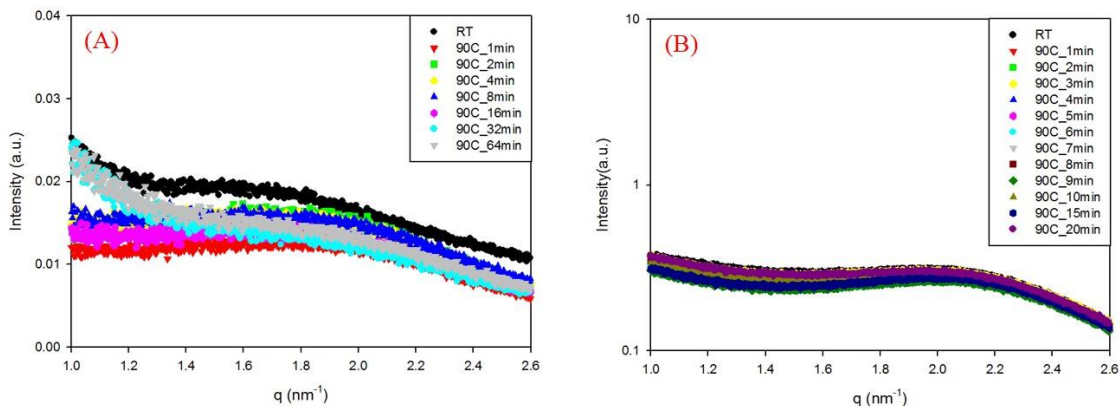


Figure 5.7. GISAXS and SAXS scattering files of TBA⁺-Nafion thin film spin coated on silicon(A), and TBA⁺-Nafion 117 membrane(B) annealed under 90 °C for different time

Besides the differences in the thermally ordering effect between TMA⁺- and TBA⁺-Nafion, an elliptical scattering pattern with larger q value in the thickness direction than that of the surface direction was observed for TMA⁺-Nafion thin film. To further examine this scattering behavior, a series of TMA⁺/TBA⁺- mixture Nafion thin films with varying TMA⁺/TBA⁺ contents were prepared for GISAXS measurements. These Nafion thin films were annealed under 100 °C and 200 °C, respectively, prior to the GISAXS experiments.

At lower content of TMA⁺-Nafion, elliptical scattering was observed when the film was unannealed or annealed under 100 °C, with a higher scattering intensity in the thickness direction than that in the surface direction. This is strong evidence that cylindrical structures which contain ionic aggregates are more preferentially arranged parallel to the surface direction.^{27,36} However, when these films were annealed under 200 °C, both the elliptical scattering and anisotropic scattering disappeared, indicating that these cylindrical structures that contain more TBA⁺ ions are more randomly distributed when provided with more thermal energy. When the amount of TMA⁺-Nafion dominated in the thin film, the elliptical scattering and anisotropic scattering preserved even under high annealing temperature, which is attributed to the higher affinity between the more hydrophilic TMA⁺ ions and the hydrophilic silicon substrate, and this keeps the cylindrical structures parallel to the substrate.

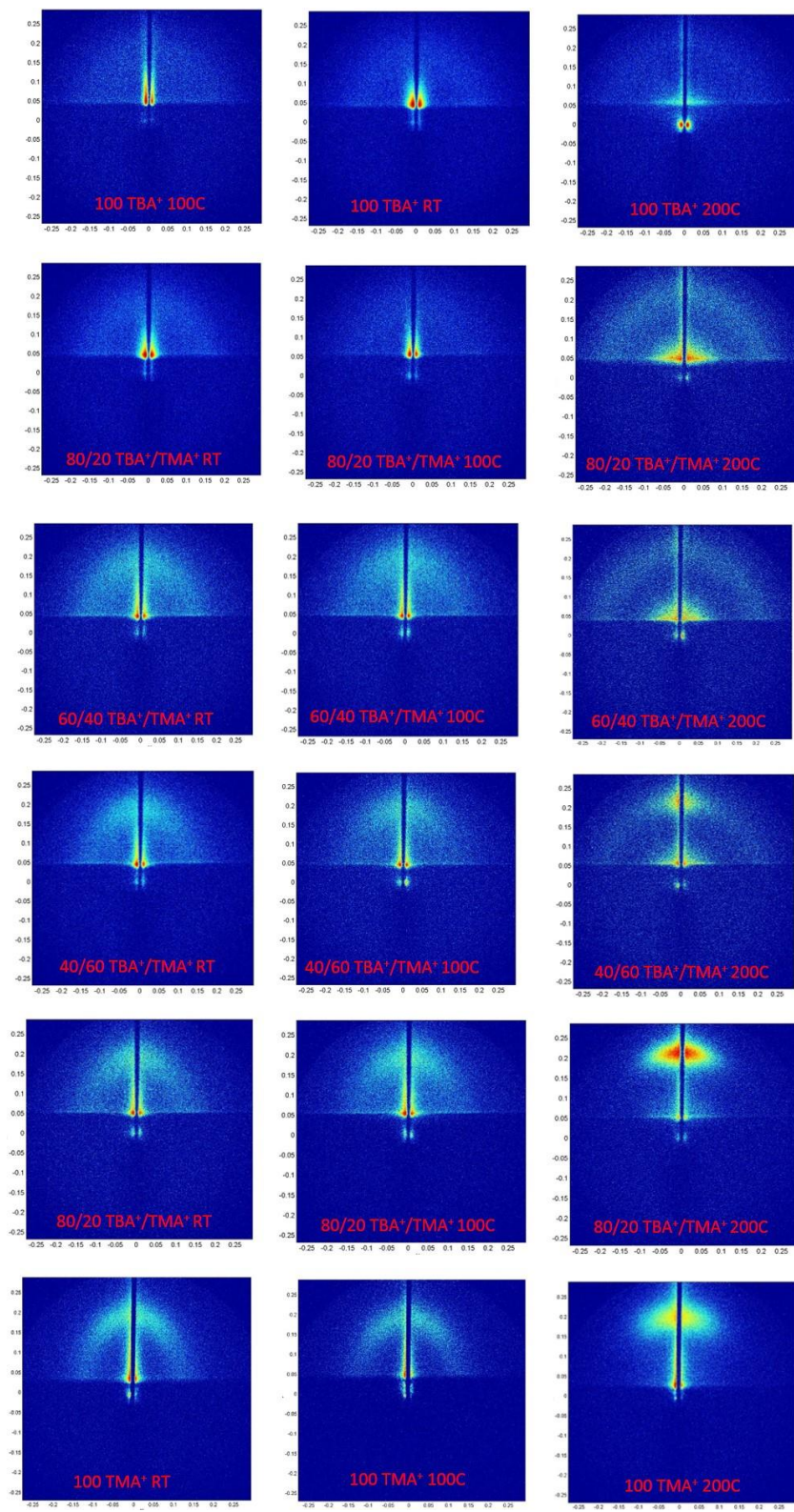


Figure 5.8. GISAXS patterns of TMA⁺/TBA⁺ mixture with different ratios under different temperatures

5.4 Conclusions

GISAXS experiments on Nafion thin films showed that the use of different counterions in Nafion would affect the surface morphology of Nafion thin film. For TMA⁺-Nafion, the ionic domains would form cylindrical structures that are aligned parallel to the silicon substrate. While for TBA⁺-Nafion, the cylindrical structures would prefer a more random distribution on silicon substrate.

Furthermore, annealing temperatures have a huge effect on the surface structure of these Nafion thin films. Higher annealing temperature on TMA⁺-Nafion would result in a larger degree of the alignment of the cylindrical structures. On the other hand, when TBA⁺-Nafion films were annealed under higher temperatures, the cylindrical structures would tend to be more randomly distributed. This scattering behavior in Nafion thin film was further demonstrated with variable TMA⁺/TBA⁺ contents annealed under different temperatures. This is attributed to the difference in the hydrophobicity between TMA⁺ and TBA⁺ ions in that more hydrophilic TMA⁺ ions will have a higher affinity with the hydrophilic silicon substrate.

The findings of this work demonstrate that the use of TMA⁺ and TBA⁺ ions would provide a means for one to manipulate the surface structures within Nafion thin film. Besides, thermal annealing under different temperatures would also help to control the surface morphology of Nafion thin films.

5.5 Acknowledgements

We thank graduate student Chao Wang for his assistance and helpful discussions on spin coating process. We also thank Professor A. R. Esker's group on sharing their spin

coater. This material is partially based upon work supported by the National Science Foundation under Grant No. DMR-0923107.

5.6 References

- (1) Mauritz, K. A.; Moore, R. B. *Chemical Reviews* **2004**, *104*, 4535.
- (2) Mohsen, S.; Kwang, J. K. *Smart Materials and Structures* **2001**, *10*, 819.
- (3) Roche, E. J.; Pineri, M.; Duplessix, R.; Levelut, A. M. *Journal of Polymer Science: Polymer Physics Edition* **1981**, *19*, 1.
- (4) Rollet, A.-L.; Diat, O.; Gebel, G. *The Journal of Physical Chemistry B* **2002**, *106*, 3033.
- (5) Rubatat, L.; Rollet, A. L.; Gebel, G.; Diat, O. *Macromolecules* **2002**, *35*, 4050.
- (6) Rubatat, L.; Gebel, G.; Diat, O. *Macromolecules* **2004**, *37*, 7772.
- (7) Kim, M.-H.; Glinka, C. J.; Grot, S. A.; Grot, W. G. *Macromolecules* **2006**, *39*, 4775.
- (8) Roche, E. J. S., R. S.; Russell, T. P.; MacKnight, W. J. *J. Polym. Sci., Polym. Phys. Ed.* **1980**, *18*, 1497.
- (9) Fujimura, M.; Hashimoto, T.; Kawai, H. *Macromolecules* **1981**, *14*, 1309.
- (10) Fujimura, M.; Hashimoto, T.; Kawai, H. *Macromolecules* **1982**, *15*, 136.
- (11) Moore, R. B.; Martin, C. R. *Macromolecules* **1988**, *21*, 1334.
- (12) Haubold, H. G.; Vad, T.; Jungbluth, H.; Hiller, P. *Electrochimica Acta* **2001**, *46*, 1559.
- (13) Page, K. A.; Cable, K. M.; Moore, R. B. *Macromolecules* **2005**, *38*, 6472.

- (14) Page, K. A.; Landis, F. A.; Phillips, A. K.; Moore, R. B. *Macromolecules* **2006**, *39*, 3939.
- (15) Song, J. M., Park, Jong Keun, Moore, Robert B. *To be submitted* **2012**.
- (16) Park, J. K.; Li, J.; Divoux, G. M.; Madsen, L. A.; Moore, R. B. *Macromolecules* **2011**, *44*, 5701.
- (17) Gierke, T. D.; Munn, G. E.; Wilson, F. C. *Journal of Polymer Science: Polymer Physics Edition* **1981**, *19*, 1687.
- (18) Hsu, W. Y.; Gierke, T. D. *Journal of Membrane Science* **1983**, *13*, 307.
- (19) Litt, M. *Polym. Prepr.* **1997**, *38*, 80.
- (20) van der Heijden, P. C.; Rubatat, L.; Diat, O. *Macromolecules* **2004**, *37*, 5327.
- (21) Rubatat, L.; Diat, O. *Macromolecules* **2007**, *40*, 9455.
- (22) Schmidt-Rohr, K.; Chen, Q. *Nat Mater* **2008**, *7*, 75.
- (23) Elliott, J. A.; Wu, D.; Paddison, S. J.; Moore, R. B. *Soft Matter* **2011**.
- (24) Zawodzinski Jr, T. A.; Springer, T. E.; Uribe, F.; Gottesfeld, S. *Solid State Ionics* **1993**, *60*, 199.
- (25) He, Q.; Kusoglu, A.; Lucas, I. T.; Clark, K.; Weber, A. Z.; Kostecki, R. *The Journal of Physical Chemistry B* **2011**, *115*, 11650.
- (26) Levine, J. R.; Cohen, J.; Chung, Y.; Georgopoulos, P. *Journal of Applied Crystallography* **1989**, *22*, 528.
- (27) Müller-Buschbaum, P. In *Applications of Synchrotron Light to Scattering and Diffraction in Materials and Life Sciences*; Gomez, M., Nogales, A., Garcia-Gutierrez, M. C., Ezquerra, T. A., Eds.; Springer Berlin Heidelberg: 2009; Vol. 776, p 61.

- (28) Bass, M.; Berman, A.; Singh, A.; Konovalov, O.; Freger, V. *The Journal of Physical Chemistry B* **2010**, *114*, 3784.
- (29) Bass, M.; Berman, A.; Singh, A.; Konovalov, O.; Freger, V. *Macromolecules* **2011**, *44*, 2893.
- (30) Dura, J. A.; Murthi, V. S.; Hartman, M.; Satija, S. K.; Majkrzak, C. F. *Macromolecules* **2009**, *42*, 4769.
- (31) Modestino, M. A.; Kusoglu, A.; Hexemer, A.; Weber, A. Z.; Segalman, R. A. *Macromolecules* **2012**, *45*, 4681.
- (32) Page, K. A.; Cable, K. M.; Moore, R. B. *Macromolecules* **2005**, *38*, 6472.
- (33) Phillips, A. K.; Moore, R. B. *J Polym Sci Pol Phys* **2006**, *44*, 2267.
- (34) Silva, R. F.; De Francesco, M.; Pozio, A. *Electrochimica Acta* **2004**, *49*, 3211.
- (35) Nojima, S.; Kato, K.; Ono, M.; Ashida, T. *Macromolecules* **1992**, *25*, 1922.
- (36) Kwon, O.; Wu, S.; Zhu, D.-M. *The Journal of Physical Chemistry B* **2010**, *114*, 14989.
- (37) Park, J. K.; Spano, J.; Moore, R. B.; Wi, S. *Polymer* **2009**, *50*, 5720.

copolymers.⁹ These block copolymers always form microphase-separated morphology, with hydrophilic phases consist of sulfonated blocks, and hydrophobic phases consist of non-sulfonated blocks. This microphase-separated morphology acts as a key parameter in determining their fuel cell performance.¹⁰ Well-defined nanostructures can also be achieved in these block copolymers via proper choices of materials and synthetic approach.⁹

However, sulfonated block copolymers have the drawback that they become very brittle when drying out, which leads to very poor mechanical properties in fuel cell applications.¹¹ One method to overcome this is to blend the block copolymer with another polymer. Some common polymer blends for fuel cell applications include sulfonated poly(etheretherketone) PEEK Victrex[®] and polysulfone Udel[®]-ortho-sulfone-diamine blend,¹² sulfonated poly(etheretherketone) sPEEK and poly(4-vinylpyridine) blend,¹¹ polybenzimidazole (PBI) and polysulfone (PSF) blend,¹³ sulfonated polystyrene (sPS) and sulfonated poly(2,6-dimethyl-1,4-phenylene oxide) (sPPO) blend.¹⁴ However, to understand how blends work as a better candidate for fuel cell applications, there still needs fundamental understanding of the morphology of these blends, and how morphology affects the properties of these blends.

In this work, we focused on the morphological analysis of the sulfonated block copolymer that was synthesized by General Motors[®] (GM[®]). To enhance the mechanical properties of this sulfonated block copolymer, we blended it with Knar Flex and found the best blending ratio between this sulfonated block copolymer and Knar Flex by means of proton conductivity measurement and small angle X-ray scattering (SAXS) experiments. Finally, a detailed morphological study on the blend was performed.

6.2 Experimental Section

6.2.1 Materials

The sulfonated block copolymer from GM[®] consists of sulfonated and non-sulfonated blocks. The sulfonated block consists of poly(biphenyl vinyl ether-perfluorocyclobutane) (BVPE-PFCB), with perfluoroether side chains capped with sulfonic acid groups. The non-sulfonated block is also a BVPE-PFCB polymer, with two trifluoromethyl groups inserted between the aromatic rings, and the structure of this sulfonated block copolymer (we would use the name “PFCB ionomer” for simplicity) is shown in Figure 6.2. Sodium hydroxide, cesium hydroxide, and dimethylacetamide (DMAc) were obtained from Aldrich Chemical Co., and used as-received without further purification.

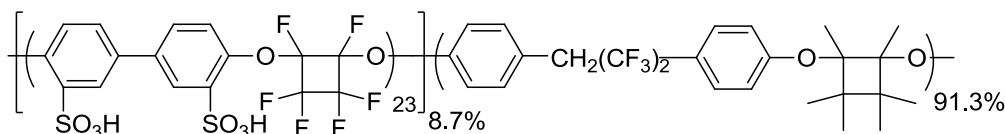


Figure 6.2. Chemical Structure of sulfonate block copolymer from GM[®]

Knar Flex (KF) used in this study was also received from GM[®], with a product name KF 2751. KF 2751 is a random copolymer of poly vinylidene difluoride (85 mol%) and poly hexafluoropropylene (15 mol%), and the molecular weight is around 380,000. The structure of KF is shown in Figure 6.3.

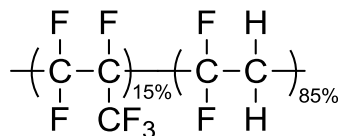


Figure 6.3. Chemical Structure of KF from GM[®]

6.2.2 Membrane Casting Procedure

All pure component membranes were prepared at Virginia Tech (VT cast). These membranes were obtained via solution casting, using the same procedure employed by

GM[®]. First 5 gram of polymer was mixed with 45 g DMAc. Then the solution was homogenized at 24,000 RPM for 5 minutes, and left overnight. Then the solution was filtered through 5 μm pore size filter paper to remove residual aggregates. Glass was used as casting substrate and the solution was placed on top of the casting glass at room temperature. Then casing temperature was quickly ramped to 80 $^{\circ}\text{C}$ and was held at 80 $^{\circ}\text{C}$ for 1 hour. Then the membrane was air cooled to room temperature. The whole casting glass with the membrane on top was placed in water for 1 hour, or until the membrane floated off. Then membrane was removed from the glass or water and stored in a sealed plastic bag.

In addition, unless otherwise specified, all membranes underwent a standardized water bath procedure to remove the residual DMAc as follows. The membrane was fixed onto PTFE frame and the framed membrane was placed into deionized (DI) water at 50 $^{\circ}\text{C}$ for 1 hour. Then the framed membrane was placed in desiccator for 24 hours.

Neutralization was performed on the PFCB ionomer for SAXS measurements using the following procedures. The membrane was stirred in either 1M CsOH or NaOH solution (50/50 in weight, H₂O/Methanol mixture) for 12 hours at room temperature. Then the membrane was stirred in the same vial at 50 $^{\circ}\text{C}$ for 1 hour. Then the membrane was washed in DI water several times. After that the membrane was dried in a vacuum at 70 $^{\circ}\text{C}$ for 1 hour. Then the membrane was reintroduced into ambient conditions for several days before testing.

6.2.3 Small Angle X-ray Scattering

Small Angle X-ray Scattering (SAXS) experiments were performed using a Rigaku S-Max 3000 3 pinhole SAXS system, equipped with a rotating copper anode emitting X-rays

with a wavelength of 0.154 nm (Cu K α). Two-dimensional SAXS patterns were obtained using a fully integrated 2D multiwire, proportional counting, gas-filled detector, with an exposure time of 1 hour. All SAXS data were analyzed using the SAXSGUI software package to obtain radially integrated SAXS intensity versus scattering vector q , where $q=(4\pi/\lambda)\sin(\theta)$, θ is half of the scattering angle and λ is the wavelength of X-ray. For all scattering experiments the sample-to-detector distance was 1603 mm, and the q -range was calibrated using a silver behenate standard. For variable temperature SAXS experiments, samples were heated using a Linkam hot stage positioned in the sample chamber and held for 30 min to equilibrate at a given temperature before data acquisition. An exposure time of 1 hour was used for all samples. For SAXS on annealing samples, sample was heated to the experimental temperature at a rate of 10 C/min, and held at that temperature for half one hour to reach equilibrium, then measured for another hour. For each experiment, a new sample was used.

Absolute intensities were obtained by first determining the calibration scale factor. This factor was obtained by comparing the scattering pattern of a glassy carbon sample and the calibrated intensity of glass carbon from Argonne Photon Source (APS),¹⁵

$$\text{Scale Factor} = \left(\frac{\partial \Sigma}{\partial \Omega} \right)_{st} \bigg/ \frac{(I_{st}(q) - BG_{st})}{d_{st} T_{st}} \quad (6.1)$$

where d_{st} is the thickness of glass carbon, T_{st} is the transmission of glassy carbon, and BG_{st} is the background scattering.

Thus, absolute intensities of all the Nafion samples were obtained using the following equation, where d_s is the thickness of the sample, and T_s is the transmission of the sample.

$$\text{Absolute intensity} = \left(\frac{\partial \Sigma}{\partial \Omega} \right)_{st} \frac{(I_s(q) - BG_s)}{d_s T_s} \bigg/ \frac{(I_{st}(q) - BG_{st})}{d_{st} T_{st}} \quad (6.2)$$

6.2.4 Atomic Force Microscopy

All Atomic Force Microscopy (AFM) scans were performed on a Veeco Multimode Atomic Force Microscope. The free air (root mean square) RMS for every sample was 3 ± 0.05 mV, and the tapping RMS was 2.15 ± 0.05 mV. A high k tip was used for every sample. Every sample was run under ambient conditions.

6.2.5 Through Plane Proton Conductivity Measurement

Membrane through plane proton conductivity was measured by our collaborators from GM[®] using a conductivity cell from BakkTech[™] using humidified air and hydrogen at a flow rates of 2 L min^{-1} from a fuel cell test stand. Current was measured from applied voltages controlled by a computer equipped with a Gamry card (Gamry Instruments Inc., PA). The membrane was initially equilibrated at $80 \text{ }^\circ\text{C}$ and 20% relative humidity (RH) followed by step-wise humidification to 100% RH. The relative humidity was increased in 10% increment and held for thirty minutes at each step, followed by 5 consecutive measurements from 0-0.6 V at a sweep rate of 10 mV/sec prior to the next increase in RH.

6.3 Results and Discussion

AFM phase images on the pure H^+ -PFCB ionomer are presented in Figure 6.4. In Figure 6.4 (A), dark and light phases could be clearly observed, with dark phase corresponding to the “hard” phase that contains ionic groups and light phase corresponding to the “soft” phase that consists of amorphous phase. If zoomed in as shown in Figure 6.4 (B), a much clearer phase-separated morphology could be observed. However, it is very difficult to accurately quantify the shape or size of the different phases from these AFM images. Thus,

SAXS experiments were performed on different counterion forms of pure PFCB ionomer (H^+ , Na^+ , Cs^+ -forms) in order to obtain more detailed morphological information.

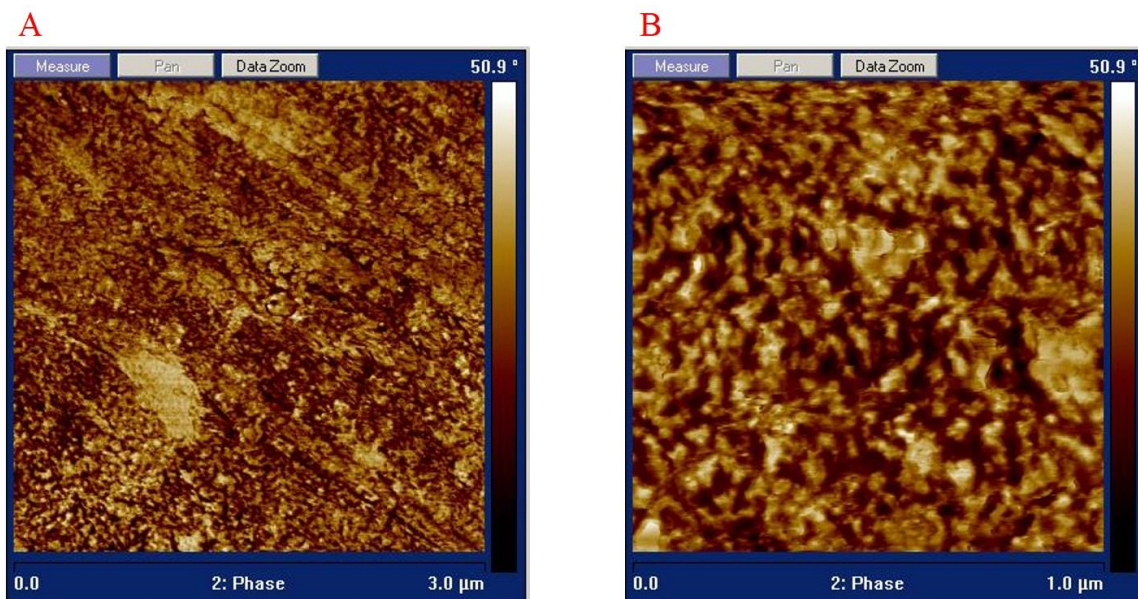


Figure 6.4. AFM images of H^+ -PFCB ionomer

SAXS profiles of different counterion forms of pure PFCB ionomer are presented in Figure 6.5. A peak was observed at around $q=0.28 \text{ nm}^{-1}$, which is the typical peak position corresponding to the dimensions between the phases within the block copolymer that has a phase-separated morphology.¹⁶ This phase-separated morphology is due to the difference in hydrophilicity between the two different blocks.^{17,18} From this peak position, one can estimate that the average distance between the phases is around 22 nm by using Bragg's law ($d=2\pi/q$).

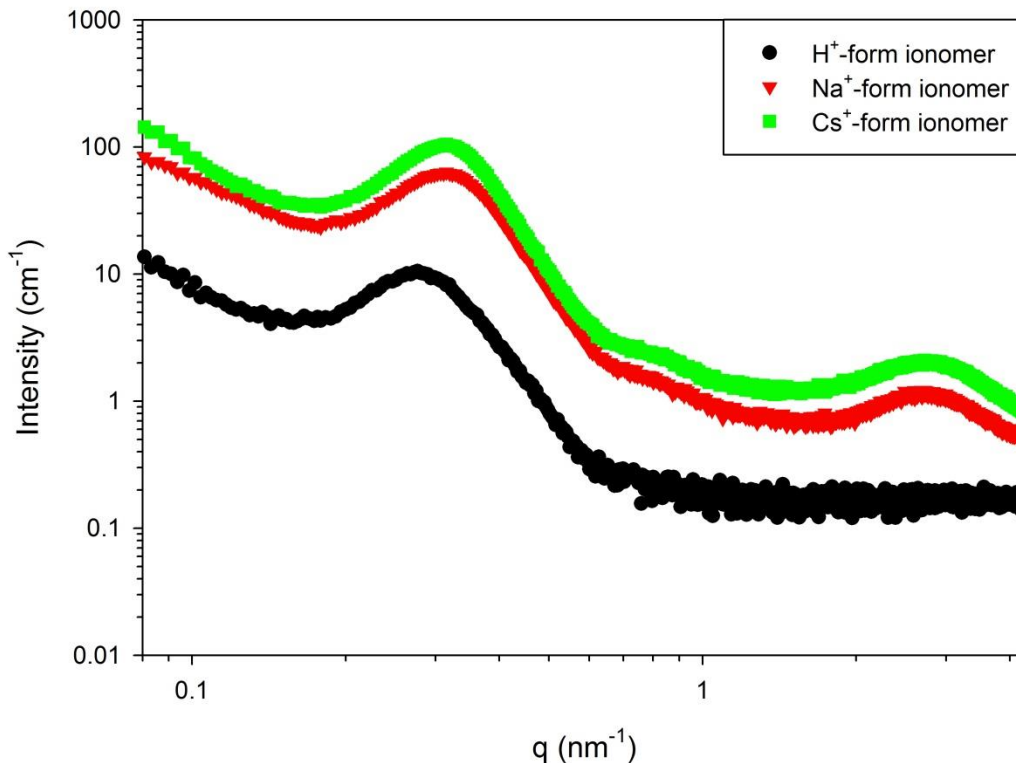


Figure 6.5. SAXS profiles of different counterion forms of pure PFCB ionomer

For H⁺-PFCB ionomer, the scattering profile is featureless at high q region. However, the SAXS profiles on both Na⁺ and Cs⁺-PFCB ionomers clearly show a scattering maxima at $q \approx 2.8 \text{ nm}^{-1}$, which is the typical peak position for ionic peak in ionomers.¹⁹⁻²¹ The appearance of this peak when H⁺-PFCB ionomer was neutralized with either NaOH or CsOH further demonstrates that it is related to the ionic regions that contain either Na⁺ ions or Cs⁺ ions. Thus, the scattering peak at $q \approx 2.8 \text{ nm}^{-1}$ is assigned as the “ionic peak” for PFCB ionomer. It also needs to point out here that this ionic peak is not usually observed for block ionomers that have highly ordered morphology.²²⁻²⁴ Based on both AFM and SAXS data, a morphological model was proposed for this PFCB ionomer as shown in Figure 6.6. In this model, the phase separation distance is between 20 and 30 nm. Ionic

aggregations are within the hydrophilic phase, which has an average distance of around 2.4 nm.

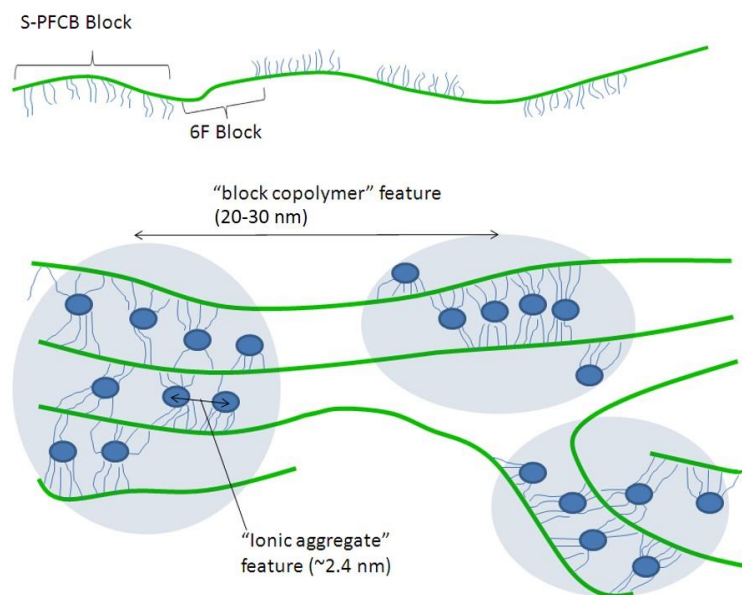


Figure 6.6. Proposed morphological model for pure PFCB ionomer

However, this pure PFCB ionomer is very brittle and has poor mechanical properties tested by GM[®]. In order to enhance its mechanical performance in fuel cell applications, Kynar Flex (KF) was used to blend with this ionomer. One key parameter needs to be figured out is the best ratio between PFCB and KF in order to achieve excellent properties in both conductivity and durability. To examine the effect of KF amount on the morphology of these blends, SAXS experiments were performed on a series of H⁺-PFCB/KF blends with variable compositions and the data are presented in Figure 6.7. The phase separation peak shifts to lower q values and becomes much broader with increasing KF amounts. It starts to become a shoulder when KF amount reaches 40 wt%, and eventually becomes indistinguishable when KF amount is above 80 wt%, indicating that the phase-separated morphology is strongly affected by increasing KF content. The detailed information on the phase separation peak is listed in Table 6.1, where the increase in full width at half maxima

(FWHM) clearly demonstrates that the phase separation peak becomes broader with increase in KF amount within the blend. Another shoulder at $q \approx 1 \text{ nm}^{-1}$ starts to appear when KF amount is at 40 wt%. Since KF has a fair amount of crystallinity demonstrated from previous Differential Scanning Calorimetry (DSC) studies,²⁵ this peak is attributed to the “crystalline peak” of KF. Thus, it is reasonable to conclude that a large change in the morphology of the blends has already resulted when KF amount is at 40 wt%.

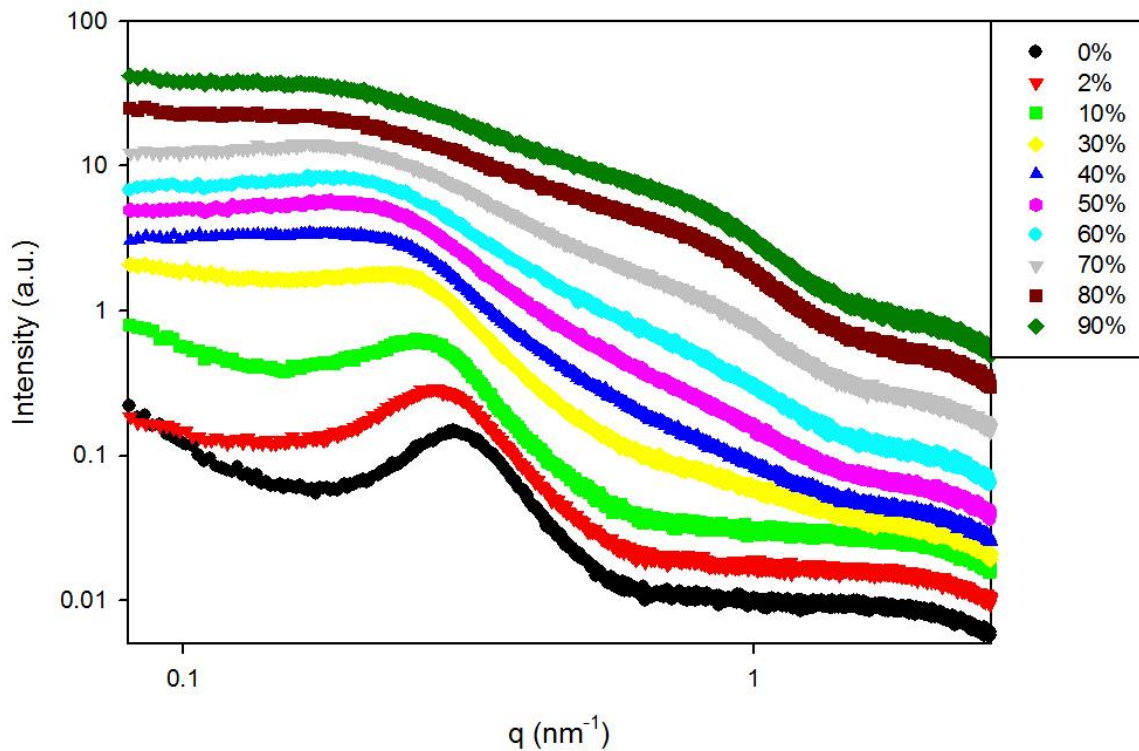


Figure 6.7. SAXS profiles of PFCB/Kynar Flex blends with variable weight percentages of Kynar Flex in the blends.

Table 6.1. Summary of SAXS results in Figure 6.7

KF Content	$q_{\max}(\text{nm}^{-1})$	d (nm)	Full width at half maxima (FWHM) (nm^{-1})
0%	0.30	21	0.13
2%	0.28	22	0.14
10%	0.26	24	0.14
30%	0.16	27	0.23
40%	0.22	29	0.16
50%	0.21	30	0.18
60%	0.19	33	0.21
70%	0.17	37	0.25
80%	0.11	57	0.40
90%	n/a	n/a	n/a

In order to study the effect of amount of KF content on the transport properties, through plane proton conductivity measurements under different RH were performed on PFCB/KF blends with variable KF content by our collaborators in GM[®] and the data are presented in Figure 6.8. It was observed that higher humidity would result in a higher through plane conductivity, which is due to an increase in the water content in the membrane.^{26,27} At a fixed RH, proton conductivity remains relatively constant when KF content is below 40 wt%, and decreases dramatically when KF content is at and above 40 wt%. This may indicate that when KF content is at 40 wt%, a large change in morphology has already resulted, which is consistent with the SAXS results shown in Figure 6.7.

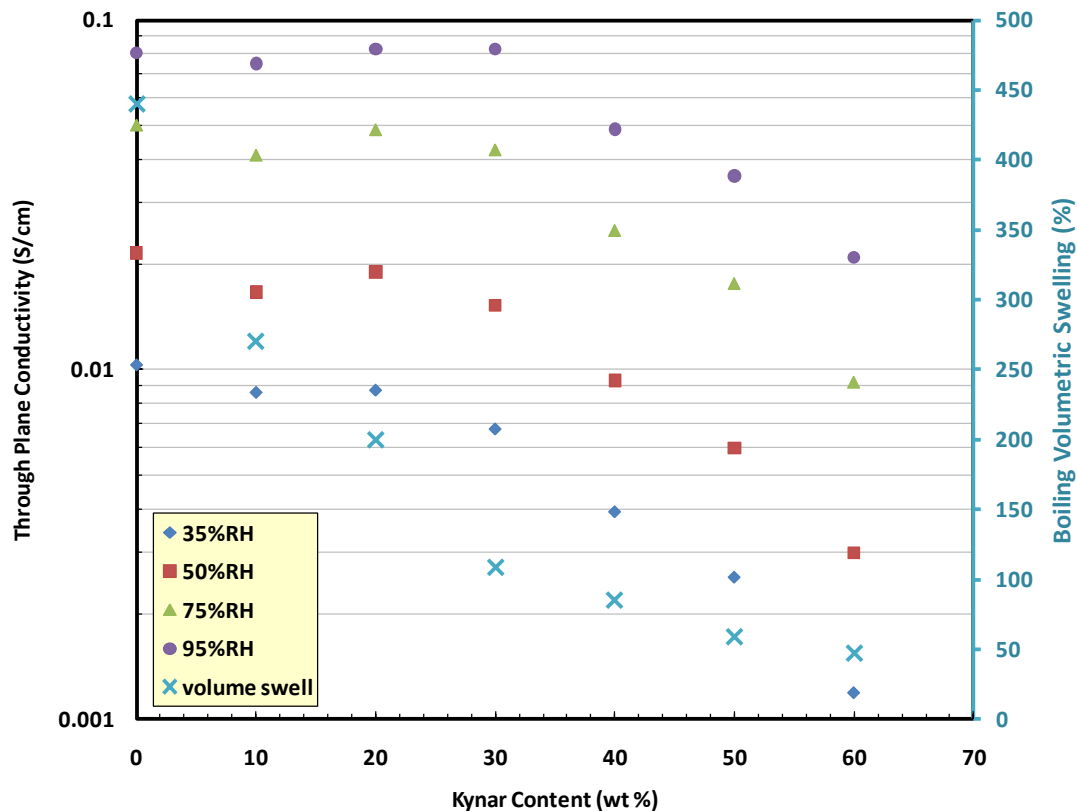


Figure 6.8. Through plane conductivity of PFCB/Kynar Flex blends with variable weight percentages of Kynar Flex in the blends, and data were acquired by R. Jiang at GM®

To further correlate morphology with transport properties, through plane conductivity at 35% RH, FWHM, and average distance between the phases from SAXS were plotted against KF content as presented in Figure 6.9. Through plane conductivity at 35% RH, FWHM, and distance all remained relatively unchanged when KF content was below 40 wt%, and they all changed dramatically when KF content was at and beyond 40 wt%. Figure 6.10 further demonstrates the correlation between morphology and proton transport properties by plotting through plane conductivity against FWHM and phase separation distance. A clear correlation between the conductivity and morphology could be observed, indicating the morphology plays an important role in determining the transport properties in these blends. As the distance between the phases increases and the distribution of these

phases becomes more random, the hydrophilic channels for proton transfer are more randomly distributed with a larger distance away from each other, resulting in a decrease in the overall through plane conductivity.

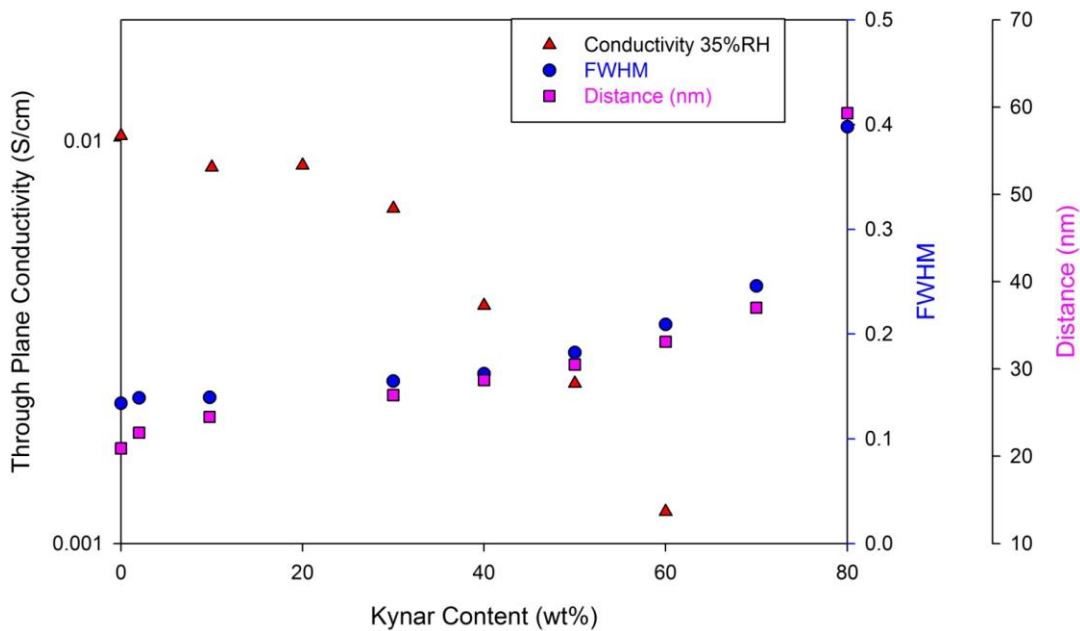


Figure 6.9. Through plane conductivity, FWHM, and distance between the phases vs. KF content in the blends

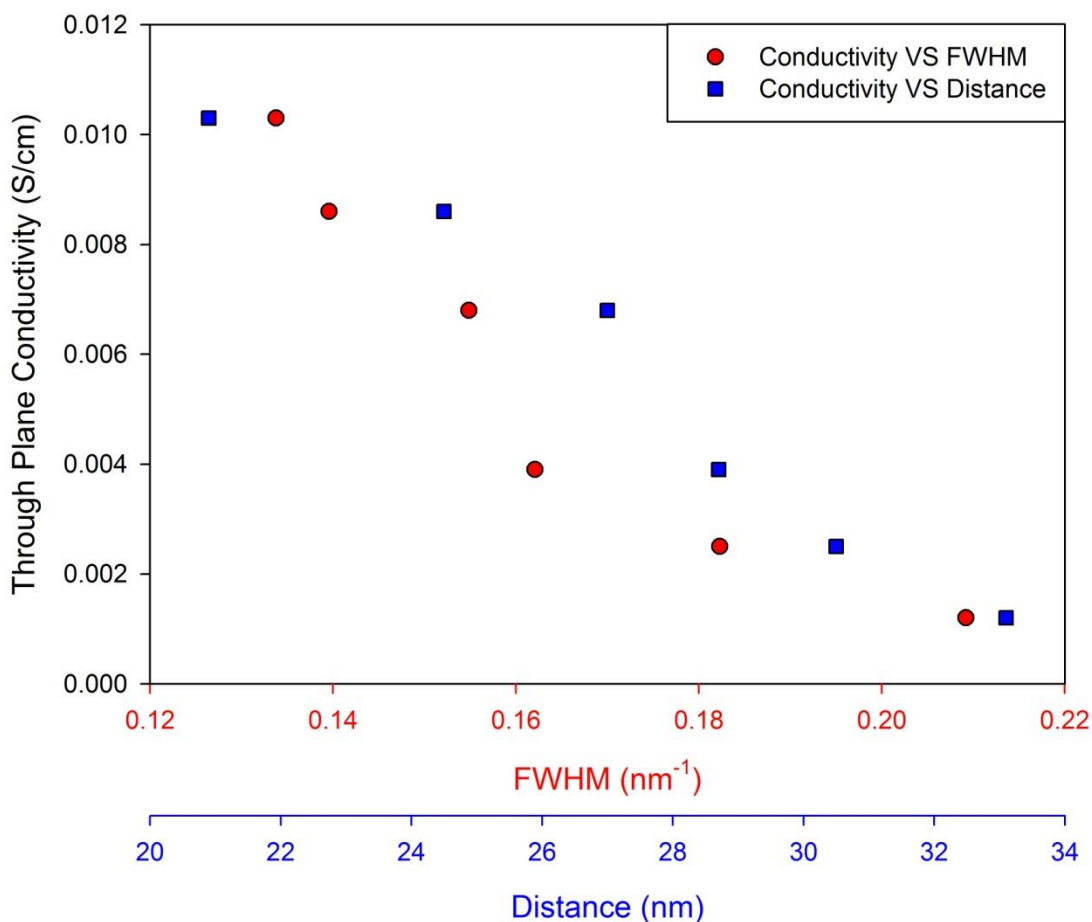


Figure 6.10. Through plane conductivity vs. FWHM, and distance between the phases at the same KF content

Given the conductivity and morphology data, 70/30 PFCB/KF was chosen as the best ratio for the blend, which has good conductivity as well as fair amount of KF in the blend to enhance mechanical properties. SAXS profiles of different counterion forms of 70/30 PFCB/KF blend are presented in Figure 6.11. Similar to the scattering profiles in Figure 6.5, these blends also show a phase separation peak at $q \approx 0.28 \text{ nm}^{-1}$. For H^+ -form blend, it is still featureless at higher q region, while clear ionic peaks at $q \approx 2.8 \text{ nm}^{-1}$ were observed for Na^+ - and Cs^+ -blends. The crystalline peak was not clearly observed in 70/30 PFCB/KF blend as also shown in Figure 6.7. However, a clear peak at $q \approx 0.82 \text{ nm}^{-1}$

was observed for both Na⁺- and Cs⁺- blends, and this peak position is very close to the position where the KF crystalline peak shows up in Figure 6.7 when KF content is relatively high. This may be due to the increase in electron density within the hydrophilic domains that contains either Na⁺ or Cs⁺ ions after neutralization, which results in a change in the electron density difference between the KF crystalline region and non-crystalline region that contains hydrophilic domains and amorphous phase. Thus this peak is confirmed to be the crystallinity peak of KF, and it corresponds to a distance of around 8 nm. Both the phase separation peak and the ionic peak are at the same positions as those in the pure PFCB ionomer, indicating that most of the KF in the blend are miscible with the hydrophobic domains, and does not cause a significant change in morphology at 70/30 blend ratio. Thus the through plane conductivity of 70/30 PFCB/KF blend is almost the same as that of the pure PFCB ionomer under the same RH due to little change in morphology.

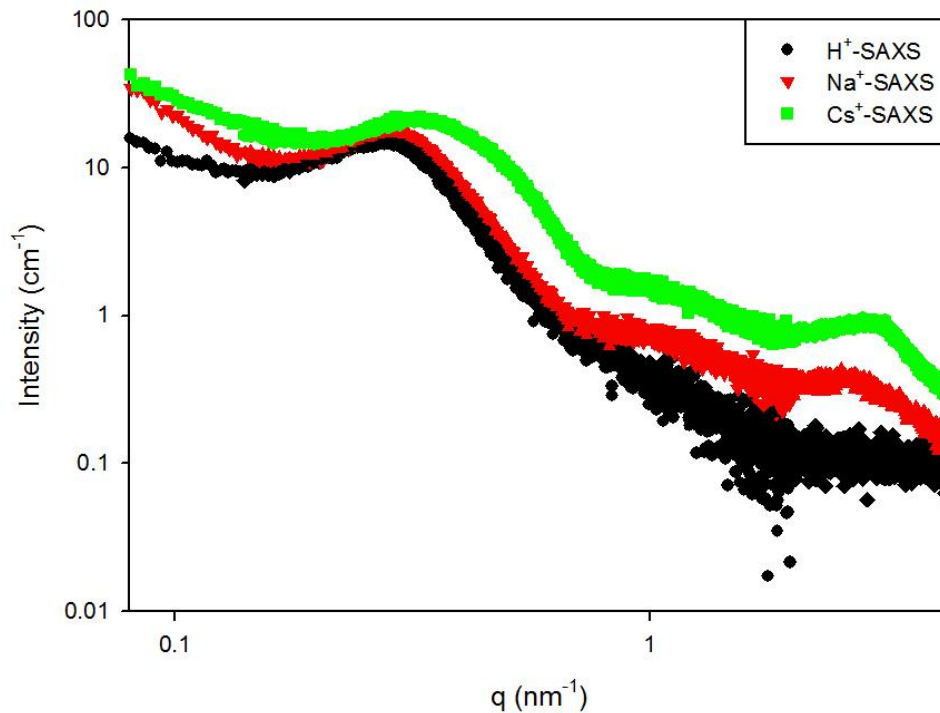


Figure 6.11. SAXS profiles of different counterion forms of 70/30 PFCB/Kynar Flex blend

Besides, the effects of thermal annealing on the blends were studied. Figure 6.12 presents the data of RH cycling lifetime vs. annealing condition and %KF that were obtained from GM[®]. It was observed that membranes that were annealed under 140 °C would result in a longer cycling life. In order to further examine the effect of annealing on the 70/30 blend, SAXS experiments were performed on blends annealed under different temperatures as shown in Figure 6.13. No clear change in the phase separation peak was observed. However, the crystalline peak becomes much clearer as annealing temperature was increased, indicating that thermal annealing would affect the crystallinity of Kynar Flex. However, when temperature was above 120 °C, an abnormal peak was observed at $q \approx 0.6 \text{ nm}^{-1}$, which may be due to the degradation of H⁺-blend membrane.

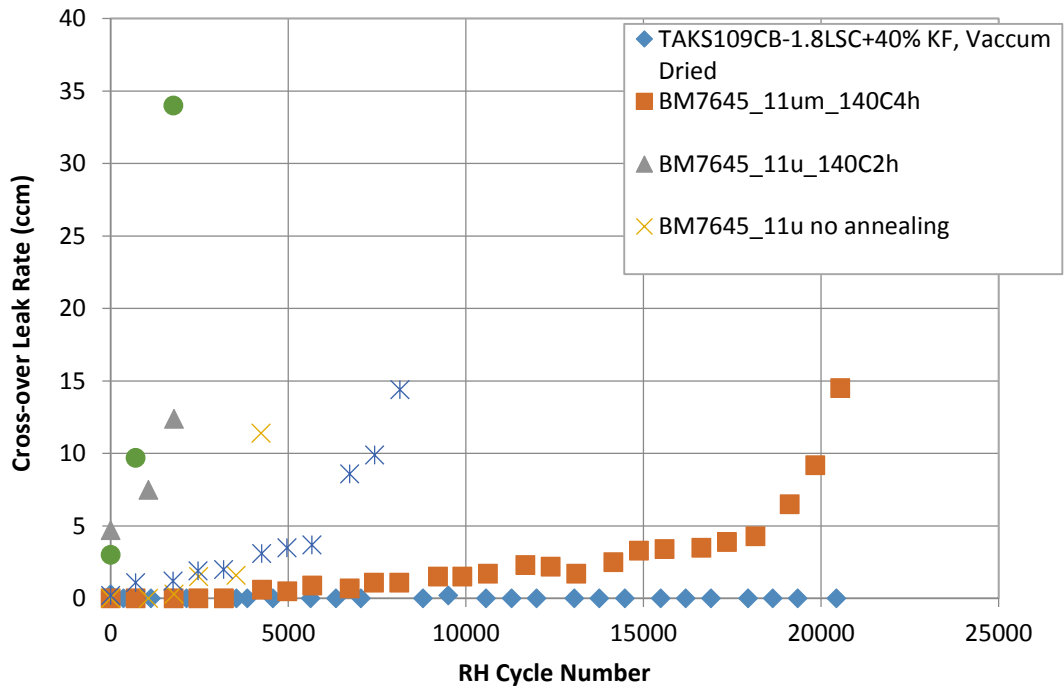


Figure 6.12. RH Cycling Lifetime vs. Annealing Condition and %KF (80 °C, 0-150%RH), and data were collected by L. Zou and T. Fuller at GM®

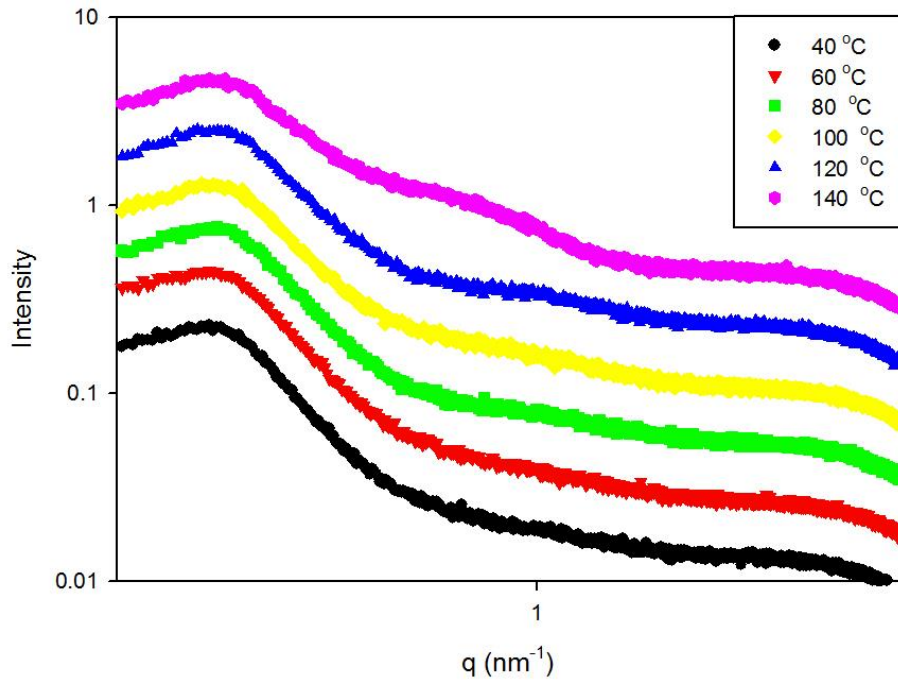


Figure 6.13. SAXS data of 70/30 blends annealed under different temperatures

Moreover, the effects of relative humidity on the properties of the blends were examined. Figure 6.14 presents the data obtained from GM[®] which show the Δ RH effect on RH cycling lifetimes on 70/30 blend. It was clearly observed an extension of lifetime when lower end RH was increased from 10% to 30%, and limited extension when the lower end RH was increased to 50%. In order to examine RH effect on the blends, SAXS experiments were also performed on the 70/30 blends under different RH and the data are shown in Figure 6.15. It is observed that the position of the phase separation peak slightly shifts to lower q values as RH is increased, indicating a slight increase in the distances between the hydrophilic domains, while the peak positions of the crystalline peak and ionic peak were hardly identified due to the loss in scattering contrast with increasing water content. However, there still needs further studies on the effect of RH on the morphology and mechanical properties of the 70/30 blend.

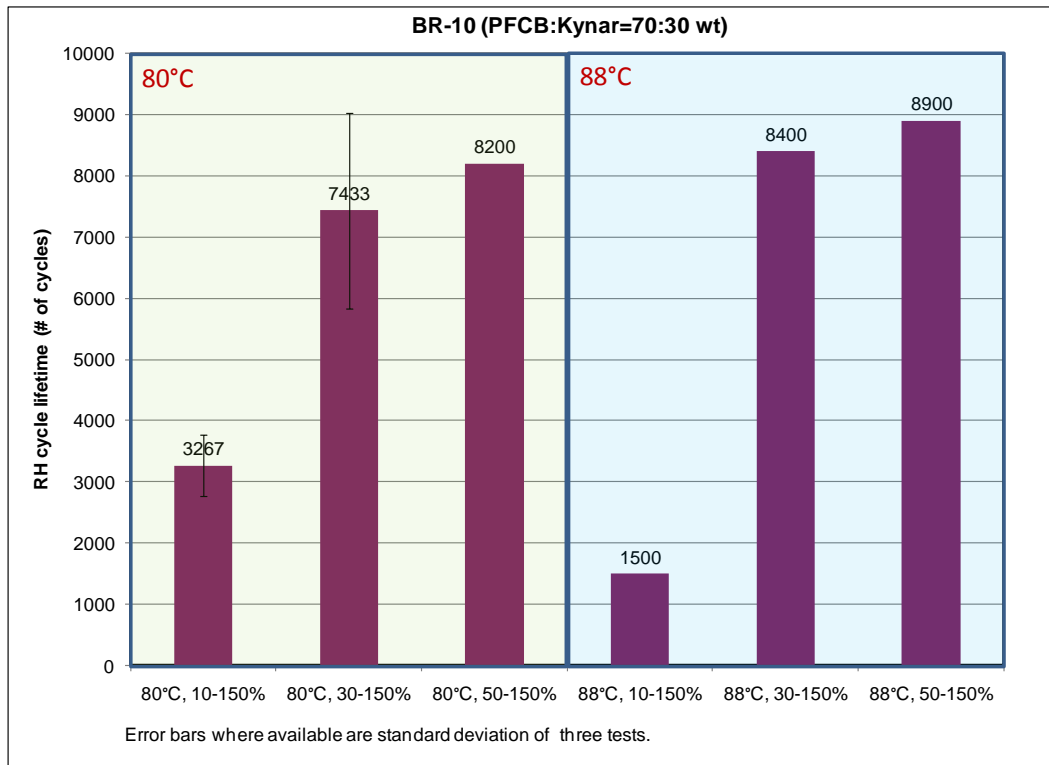


Figure 6.14. Δ RH Effect on RH Cycling Lifetimes:BR-10, 70/30 blends, and data were collected by R. Li at GM[®]

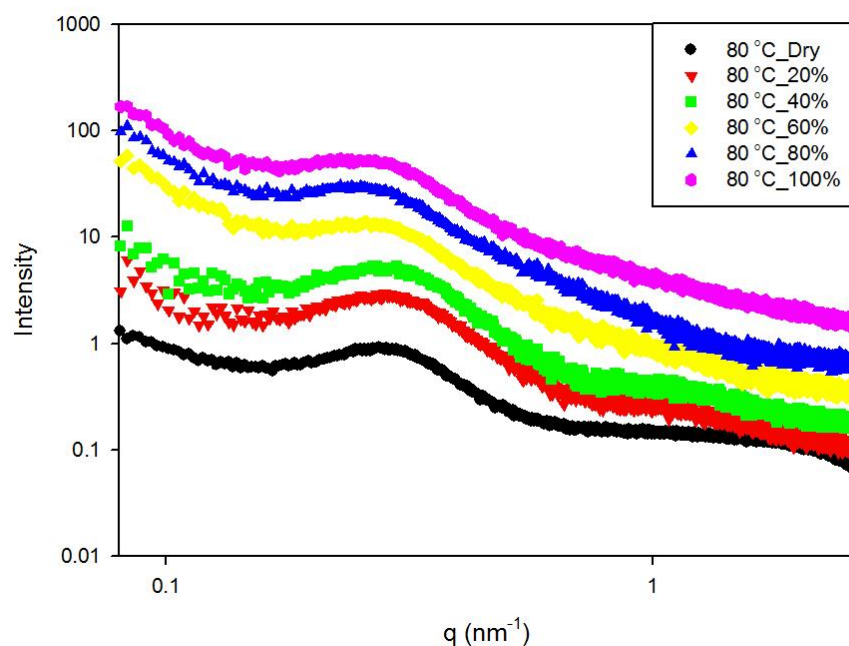


Figure 6.15. SAXS data of 70/30 blends under different RH

6.4 Conclusion

In this work, we presented a detailed morphological study on a newly synthesized sulfonated block copolymer for fuel cell applications by GM[®]. This new PFCB ionomer shows a clear phase-separated morphology, with ionic aggregates in the hydrophilic domains. Furthermore, the correlation between morphology and transport properties were investigated, and it demonstrates morphology is a key factor in determining proton conductivity of the blend. Finally, it was determined that 70/30 PFCB/KF blend would achieve good transport properties as well as enhanced mechanical properties due to the existence of fair amount of KF. Further studies will focus on continuing to reveal the effects of morphology changes under different conditions (annealing temperatures, RH) on the fuel cell performance.

6.5 Acknowledgement

The authors gratefully acknowledge the financial support from GM[®] and Insitute for Critical Technology and Applied Science (ICTAS) at Virginia Tech. The authors thank Dr. Jan Ilavsky for providing standard glassy carbon to obtain absolute intensity. The authors also want to thank Dr. Yeh-Hung Lai from GM[®] for his help and advice during this work, R. Jiang from GM[®] for the conductivity measurement, R. Li, L. Zou and T. Fuller for the RH cycling lifetime measurements, and Nathan May for the AFM measurements. This material is partially based upon work supported by the National Science Foundation under Grant No. DMR-0923107.

6.6 References

- (1) Hickner, M. A.; Ghassemi, H.; Kim, Y. S.; Einsla, B. R.; McGrath, J. E. *Chemical Reviews* **2004**, *104*, 4587.
- (2) Peighambardoust, S. J.; Rowshanzamir, S.; Amjadi, M. *Int J Hydrogen Energ* **2010**, *35*, 9349.
- (3) Mauritz, K. A.; Moore, R. B. *Chemical Reviews* **2004**, *104*, 4535.
- (4) Sumner, J. J.; Creager, S. E.; Ma, J. J.; DesMarteau, D. D. *Journal of The Electrochemical Society* **1998**, *145*, 107.
- (5) Slade, S.; Campbell, S. A.; Ralph, T. R.; Walsh, F. C. *Journal of The Electrochemical Society* **2002**, *149*, A1556.
- (6) Borup, R.; Meyers, J.; Pivovar, B.; Kim, Y. S.; Mukundan, R.; Garland, N.; Myers, D.; Wilson, M.; Garzon, F.; Wood, D. *Chemical Reviews* **2007**, *107*, 3904.
- (7) Rikukawa, M.; Sanui, K. *Progress in Polymer Science* **2000**, *25*, 1463.

- (8) Souzy, R.; Ameduri, B. *Progress in Polymer Science* **2005**, *30*, 644.
- (9) Ruzette, A.-V.; Leibler, L. *Nat Mater* **2005**, *4*, 19.
- (10) Harrison, W. L.; Hickner, M. A.; Kim, Y. S.; McGrath, J. E. *Fuel Cells* **2005**, *5*, 201.
- (11) Kerres, J.; Ullrich, A.; Meier, F.; Häring, T. *Solid State Ionics* **1999**, *125*, 243.
- (12) Cui, W.; Kerres, J.; Eigenberger, G. *Separation and Purification Technology* **1998**, *14*, 145.
- (13) Deimede, V.; Voyiatzis, G. A.; Kallitsis, J. K.; Qingfeng, L.; Bjerrum, N. *J. Macromolecules* **2000**, *33*, 7609.
- (14) Jung, B.; Kim, B.; Yang, J. M. *Journal of Membrane Science* **2004**, *245*, 61.
- (15) Fan, L.; Degen, M.; bendle, S.; Grupido, N.; Ilavsky, J. *Journal of Physics: Conference Series* **2010**, *247*, 012005.
- (16) Hamley, I. W. *The physics of block copolymers*; Oxford University Press; Oxford; New York, 1998.
- (17) Li, X.; Zhang, G.; Xu, D.; Zhao, C.; Na, H. *Journal of Power Sources* **2007**, *165*, 701.
- (18) Fan, Y.; Cornelius, C. J.; Lee, H.-S.; McGrath, J. E.; Zhang, M.; Moore, R.; Staiger, C. L. *Journal of Membrane Science* **2013**, *430*, 106.
- (19) Roche, E. J.; Pineri, M.; Duplessix, R.; Levelut, A. M. *Journal of Polymer Science: Polymer Physics Edition* **1981**, *19*, 1.
- (20) A. Eisenberg, B. H., and R. B. Moore *Macromolecules* **1990**, *23*, 4098.

- (21) Yarusso, D. J.; Cooper, S. L. *Polymer* **1985**, *26*, 371.
- (22) Fan, Y.; Zhang, M.; Moore, R. B.; Lee, H.-S.; McGrath, J. E.; Cornelius, C. J. *Polymer* **2011**, *52*, 3963.
- (23) Shin, D. W.; Lee, S. Y.; Lee, C. H.; Lee, K.-S.; Park, C. H.; McGrath, J. E.; Zhang, M.; Moore, R. B.; Lingwood, M. D.; Madsen, L. A. *Macromolecules* **2013**, *46*, 7797.
- (24) Chen, Y.; Rowlett, J. R.; Lee, C. H.; Lane, O. R.; VanHouten, D. J.; Zhang, M.; Moore, R. B.; McGrath, J. E. *Journal of Polymer Science Part A: Polymer Chemistry* **2013**, *51*, 2301.
- (25) May, N., Virginia Tech, 2011.
- (26) Bae, B.; Yoda, T.; Miyatake, K.; Uchida, H.; Watanabe, M. *Angewandte Chemie* **2010**, *122*, 327.
- (27) Morris, D. R.; Sun, X. *Journal of Applied Polymer Science* **1993**, *50*, 1445.

Chapter 7

Measurement of Persistence Length using Small Angle X-ray Scattering¹

7.1 Introduction

Persistence length, l_p , is defined as the length over which correlations in the direction of the tangent are lost. In terms of bond angle θ between a vector that is tangent to the polymer at position 0 and a tangent vector at a distance s away from position 0, we can express persistence length as,^{2,3}

$$\langle \cos \theta \rangle = \exp(-s/l_p) \quad (7.1)$$

where $\langle \cos \theta \rangle$ is the expected value of the cosine of the angle, and it falls off exponentially with distance. For small values of bond angle ($\theta \ll 1$),

$$\cos \theta \cong 1 - \frac{\theta^2}{2} \quad (7.2)$$

and

$$\ln(\cos \theta) \cong -\frac{\theta^2}{2} \quad (7.3)$$

Thus one can express the persistence length as

$$l_p = s \frac{2}{\theta^2} \quad (7.4)$$

SAXS has been widely used to study the persistence length of various polymers.⁴⁻²¹ One early method to calculate persistence length from scattering curve was proposed by Kratky and Porod.²² If intensity is plotted as a function of scattering vector q , it can be observed that the scattering curve has several different regions. At low q region, the polymer chain can be considered as an individual particle, and the scattering on this polymer chain follows Guinier law²³ as

$$I(q) = \rho_0^2 v^2 \exp\left(-\frac{1}{3} q^2 R_g^2\right) \quad (7.5)$$

where R_g is the radius of gyration, indicating the size of the particle.

With increasing q values, the size that SAXS can probe decreases, and the scattering curve starts to characterize the random coil nature of the polymer. Followed by Debye' equation,²⁴ scattered intensity for random coils will be inversely proportional to q^2 . As q continues to increase, the scattering curve reaches the region that indicates the rigidity of the polymer chain, and now the polymer chain could be viewed as a rigid rod. Thus, scattered intensity will be inversely proportional to q .²² Figure 7.1 illustrates this characteristics of scattering intensity with respect to different q regions.

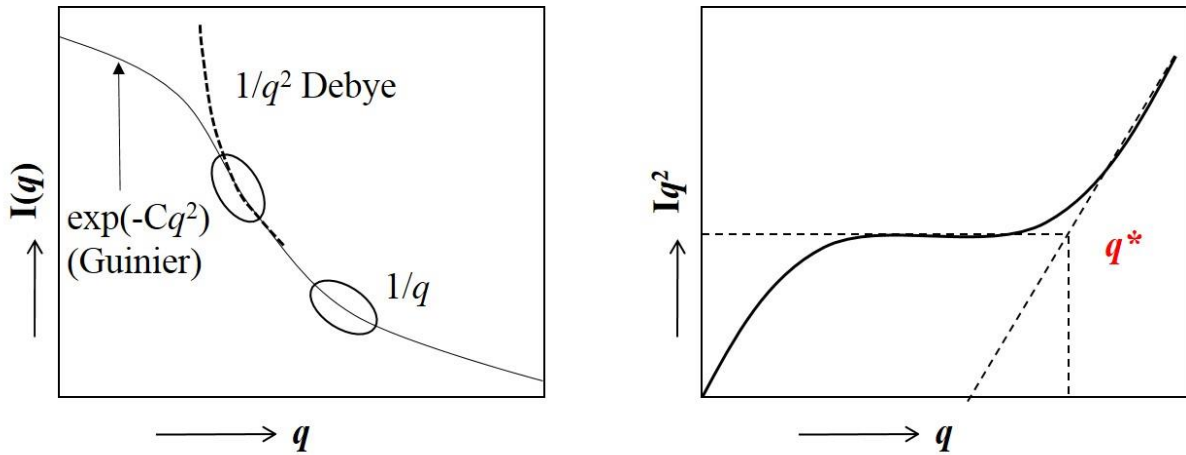


Figure 7.1. Schematic drawing of the scattering curve in different q regions

The right plot in Figure 7.1 is usually called Kratky-Porod plot, from which the persistence length can be calculated as

$$l_p = \frac{a}{q^*} \quad (7.6)$$

where a is constant given as^{4,25}

$$a = \frac{6}{\pi} \quad (7.7)$$

Many other researchers have worked on obtaining a more accurate a value in Eqn. 7.6. Peterlin⁵ performed calculation for assuming a chain with N links of fixed length that are all joined at a fixed angle by the use of Monte Carlo simulation, and obtained that

$$a \cong 2 \quad (7.8)$$

A further refinement of Peterlin's method performed by Heine and co-workers²⁶ shown that $a \cong 2.3$ by calculating two link-chains with fixed angles $\cos\alpha=0.8$, and $\cos\alpha=0.9$, respectively.

A later calculation by Burchard and Kajiwara⁸ considered both the bond angle and internal rotation angle, and they determined the transition position by extrapolating the coil region and rigid region, which gives

$$a = 2.87 \pm 0.05 \quad (7.9)$$

However, still there has not been an agreement on the value of a , but common choice of the value of a is between 2 and 3.

Beside the Kratky-Porod plot method, some other methods that consider the whole scattering curve have also been developed. If excluded volume is assumed to be zero, Sharp and Bloomfield⁶ showed that the form factor can be written as

$$F(x) = G_2 \left\{ \left(\frac{2}{x^2} \right) (e^{-x} - 1 + x) + \frac{2l_p}{15L} \left[4 + \frac{7}{x} - \left(11 + \frac{7}{x} \right) e^{-x} \right] \right\} \quad (7.10)$$

where G_2 is the Guinier or Debye prefactor, and can be calculated for isolated chains using

$$G_2 = V_{chain} \rho_{chain}^2 \quad (7.11)$$

where V_{chain} is the number of chains per scattering volume in a dilute solution, and ρ_{chain} is the scattering contrast between the solute and solvent, and

$$x = \frac{Ll_p q^2}{3} \quad (7.12)$$

and L is defined as the contour length, which can be written as

$$L = 2l_p n_k \quad (7.13)$$

where n_k is the number of Kuhn segments.

However, Eqn. 7.10 is only valid for rather long polymer chain and small q values, i.e. $ql_p < 2$. For large q values, Cloizeaux¹⁰ showed that the form factor can be written as

$$F(q) = \frac{\pi}{ql_p} + \frac{2}{3q^2l_p^2} \quad (7.14)$$

Later on, Beaucage and co-workers¹⁷ proposed a unified function to model the two structural levels of a Kratky-Porod persistent chain, and it is given by

$$I(q) = G_2 \exp(-q^2 R_{g2}^2 / 3) + B_2 \exp(-q^2 l_p^2 / 3) (q_2^*)^2 + G_1 \exp(-q^2 R_{g1}^2 / 3) + B_1 (q_1^*)^{-1} \quad (7.15)$$

where

$$q_i^* = \left[\frac{q}{\left(\operatorname{erf} \left(qkR_g / \sqrt{6} \right) \right)^3} \right] \quad (7.16)$$

$$R_{g2} = \sqrt{\frac{n_k (2l_p)^2}{6}} \quad (7.14)$$

$$B_2 = \frac{2G_2}{R_{g2}^2} \quad (7.15)$$

$$R_{g1} = \frac{l_p}{\sqrt{3}} \quad (7.16)$$

$$B_1 = \frac{\pi G_1}{2l_p} = \frac{\pi G_2}{n_k 2l_p} \quad (7.17)$$

In Eqn. 7.14, 1 and 2 indicate the two different regions, with 1 as the Gaussian random coil region, and 2 as the rigid rod region, respectively. G_2 is the Gaussian prefactor for Debye-Gaussian regime, and R_{g2} is defined as the radius of gyration for the coil structure. G_1 is the Gaussian prefactor for the rod-like regime, and R_{g1} is defined as the radius of gyration of an infinitely thin rod with length $l_k=2l_p$. Thus the whole scattering curve including the transition between Gaussian random coil structure and rigid rod structure can be studied using this unified function.

In this work, first we would like to continue the discussion of calculation of the form factor using SAXS as discussed in Chapter 1, and examined the size of mono-dispersed gold nanoparticles in water. Then different methods to calculate persistence length using SAXS data were performed on four different stilbene and styrenic polymers, and the results obtained from SAXS measurements were compared with those from Size Exclusion Chromatography (SEC). This work was able to validate the steric crowing effect and quantify the stiffness of chains in these polymers.

7.2 Experimental Section

7.2.1 Materials

Gold colloid (~0.01wt%), a stabilized suspension of mono-dispersed spherical gold nanoparticles with a radius of 5.4 nm dissolved in water, was purchased from Sigma-Aldrich.

Four different stilbene and styrenic containing copolymers shown in Figure 7.2 were synthesized by Dr. Y. Li from Prof. S. R. Turner's research group, and the molecular weight of these four polymers are listed in Table 7.1.

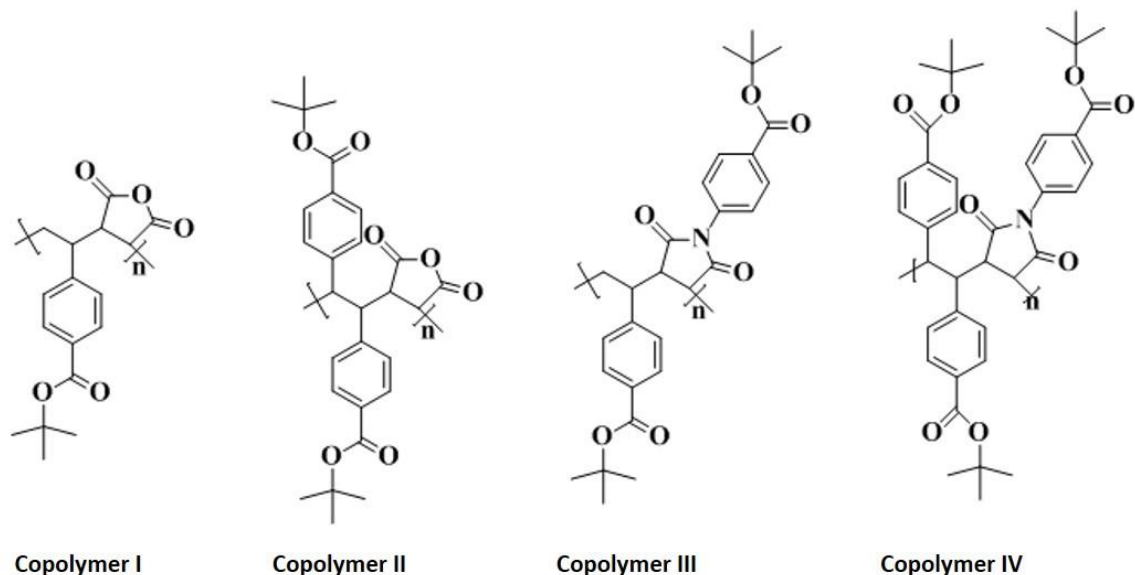


Figure 7.2. Chemical structure of copolymer I, II, III, IV, all copolymers were synthesized by Dr. Li from Prof. Turner's research group (Reprinted with permission from *Macromolecules* 2012, 45, 1595. Copyright, The American Chemistry Society, 2012)

Table 7.1. Molecular characteristics of copolymer I, II, III, IV (Reprinted with permission from *Macromolecules* 2012, 45, 1595. Copyright, The American Chemistry Society, 2012)

	M_n (g/mol) ^c	M_w (g/mol) ^d
Copolymer I ^a	41100	64600
Copolymer II ^a	73000	163000
Copolymer III ^b	60300	154000
Copolymer IV ^b	97200	225000

SEC in DMF containing 0.1 M lithium nitrate and 1% formic acid; ^bSEC in THF; ^cViscometry detection/Universal Calibration; ^dLight scattering detection

7.2.2 Small Angle X-ray Scattering

SAXS experiments were performed using a Rigaku S-Max 3000 3 pinhole SAXS system, equipped with a copper rotating anode emitting X-ray with a wavelength of 0.154 nm (Cu K α). Two-dimensional SAXS patterns were obtained using a fully integrated 2D multiwire, proportional counting, gas-filled detector, with an exposure time of 1 hour. All SAXS data were analyzed using the SAXSGUI software package to obtain radically integrated SAXS intensity versus scattering vector q (SAXS), where $q=(4\pi/\lambda)\sin(\theta)$, θ is

one half of the scattering angle and λ is the wavelength of X-ray. For all scattering experiments, the sample-to-detector distance was 1603 mm, and the q -range was calibrated using a silver behenate standard. Solution samples were measured in a glass capillary with a diameter of 1.5 mm and wall thickness of 0.01 mm. The measured intensity had been corrected for sample transmission, solvent scattering and background scattering.

7.3 Results and Discussion

7.3.1 Form Factor of Spheres

As shown in pervious section, the scattered intensities for a dilute system with spherical particles can be written as Eqn. 1.24. From that equation, it should be noticed that at very low q values the scattered intensity is flat, i.e. $I \sim q^0$. As q is increased, oscillation coming from the sine and cosine functions can be observed. Using the position of the first minimum in the intensity vs. q scattering curve, the radius of the particles can be calculated as

$$R = \frac{4.493}{q_{1st \text{ minimum}}} \quad (7.18)$$

In Figure 7.3, the black curve is the theoretical curve with $R=5.4$ nm, and the red curve is the experimental curve. It can be observed that experimental curve is very close to the theoretical curve, and R can be calculated using Eqn. 7.18 from the first minimum position to be very close to 5.4 nm.

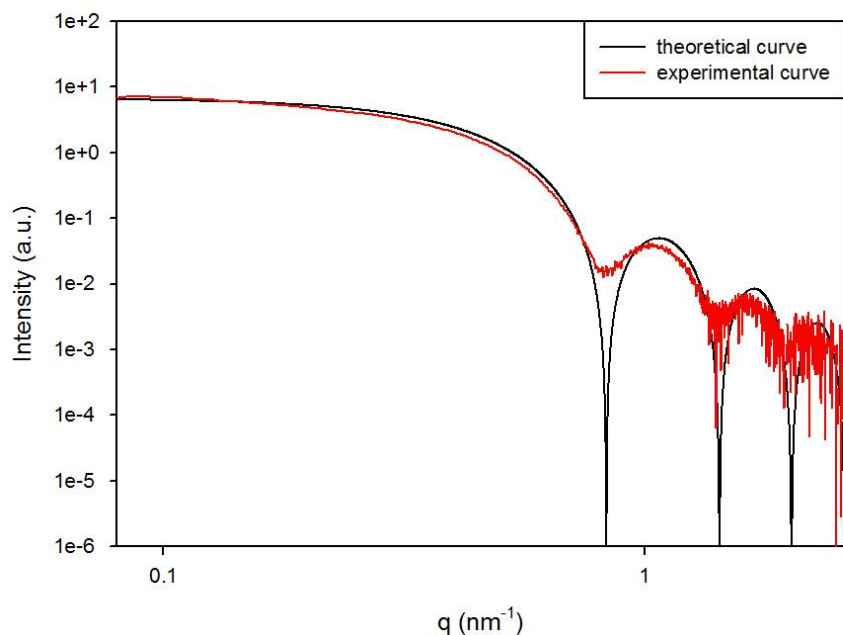


Figure 7.3. Theoretical and experimental SAXS curves of gold colloid

7.3.2 Study of Persistence Length using SAXS

As introduced in the previous section, several methods could be applied to calculate persistence length of polymers. This study was not aiming at comparing the results from different methods, but emphasizing how steric crowding effect affects the stiffness of these stilbene and styrenic containing polymers.

First, the Kratky-Porod plot method was applied to calculate the persistence length. Though choice of the a value in Kratky-Porod plot is still under debate, the value of $a=2.3$ was used as Heine and co-workers²⁶ suggested for determination of persistence length. SAXS data were plotted as log of intensity versus log of scattering vector q in order to clearly show the transition from the random coil nature of the polymer to the rod-like behavior of the polymer. The position where slopes change from -2 to -1 would be used as

the position of q^* as shown in Eqn. 7.6. However, one issue with the Kratky-Porod plot is that the -2 slope that indicates rod-like behavior of the polymer cannot always be clearly observed, instead a -1.5 to -2.0 slope would be normally observed.^{14,17,19,21,22,27,28} In this case, many researchers^{14,17,19,21,27,28} suggested to use the position where the slope of scattering curve changes significantly as the q^* position to calculate l_p . Thus, this method is applied in this work to calculate the persistence length of stilbene and styrenic containing copolymers. The log-log of $I(q)$ - q plots of different polymers are shown in Figure 7.4. Due to the finite length of these samples, it was expected that an exact -2 slope corresponding to the random coil structure could not be clearly observed. On the other hand, the exact -1 slope can be clearly observed from SAXS measurements for all polymers I, II, III, IV. Furthermore, clear changes in the slopes of scattering curves could be identified for all these polymers, which could be utilized to calculate persistence length. In order to keep consistent calculations to find the q^* positions of these polymers, common ranges of data both in low q range (0.030-0.052 \AA^{-1}) and high q range (0.075-0.2 \AA^{-1}) were selected to determine the two different slope regions, and thus the q^* position. This allows one to use Eqn. 7.6 to calculate persistence length and the results are shown in Table 7.2.

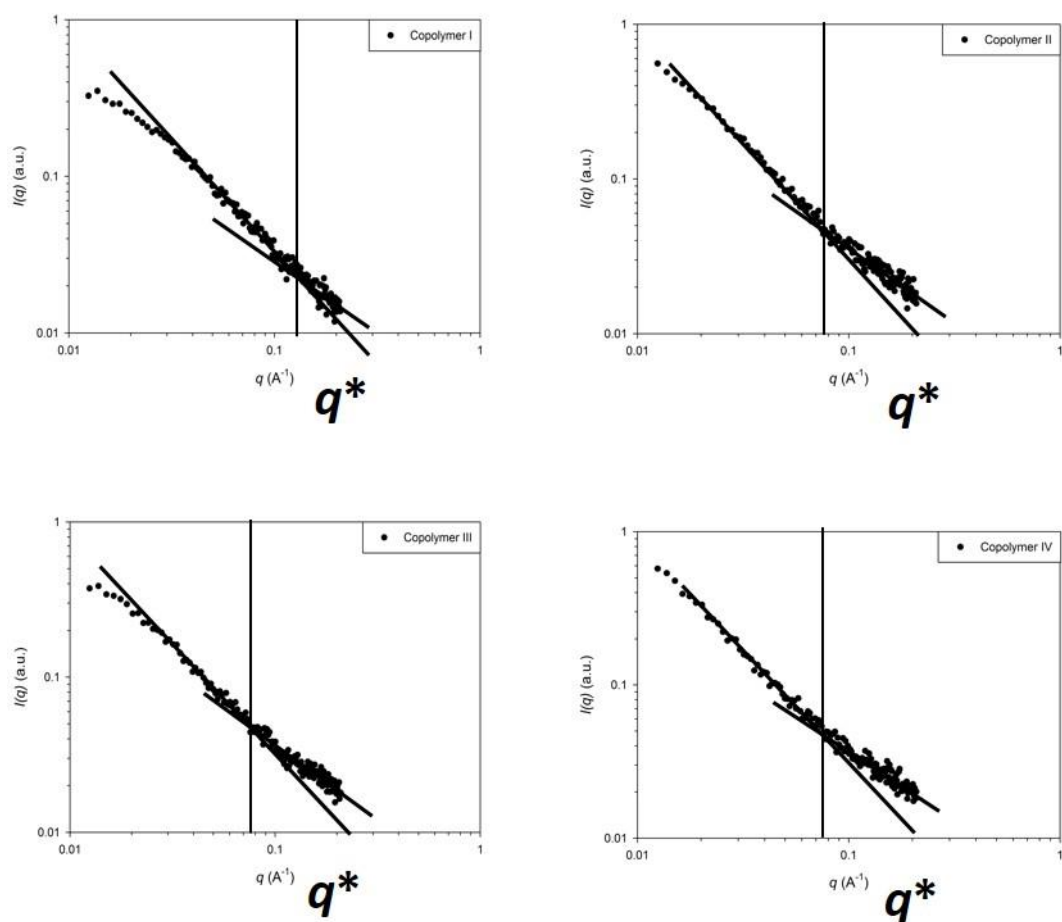


Figure 7.4. Log-log of $I(q)$ vs. q plots for copolymers I, II, III, IV. The fit range includes all of the data points. Every fifth data point is selected to plot for clarity (Reprinted with permission from *Macromolecules* 2012, 45, 1595. Copyright, The American Chemistry Society, 2012)

Table 7.2. Fitting results from SAXS measurements for copolymers I, II, III, IV (Reprinted with permission from *Macromolecules* 2012, 45, 1595. Copyright, The American Chemistry Society, 2012)

	q^* (\AA^{-1})	l_p by Eq. (1) (nm)
Copolymer I	0.139	1.7
Copolymer II	0.079	2.9
Copolymer III	0.076	3.0
Copolymer IV	0.075	3.1

From Table 7.2 it can be clearly seen that copolymer II has a much larger persistence length than that of copolymer I, which indicates that it has a much stiffer polymer chain compared with that of copolymer I. On the other hand, there is not a significant difference in the persistence length between copolymer III and IV. This is probably due to the fact that the scattering curves of these two polymers both exhibit a gradual transition between the two regions, and this leads to very close values of q^* positions. This is also known as a major drawback of Kratky-Porod plot method in that the determination of q^* positions, and thus persistence length, are subject to some ambiguities by using Kratky-Porod plot method.³¹

To improve the accuracy of calculating persistence length, Sharp and Bloomfield function (SBF) given in Eqn. 7.10 was applied on the data in the entire q range. The utilization of the whole scattering data would potentially lead to better and accurate values of persistence length. Since the scattering intensities are in arbitrary unit, the values of the prefactor G_2 from SBF method would not give much information and they are treated as undefined fitting constants, and not reported here. The fitting curves are shown in Figure 7.5, and the results of fitting variables N_k , l_p , as well as the fitting confidence intervals (95%0 for l_p , are listed in Table 7.3.

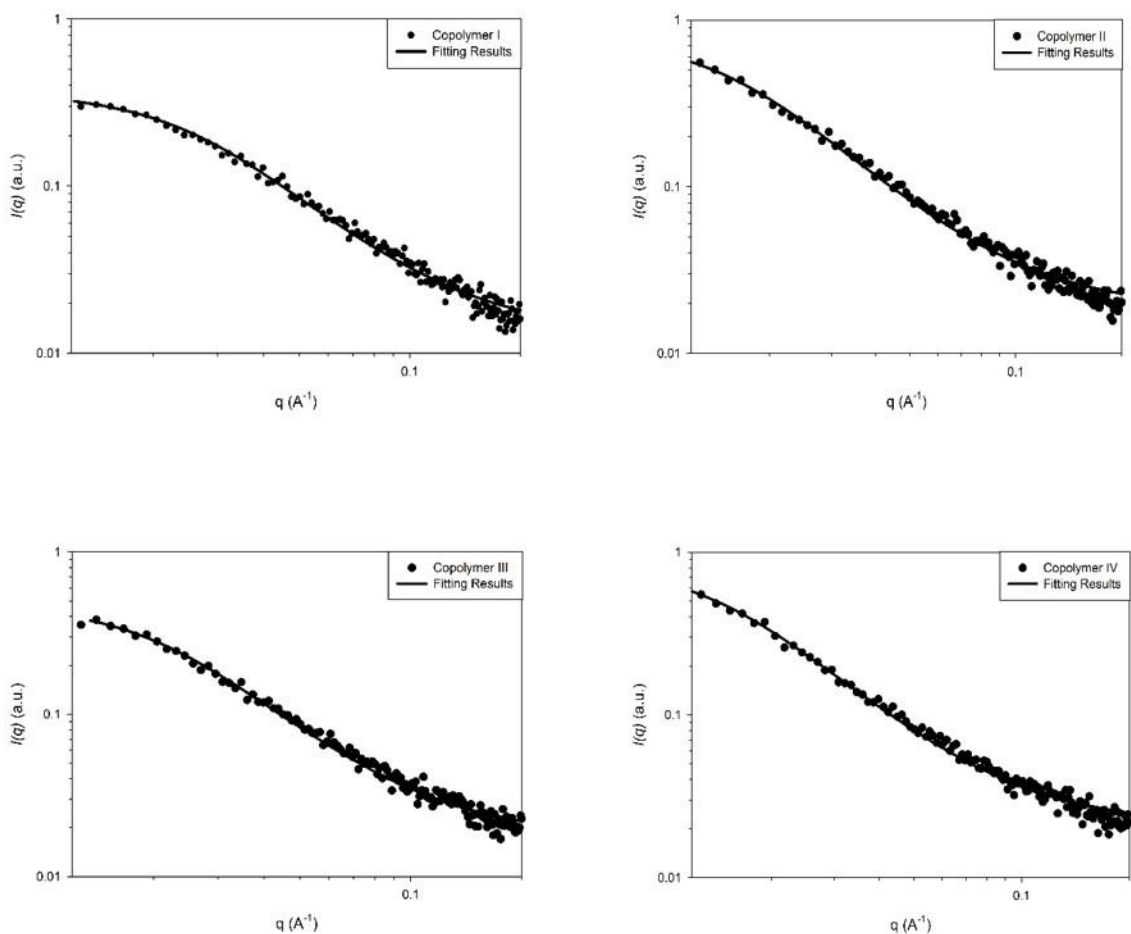


Figure 7.5. Sharp and Bloomfield function (SBF) fits to the data of Figure 6.5. The fit range includes all of the data points. Every fifth data point is selected to plot for clarity (Reprinted with permission from *Macromolecules* 2012, 45, 1595. Copyright, The American Chemistry Society, 2012)

Table 7.3. Parameters of SBF for copolymer I, II, III, IV (Reprinted with permission from *Macromolecules* 2012, 45, 1595. Copyright, The American Chemistry Society, 2012)

	N_k	l_p (nm)	Confidence Interval (95%) (nm)
Copolymer I	7.62	2.7	(2.62, 2.78)
Copolymer II	11.7	3.6	(3.54, 3.66)
Copolymer III	7.53	3.4	(3.32, 3.48)
Copolymer IV	11.2	4.0	(3.93, 4.07)

The results obtained from SBF methods clearly show copolymer III has a much larger persistence length than that of copolymer I, while copolymer IV has a much larger persistence length than that of copolymer II. This demonstrates that adding more bulky phenyl rings along the polymer chains would lead to much stiffer polymer chains, thus result in an increase in the values of persistence length. However, it needs to point out that the values of persistence length obtained from Kratky-Porod plot are different from those obtained using SBF method. This may due to the error in finding the accurate position of q^* given that only gradual change in slopes of the scattering curves are observed. In spite of that, an increase in the values of persistence length from copolymer I to copolymer II, and from copolymer III to copolymer IV, respectively, is clearly observed. This clearly demonstrates that the stilbene containing alternating copolymers (III and IV) have larger persistence length than the analogous styrene containing alternating copolymers (I and II) in that their polymer chains are more rigid due to the steric conformational constraints, which lead to larger chain stiffness of the stilbene containing alternating copolymers.

SEC will also provide a complementary method for quantifying the stiffness of copolymer chains. The persistence length results obtained from SEC were calculated by Dr. Y. Li from Prof. S. R. Turner's group. The l_p for copolymer I, II, II, and IV are 2.7, 3.6, 3.4, and 4.0 nm, respectively, and these results showed similar trends as those obtained from SBF. Results from both SAXS and SEC showed that the added phenyl groups increase the rigidity of the polymer chains by about 30-50%. These persistence length values put these copolymers into a broadly defined "semi-rigid" category of polymers.

7.4 Conclusion

SAXS is a powerful technique in that it could be utilized to study various physical parameters of polymers. Modeling of SAXS data would allow one to obtain the information such as shape, size of polymer in dilute solution. Furthermore, SAXS could also be performed to study the chain stiffness of various polymers in dilute solution. In our results, stilbene and styrenic alternating copolymers were calculated to have persistence lengths ranging from 2 to 6 nm, which characterizes these copolymers into a class of semi-rigid polymers. It is also demonstrated that steric crowding effect would strongly affect the persistence lengths of similar polymers. Addition of the second phenyl ring on the backbone of stilbene and styrenic alternating copolymers would enhance the polymer chain stiffness by about 30-50%. It was also found the polymer backbones enchainned with *t*-butyl carboxylate functionalized *N*-phenyl maleimide units have larger persistence length than those containing maleic anhydride units. This is probably due to the steric hindrance caused by the bulky *t*-butyl phenyl carboxylate functional group that is located on the maleimide unit.

7.5 Acknowledgements

We wish to express our gratitude to Dr. Y. Li from Professor S. R. Turner's research group for synthesizing all the copolymers, and Professor R. D. Gandour for his assistance in using energy minimization in ChemBio3D Ultra and to Graduate Student G. Divoux for his assistance and helpful discussions on SAXS measurements. This work was supported by the donors of the American Chemical Society Petroleum Research Fund, the National

Science Foundation under Grant No. DMR-0905231 and the National Science Foundation under Grant No. DMR-0923107.

7.6 References

- (1) Li, Y.; Zhang, M.; Mao, M.; Turner, S. R.; Moore, R. B.; Mourey, T. H.; Slater, L. A.; Hauenstein, J. R. *Macromolecules* **2012**, *45*, 1595.
- (2) Doi, M.; Edwards, S. F. *The theory of polymer dynamics*; Clarendon Press; Oxford University Press: Oxford Oxfordshire, New York, 1986.
- (3) Rubinstein, M.; Colby, R. H. *Polymer physics*; Oxford University Press: Oxford ; New York, 2003.
- (4) Porod, G. *Journal of Polymer Science* **1953**, *10*, 157.
- (5) Peterlin, A. *Journal of Polymer Science* **1960**, *47*, 403.
- (6) Sharp, P.; Bloomfield, V. A. *Biopolymers* **1968**, *6*, 1201.
- (7) Stivala, S. S.; Herbst, M.; Kratky, O.; Pilz, I. *Archives of Biochemistry and Biophysics* **1968**, *127*, 795.
- (8) Burchard, W.; Kajiwara, K. *Proceedings of the Royal Society of London. A. Mathematical and Physical Sciences* **1970**, *316*, 185.
- (9) Schmid, C. W.; Rinehart, F. P.; Hearst, J. E. *Biopolymers* **1971**, *10*, 883.
- (10) des Cloizeaux, J. *Macromolecules* **1973**, *6*, 403.
- (11) Pineri, M.; Meyer, C.; Levelut, A. M.; Lambert, M. *Journal of Polymer Science: Polymer Physics Edition* **1974**, *12*, 115.
- (12) Yoon, D. Y.; Flory, P. J. *Polymer* **1975**, *16*, 645.
- (13) Yoon, D. Y.; Flory, P. J. *Macromolecules* **1976**, *9*, 294.
- (14) Cleland, R. L. *Archives of Biochemistry and Biophysics* **1977**, *180*, 57.

- (15) Kube, O.; Springer, J. *Journal of Applied Crystallography* **1987**, *20*, 41.
- (16) Rawiso, M.; Duplessix, R.; Picot, C. *Macromolecules* **1987**, *20*, 630.
- (17) Beaucage, G.; Rane, S.; Sukumaran, S.; Satkowski, M. M.; Schechtman, L. A.; Doi, Y. *Macromolecules* **1997**, *30*, 4158.
- (18) Tinland, B.; Pluen, A.; Sturm, J.; Weill, G. *Macromolecules* **1997**, *30*, 5763.
- (19) Yamazaki, S.; Muroga, Y.; Noda, I. *Langmuir* **1999**, *15*, 4147.
- (20) Taylor, T. J.; Stivala, S. S. *Journal of Polymer Science Part B: Polymer Physics* **2003**, *41*, 1263.
- (21) Muroga, Y.; Noda, I.; Nagasawa, M. *Macromolecules* **1985**, *18*, 1576.
- (22) Glatter, O.; Kratky, O. *Small angle x-ray scattering*; Academic Press, 1982.
- (23) Guinier, A.; Fournet, G. *Small-Angle Scattering of X-rays*; John Wiley & Sons, Inc. Chapman & Hall, Ltd. : New York, London, 1955.
- (24) Debye, P. *The Journal of Physical and Colloid Chemistry* **1947**, *51*, 18.
- (25) Kratky, O. *Kolloid-Z.u.Z.Polymere* **1962**, *182*, 7.
- (26) Heine, V. S.; Kratky, O.; Roppert, J. *Die Makromolekulare Chemie* **1962**, *56*, 150.
- (27) Gupta, A. K.; Cotton, J. P.; Marchal, E.; Burchard, W.; Benoit, H. *Polymer* **1976**, *17*, 363.
- (28) Choudhury, P. K.; Bagchi, D.; Menon, R. *Journal of Physics: Condensed Matter* **2009**, *21*, 195801.

Chapter 8

Morphological Characterization of Block Copolymers using Small Angle X-ray Scattering

8.1 Background

8.1.1 Introduction

Block copolymers belong to a particular class of polymers that are formed by two or more chemically homogenous blocks of polymers that are joined by covalent bonds.¹ Based on their architectures, block copolymer can be divided into diblock, triblock, multiblock, random multiblock, starblock, and graft copolymers, and their architectures are shown in Figure 8.1.

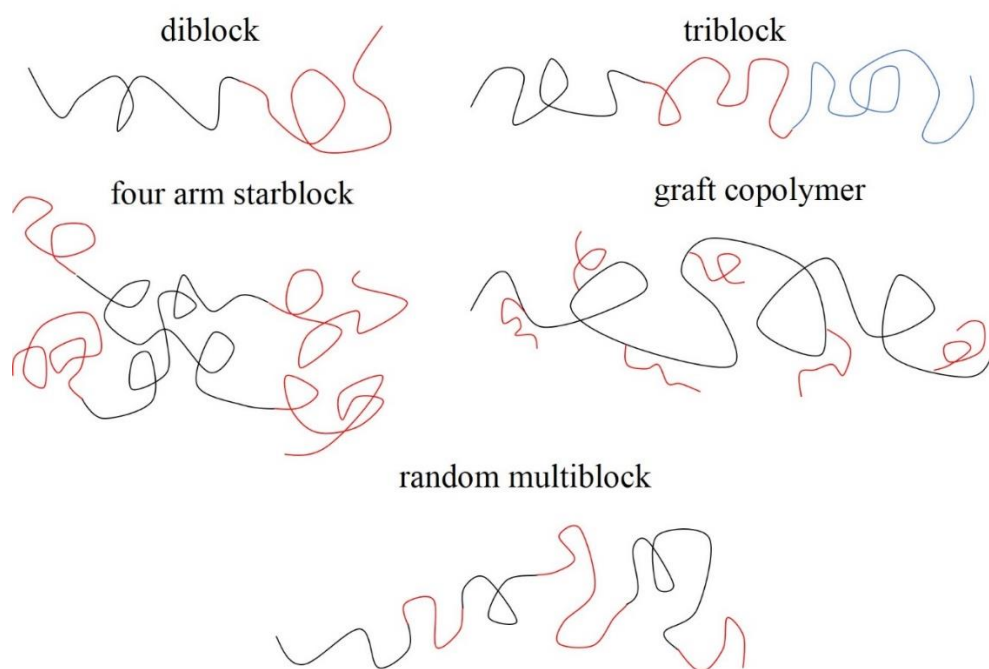


Figure 8.1. Some architectures of block copolymers

Block copolymers are widely used in industry, and applications of block copolymers can be found in the book edited Goodman,² book edited by Lazzari and coworkers,³ review

written by Jun and coworkers.⁴ While in this chapter, we will focus on introducing SAXS as a means to study the bulk morphology of block copolymers.

8.1.2 Microphase Separation in Block Copolymer

Amorphous diblock copolymers are the simplest type of block copolymer to be studied with. The microphase separation in diblock copolymers depends on the volume fractions of the two different blocks (f_A, f_B , where $f_A + f_B = 1$), the Flory-Huggins χ parameter between the two blocks, and also the total degree of polymerization, N .⁵ The degree of segregation in block copolymers are controlled by χN , which will divide degree of segregation into weak segregation limit (WSL), intermediate segregation region (ISR), and strong segregation limit (SSL). For $0 < \chi N < 10$, it is classified as WSL; for $10 < \chi N < 50$, it is classified as ISR; and if $\chi N \rightarrow \infty$, it is classified as SSL.

An example of the experimental determined phase separation diagram for polyisoprene-polystyrene (PI-PS) diblock copolymer is shown in Figure 8.2.⁶ It is observed that as $f_{PI} \rightarrow \infty$ or $f_{PI} \rightarrow 0$, a disordered phase results. While as $|f_{PI} - 0.5|$ becomes smaller, it undergoes a morphology transition in the SSL. For $f_{PI} < 0.23$, it results in a body centered cubic (BCC) morphology; for $0.23 < f_{PI} < 0.34$, a hexagonal packed cylinders (HEX) morphology results; for $0.34 < f_{PI} < 0.38$, it leads to a bicontinuous cubic ‘gyroid’ morphology; for $0.38 < f_{PI} < 0.66$, it results in a lamella morphology; for $0.66 < f_{PI} < 0.72$, it also leads to a bicontinuous cubic ‘gyroid’ morphology; for $0.72 < f_{PI} < 0.87$, a HEX morphology results; and for $f_{PI} > 0.87$, it results in a BCC morphology.

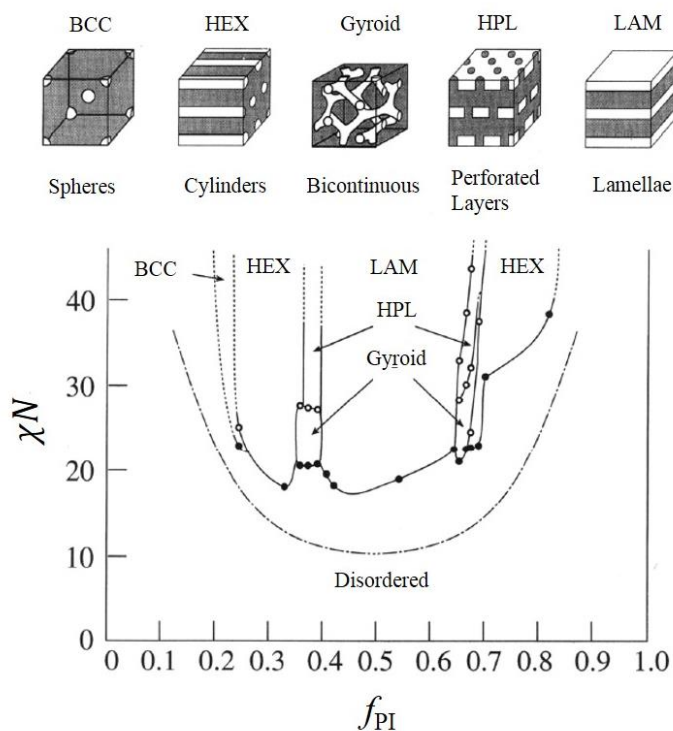


Figure 8.2. χN versus f_{PI} diagram for PI-PS diblock copolymers (Reprinted with permission from *Macromolecules* **1995**, 28, 8796. Copyright, The American Chemical Society, 1995)

Traditional methods to study this morphological change include small-angle X-ray scattering (SAXS), small-angle neutron scattering (SANS), and transmission electron microscopy (TEM). Here SAXS will be introduced as a major means to study different morphology in block copolymers.

8.1.3 SAXS as A Means to Study Microphase Separation in Block Copolymer

8.1.3.1 Invariant for Ideal Two-Phase System

For an ideal two-phase system, the average scattering length density can be calculated as⁷

$$\langle \rho \rangle = \phi_1 \rho_1 + \phi_2 \rho_2 \quad (8.1)$$

where ϕ_1 and ϕ_2 are the volume fractions of the two different phases, 1 and 2, respectively, and $\phi_1 + \phi_2 = 1$; and ρ_1 and ρ_2 are the scattering length densities of the two different phases, 1 and 2, respectively. Then the invariant can be calculated as

$$Q = V \langle \eta^2 \rangle \quad (8.2)$$

where V is the volume, and

$$\langle \eta^2 \rangle = \eta_1^2 \phi_1 + \eta_2^2 \phi_2 \quad (8.3)$$

where

$$\eta_1 = \rho_1 - \langle \rho \rangle \quad (8.4)$$

$$\eta_2 = \rho_2 - \langle \rho \rangle \quad (8.5)$$

Eqn. 8.3 now can be written as

$$Q = V (\Delta\rho)^2 \phi_1 \phi_2 \quad (8.6)$$

if we define

$$\Delta\rho = \rho_1 - \rho_2 = \eta_1 - \eta_2 \quad (8.7)$$

It needs to point out that Eqn. 8.6 is only valid if the two following conditions are satisfied:

- (1) The two phases have a sharp boundary with zero thickness
- (2) Only two phases with constant scattering length densities exist in the system

Eqn. 8.6 can be very useful in that $\Delta\rho$ can be calculated if Q is known from the scattering data. However, since the assumption (2) only exists in theory, we often obtain scattering curves that are deviated from theoretical curves. But we can utilize this deviation to obtain some useful information such as the width of the diffuse phase boundaries.⁷

8.1.3.2 Porod's Law

The Porod's law⁸ describes that the slope of the log-log plot of $I(q)$ vs. q should be -4 for an ideal two-phase system, which represents the strong interface of the scattering objects. Moreover, the scattering intensity is also proportional to the total area of the interface, S , between the two phases, which means we have

$$\lim_{q \rightarrow \infty} I(q) \propto 2\pi (\Delta\rho)^2 S q^{-4} \quad (8.8)$$

Furthermore, Porod also pointed out that the slope of the log-log plot of $I(q)$ vs q represents the fractal dimension of the scattering objects. If the slope equals -2, it indicates the structure of Gaussian chain, and if the slope is -1, it represents rigid rod structure.

8.1.3.3 Miller Indices

In order to introduce SAXS on highly ordered structure, diffraction by ideal crystals needs be briefly introduced here. A crystal is defined as a given atomic pattern that can be repeated in three dimensions.^{9,10} Thus we can describe the crystal by using three vectors, i.e. $(\vec{a}, \vec{b}, \vec{c})$. Now if we have a family of planes, we can thus characterize these planes by using three integers as (h, k, l) , which are known as Miller indices. This allows us to represent the plane in the \vec{a} direction as a/h , \vec{b} direction as b/k , and \vec{c} direction as c/l . By using Miller indices, it also provides us a means to calculate the distance between the planes.

8.1.3.4 Scattering on Ordered Nanostructures

As it has been shown in Chapter 1, the scattering vector in SAXS is defined as

$$q = \frac{4\pi \sin \theta}{\lambda} \quad (8.9)$$

The q value in Eqn. 8.9 can also be considered as a measure of reciprocal spacing. Bragg's law allows one to calculate the distance, d , between the crystallographic planes in the atomic lattice,

$$\sin \theta = \frac{n\lambda}{2d} \quad (8.10)$$

where n is an integer, λ is the wavelength of X-ray incident wave. Combining Eqn. 8.9 and 8.10, one can obtain an equation to estimate the distance between the periodic structures in SAXS by

$$d = \frac{2n\pi}{q} \quad (8.11)$$

For a system that contains a one-dimensional periodic structure, i.e. lamellar structure, as shown in Figure 8.3(a), the position of the scattering peaks can be calculated by the equation

$$q_n = n \frac{2\pi}{d} \quad (8.12)$$

where $n=1, 2, 3$, and d is the lamellar repeat unit. Thus scattering on such a system will give scattering maxima at $q, 2q, 3q, \dots$

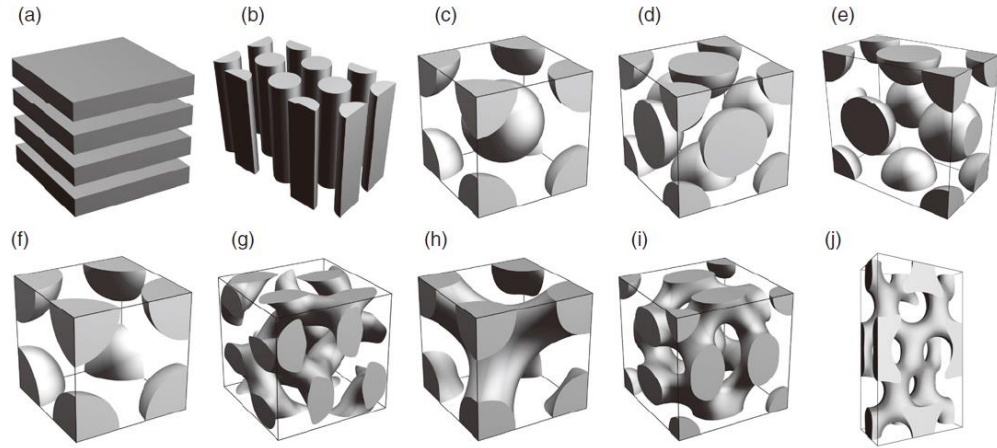


Figure 8.3. Common lattice structure. (a) Lamellae; (b) hexagonal packed cylinders; (c) BCC; (d) FCC; (e) hexagonal close-packed spheres; (f) primitive cubic; (g) double gyroid; (h) double diamond (DD); (i) Pm3n; and (j) Fddd (Reprinted with permission from *Polymer Science: A Comprehensive Reference*; Matyjaszewski, K., Möller, M., Eds.; Elsevier: Amsterdam, 2012, p 363. Copyright, Elsevier, 2012)

For a system that contains hexagonally close-packed cylinders as shown in Figure 8.3(b), the positions of the scattering peaks can be described by the equation¹¹

$$q_n = \frac{4\pi}{\sqrt{3}a} \sqrt{h^2 + k^2 + hk} \quad (8.13)$$

where a is the distance between two neighboring rods, and h, k are the Miller indices. By varying h, k values, one could obtain the peak positions for scattering on such a system as q ($(h,k)=(1,0)$), $\sqrt{3} q$ ($(h,k)=(1,1)$), $2q$ ($(h,k)=(2,0)$), $\sqrt{7} q$ ($(h,k)=(2,1)$), and so on. Thus this leads to peak position ratios of $1 : \sqrt{3} : 2 : \sqrt{7}$.

For a primitive cubic as shown in Figure 8.3(f), the positions of the scattering peaks can be described by the equation¹¹

$$q_n = \frac{2\pi}{a} \sqrt{h^2 + k^2 + l^2} \quad (8.13)$$

By varying h, k, l values, one could obtain the peak positions for scattering on such a system as q ($(h,k,l)=(1,0,0)$), $\sqrt{2} q$ ($(h,k,l)=(1,1,0)$), $\sqrt{3} q$ ($(h,k,l)=(1,1,1)$), $2q$ ($(h,k,l)=(2,0,0)$), and so on. Thus it results in peak position ratios of $1 : \sqrt{2} : \sqrt{3} : 2 : \sqrt{5} : \sqrt{6}$.

For a BCC as shown in Figure 8.3(c), the positions of the scattering peaks can also be described by the Eqn. 8.13, however, $h+k+l$ must be even. By varying h, k, l values, one could obtain the peak positions for scattering on such a system as $\sqrt{2} q$ ($(h,k,l)=(1,1,0)$), $2q$ ($(h,k,l)=(2,0,0)$), $\sqrt{6} q$ ($(h,k,l)=(2,1,1)$), $\sqrt{8} q$ ($(h,k,l)=(2,2,0)$), and so on. Thus we would also have peak position ratios of $1 : \sqrt{2} : \sqrt{3} : 2 : \sqrt{5} : \sqrt{6}$.

For a Pm3n structure as shown in Figure 8.3(e), the positions of the scattering peaks can also be described by the Eqn. 8.13, however, the scattering peaks will only be observed at $\sqrt{2} q$ ($(h,k,l)=(1,1,0)$), $2q$ ($(h,k,l)=(2,0,0)$), $\sqrt{5} q$ ($(h,k,l)=(2,1,0)$), $\sqrt{6} q$ ($(h,k,l)=(2,1,1)$), $\sqrt{8} q$ ($(h,k,l)=(2,2,0)$), and so on. Thus we would have peak position ratios of $\sqrt{2} : 2 : \sqrt{5} : \sqrt{6} : \sqrt{8} : \sqrt{10}$.

For other common lattice structures, the peak position ratios are summarized in Table 8.1.¹² Thus, by analyzing the ratios of SAXS peaks and combining information from TEM and AFM, one can obtain detailed morphological information of block copolymers.

Table 8.1. Peak position ratios of common lattice structures observed in block copolymers (Reprinted with permission from Burger, C.; Hsiao, B. S.; Chu, B. In *Polymer Science: A Comprehensive Reference*; Matyjaszewski, K., Möller, M., Eds.; Elsevier: Amsterdam, 2012, p 363. Copyright, Elsevier, 2012)

Macro lattice Structure	Peak Position Ratios
Lamellae	1 : 2 : 3 : 4 : 5 : 6
Hexagonally close-packed cylinders	1 : $\sqrt{3}$: 2 : $\sqrt{7}$: 3 : $\sqrt{12}$
Primitive cubic	1 : $\sqrt{2}$: $\sqrt{3}$: 2 : $\sqrt{5}$: $\sqrt{6}$
Body centered cubic	1 : $\sqrt{2}$: $\sqrt{3}$: 2 : $\sqrt{5}$: $\sqrt{6}$.
Pm3n	$\sqrt{2}$: 2 : $\sqrt{5}$: $\sqrt{6}$: $\sqrt{8}$: $\sqrt{10}$
Double diamond (DD)	$\sqrt{2}$: $\sqrt{3}$: 2 : $\sqrt{6}$: $\sqrt{8}$: 3 : $\sqrt{10}$
Face centered cubic (FCC)	$\sqrt{3}$: 2 : $\sqrt{8}$: $\sqrt{11}$: $\sqrt{12}$: 4 : $\sqrt{19}$
Double gyroid	$\sqrt{3}$: 2 : $\sqrt{7}$: $\sqrt{8}$: $\sqrt{10}$: $\sqrt{11}$: $\sqrt{12}$
Hexagonally closed-packed spheres	$\sqrt{32}$: 6 : $\sqrt{41}$: $\sqrt{68}$: $\sqrt{96}$: $\sqrt{112}$: $\sqrt{118}$
Fddd	$\sqrt{12}$: $\sqrt{18}$: $\sqrt{36}$: 6 : $\sqrt{39}$: $\sqrt{45}$

8.2 Recent Published Results

8.2.1 Morphological Properties of A Series of Sulfonated Poly(arylene ether sulfone) (BPSH-BPS) Multiblock Copolymer (MBC) Ionomers¹³

Today, fuel cells have been considered as an alternative source for stationary power and transportation applications.^{14,15} One type of fuel cells have been extensively studied by researchers is Proton Exchange Membrane Fuel Cells (PEMFC), which has diverse energy potential. Currently, Nafion is studied as the benchmark material in PEMFC, but Nafion has several drawbacks including high cost to produce, low performance at high temperature and under low humidity and high crossover. Due to these drawbacks of Nafion, some other types of membranes for fuel cells have been synthesized and studied. Among them, hydrocarbon based sulfonated block copolymers are one class of promising alternative

membranes for fuel cells.¹⁶ Research from the McGrath group has focused upon the development of poly(arylene ether sulfone) multiblock copolymer (MBC) ionomers. The acronym for these materials is based on BP representing Biphenol, S for sulfone, H for the acidified form, and xx is the degree of disulfonation (BPSH-xx or BPS-xx). A series of BPSH-BPS (x:y) MBC ionomers with x and y representing the block lengths of the oligomers were synthesized. The chemical structure of these block copolymer is shown in Figure 8.4. In order to fully understand the properties of these block copolymer, we have been collaborating with Dr. Y. Fan from Prof. C. J. Cornelius research group, and established the structure-property relationship for these copolymers.

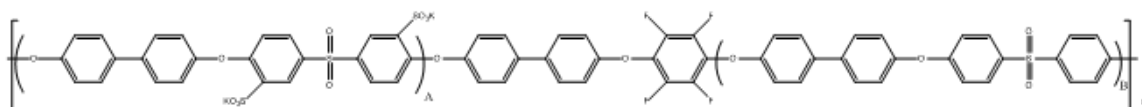


Figure 8.4. Chemical structure of BPSH-BPS MBC monomers, and material were obtained from Prof. McGrath’s research group (Reprinted with permission from *Polymer* **2011**, 52, 3963. Copyright, Elsevier, 2011)

When a volumetric based ion exchange capacity (IEC_v) is used to compare proton conductivities, these materials display conductivities that are comparable to Nafion. Previous TEM and AFM studies of these materials clearly show a phase-separated morphology, and both the degree of phase separation and the distance between different phases are enhanced by increasing block lengths.¹⁷ To further investigate the morphological information and structure-property relationship of these copolymers, through-plane SAXS experiments have been performed on a series of these copolymers with different block length, and the results are shown in Figure 8.5. For all MBC ionomers, SAXS profiles show a scattering maxima, denoted as q_{\max} , which is due to the phase separation between two different blocks in the MBC ionomers. This q_{\max} shifts to higher q

value as the block length increases, which indicates an increase in the inter-domain distance. These inter-domain distances can be estimated by using Bragg's law ($d=2\pi/q_{\max}$), and the calculated results are listed in Table 8.2. These results clearly show that the inter-domain distance between different phases within MBC ionomers is a function of block length, which is consistent with our previous results.¹⁷ Furthermore, for all three MBC ionomers, a weak second order peak at $2q_{\max}$ could be observed. Consistent with our previous SAXS and TEM results on similar copolymer,¹⁷ this scattering behavior suggests the presence of a highly ordered and periodic structure within MBC ionomers, which probably have a lamellar morphology.¹⁷ Furthermore, the 2nd order peak in BPS-BPSH 5K is much weaker than that of BPS-BPSH 15K, which may also suggest that increase in block length would improve the phase separation within MBC ionomers. These improvements in phase separation with increasing block length may improve the mechanical properties as well as proton transport. Dr. Y. Fan performed gas permeability experiments on these copolymers, and it is observed that the H₂ permeability is strongly influenced by the block length as shown in Table 8.3, which decreased as the block length increased from 5K to 15K at a fixed temperature. This may be due to the polymer chain dilation and the increase in the inter-domain distance between the blocks.

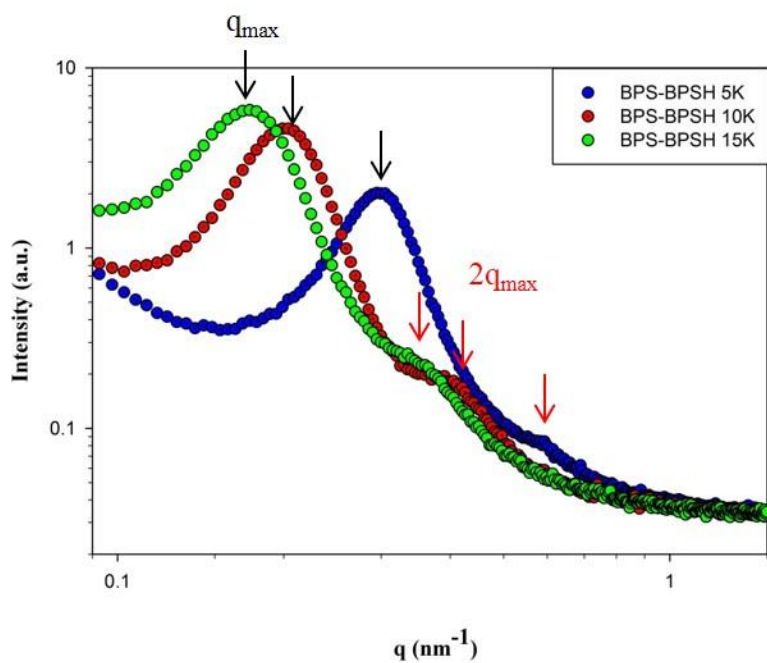


Figure 8.5. SAXS profiles of BPSH-BPS MBC ionomer (Reprinted with permission from *Polymer* **2011**, 52, 3963. Copyright, Elsevier, 2011)

Table 8.2. SAXS domain space comparison for the data in Figure 8.5 (Reprinted with permission from *Polymer* **2011**, 52, 3963. Copyright, Elsevier, 2011)

Sample	q_{\max} (nm^{-1})	$2q_{\max}$ (nm^{-1})	interdomain distance (nm)
BPS-BPSH 5K	0.294	0.587	21.4
BPS-BPSH 10K	0.200	0.406	31.4
BPS-BPSH 15K	0.173	0.356	36.3

Table 8.3. H₂ permeability coefficient at 5 atm of BPSH-BPS MBC ionomers, and data were collected by Dr. Y. Fan. (Reprinted with permission from *Polymer* **2011**, 52, 3963. Copyright, Elsevier, 2011)

Temperatures (°C)	BPS-BPSH 5K (Barrers)	BPS-BPSH 10K (Barrers)	BPS-BPSH 15K (Barrers)
30	3.2	3.0	2.5
50	5.4	4.9	4.3
70	8.3	7.2	6.4
90	13.0	11.1	9.8

8.2.2 Characterization of Multiblock Partially Fluorinated Hydrophobic Poly(arylene ether nitrile) Hydrophilic Disulfonated Poly(arylene ether sulfone) Copolymers for Proton Exchange Membranes¹⁸

A series of multiblock copolymers with various block lengths and ion exchange capacities (IEC) were synthesized with alternating segments of phenoxide terminated fully disulfonated poly(arylene ether sulfone) (BPS100) and fluorine-terminated poly(arylene ether benzonitrile) (6FPAEB) by our collaborator, Dr. Y. Chen from Prof. J. E. McGrath's research group. The chemical structure of this 6FPAEB-BPS100 multiblock copolymers are shown in Figure 8.6. In order to obtain morphological information and establish structure-properties relationship of these copolymers, SAXS was used to study the morphologies of these new series of multiblock copolymers.

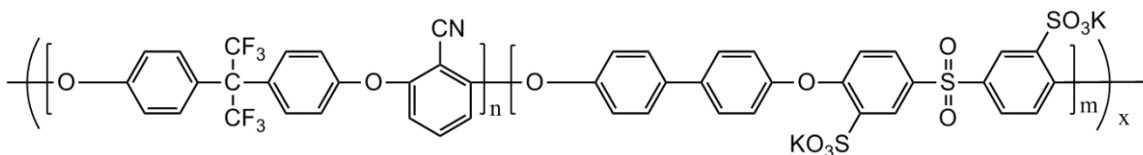


Figure 8.6. Chemical structure of 6FPAEB-BPS100 multiblock, and copolymers were synthesized by Dr. Yu Chen from Prof. McGrath's research group (Reprinted with permission from *Journal of Polymer Science Part A: Polymer Chemistry* **2013**, 51, 2301. Copyright, Elsevier, 2011)

The 6FPAEB-BPS100 multiblock copolymer membranes were cast from dimethylacetamide (DMAc) and annealed under vacuum at 220 °C which is about 30 °C higher than the T_g of 6FPAEB blocks. The SAXS profiles of the membranes are presented in Figure 8.7. The profiles of 6FPAEB-BPS100 multiblock copolymer membranes exhibit scattering maxima, while the SAXS profile for the random copolymer membrane 6FPAEB35 does not show a distinct phase separation peak. The observed scattering maxima in the profiles of 6FPAEB-BPS100 series membranes are attributed to the aggregated nano-phase separated ionic domains. With increasing block length, the scattered intensity of 6FPAEB-BPS100 increases, suggesting that the longer block improves the aggregation of ionic domains. The SAXS profiles of 6FPAEB-BPS100 multiblock copolymer membranes also confirm the presence of the ordered periodic microstructures and its dependence on the block length of the oligomers. The long-range ordered periodic microdomain structure in block copolymers can be obtained from the relative positions of multiple scattering peaks in the SAXS profiles. For a lamellar structure, the SAXS profile shows a series peaks with the q value at q_{\max} , $2q_{\max}$, $3q_{\max}$..., where q_{\max} is the scattering wave vector of the main scattering maxima.¹⁷ For all of the three 6FPAEB-BPS100 multiblock copolymer membranes, two scattering peaks are clearly observed in each SAXS profile. The first order peak is at q_{\max} and the second order peak is

at $2q_{\max}$, which suggests the presence of the highly ordered lamellar structure. The intensity of the second order peak for 6FPAEB-BPS100 7k-7k is lower than those of 11k-11k and 15k-15k, which suggests the short block lengths induce ionic domain aggregation, but prevents the formation of a well-ordered lamellar structure. It is also observed that with increasing block length for 6FPAEB-BPS100 series, the main scattering peak shifts to the lower q values. This behavior indicates that the interdomain distance increases as the block length increases.

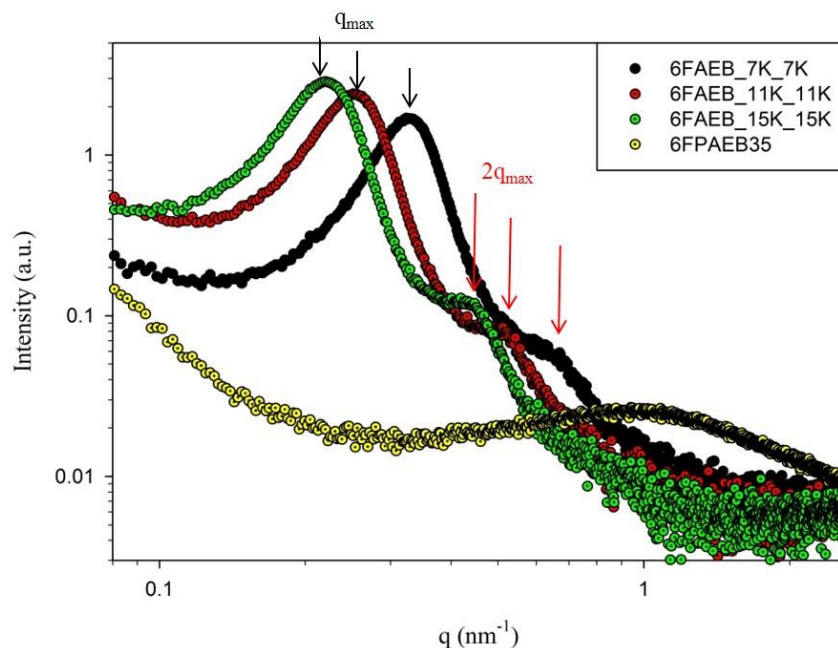


Figure 8.7. SAXS profiles of 6FPAEB-BPS100 (Reprinted with permission from *Journal of Polymer Science Part A: Polymer Chemistry* **2013**, 51, 2301. Copyright, Elsevier, 2011)

The observed morphology can be used to explain the increase in proton conductivity with increasing block lengths as shown in Table 8.3. (Data were collected by Dr. Y. Chen from Prof. J. E. McGrath's research group) The enhanced nano-phase separated lamellar morphology with increasing block length will form enhanced co-continuous hydrophilic

channels, which will lower the morphological barrier for proton transport. Thus it results in an increase in proton conductivity with increasing block length.

Table 8.4. Proton conductivity of 6FBPS0-BPSH100 block copolymer measure in liquid water at 30 °C, and data were collected by Dr. Y. Chen from Prof. J. E. McGrath's research group (Reprinted with permission from Journal of Polymer Science Part A: Polymer Chemistry **2013**, 51, 2301. Copyright, Elsevier, 2011)

6FBPS0-BPSH100	Proton Conductivity (S/cm)
4k-4k	0.14
6k-6k	0.17
8k-8k	0.17
10k-10k	0.18
12k-12k	0.19
15k-15k	0.20

8.2.3 Morphological Characterization of Multiblock Poly(arylene ether nitrile) Disulfonated Poly(arylene ether sulfone) Copolymers for Proton Exchange Membranes¹⁹

The morphology of another similar multiblock copolymers that are synthesized by J. R. Rowlett from Prof. J. E. McGrath's research group were also studied by using SAXS. The structures of these copolymers are shown in Figure 8.8.

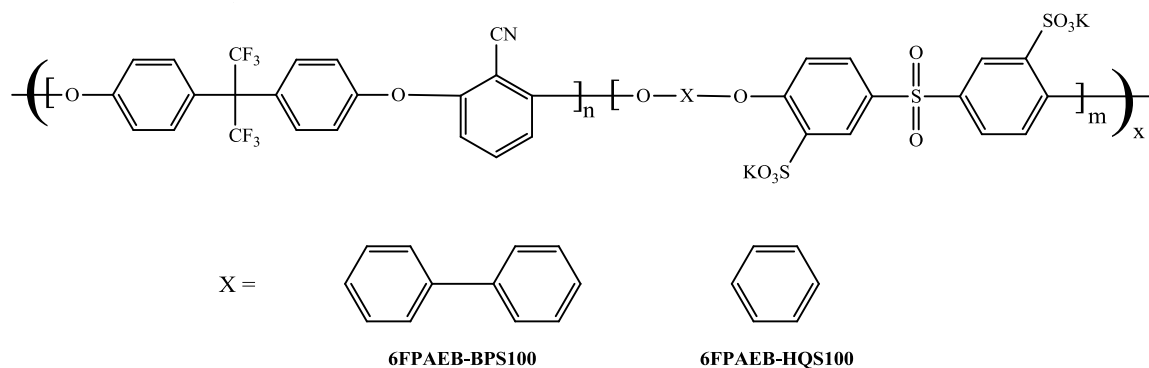


Figure 8.8. Structures of multiblock poly(arylene ether nitrile) disulfonated poly(arylene ether sulfone) copolymers (6FPAEB-BPS100, and 6FPAEB-HQS100), and copolymers were synthesized by Jarrett R. Rowlett from Prof. J. E. McGrath's research group (Reprinted with permission from *Polymer* **2013**, 54, 6305. Copyright, Elsevier, 2013)

SAXS can be used to determine the lamellar structure in semicrystalline polymers, dimensions of phase-separation in block copolymers and heterogeneities in ionomers. The scattered intensity versus the magnitude of the scattering vector q profile is often used to represent the patterns of SAXS. The profiles of the multiblock copolymers membranes cast with DMAc and annealed are presented in Figure 8.9. In the investigated range of scattering vectors, the profiles of the multiblock copolymer membranes exhibit scattering maxima, while the SAXS profile of the 6FPAEB-35 random copolymer membrane is featureless. The observed scattering maxima in the profiles of 6FPAEB-BPS100 and 6FPAEB-HQS100 membranes are attributed to the aggregated nano-phase separated ionic domains. In addition, as the block length increased for the biphenol based multiblock copolymers the scattered intensity also increased, which suggests that the longer blocks induced an enhanced degree of phase separation. The SAXS profiles of these three multiblock copolymers show a primary peak at q_{\max} , and also a secondary peak at $2 q_{\max}$, which is consistent with the scattering behaviors on similar multiblock copolymer systems in our previous studies. This may suggest that 6FPAEB-BPS100 series multiblock copolymers

with longer block lengths also exhibit lamella morphology. Additionally when comparing the 7K-7K block lengths of the two different systems, the hydroquinone based multiblock copolymer had a much clearer secondary peak, which indicates that the higher IEC systems allowed for enhanced phase separation at lower block lengths over that of biphenol analogs. From TEM studies (data collected by J. R. Rowlett from Prof. J. E. McGrath's research group) in Figure 8.10, it further confirms these two trends observed in the SAXS profiles and the existence of a lamellar morphology for the 6FPAEB-BPS100 15K-15K multiblock copolymer. While for 6FPAEB-BPS100 7K-7K, the 2nd order peak is weaker and broader than those of the longer block lengths, which suggests that the short block length with induced ionic domain aggregation prevents the formation of well ordered lamellar structure. This is consistent with the TEM study that 6FPAEB-BPS100 7K-7K showed a disordered morphology in Figure 8.10. Enhanced phase separation yields more distinct and ordered ionic domains. It was also observed that as the block length and charge density of the multiblock copolymers increased, the main scattering peak shifted to lower q values. This behavior indicates that interdomain distance increased as block length increased.

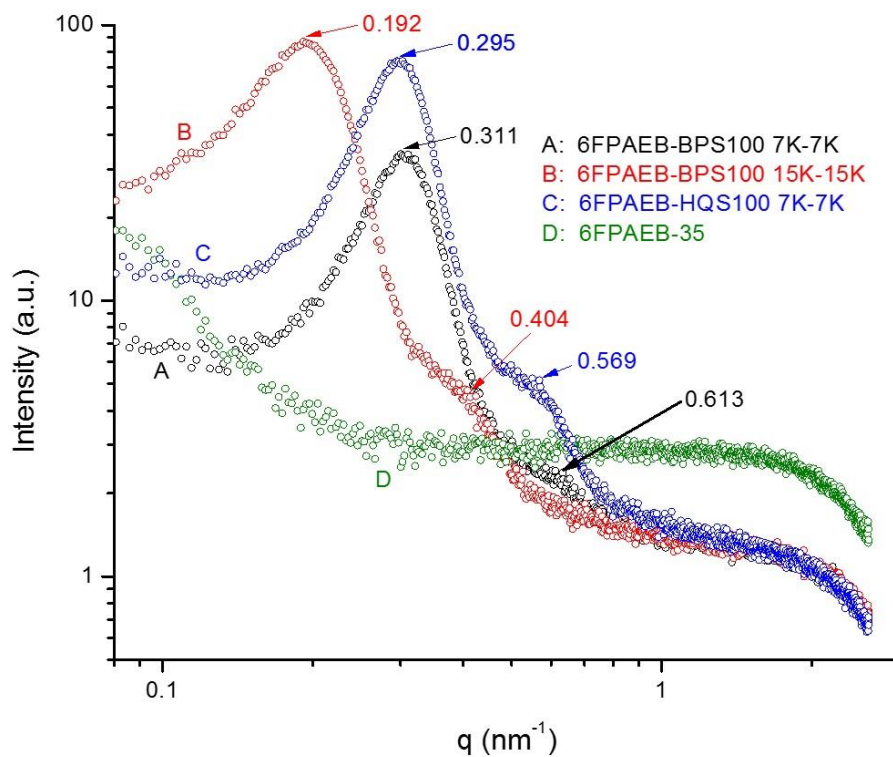


Figure 8.9. SAXS profiles of 6FPAEB-BPS100 and 6FPAEB-HQS100 multiblock copolymers and 6FPAEB35 random copolymer membrane (Reprinted with permission from *Polymer* **2013**, 54, 6305. Copyright, Elsevier, 2013)

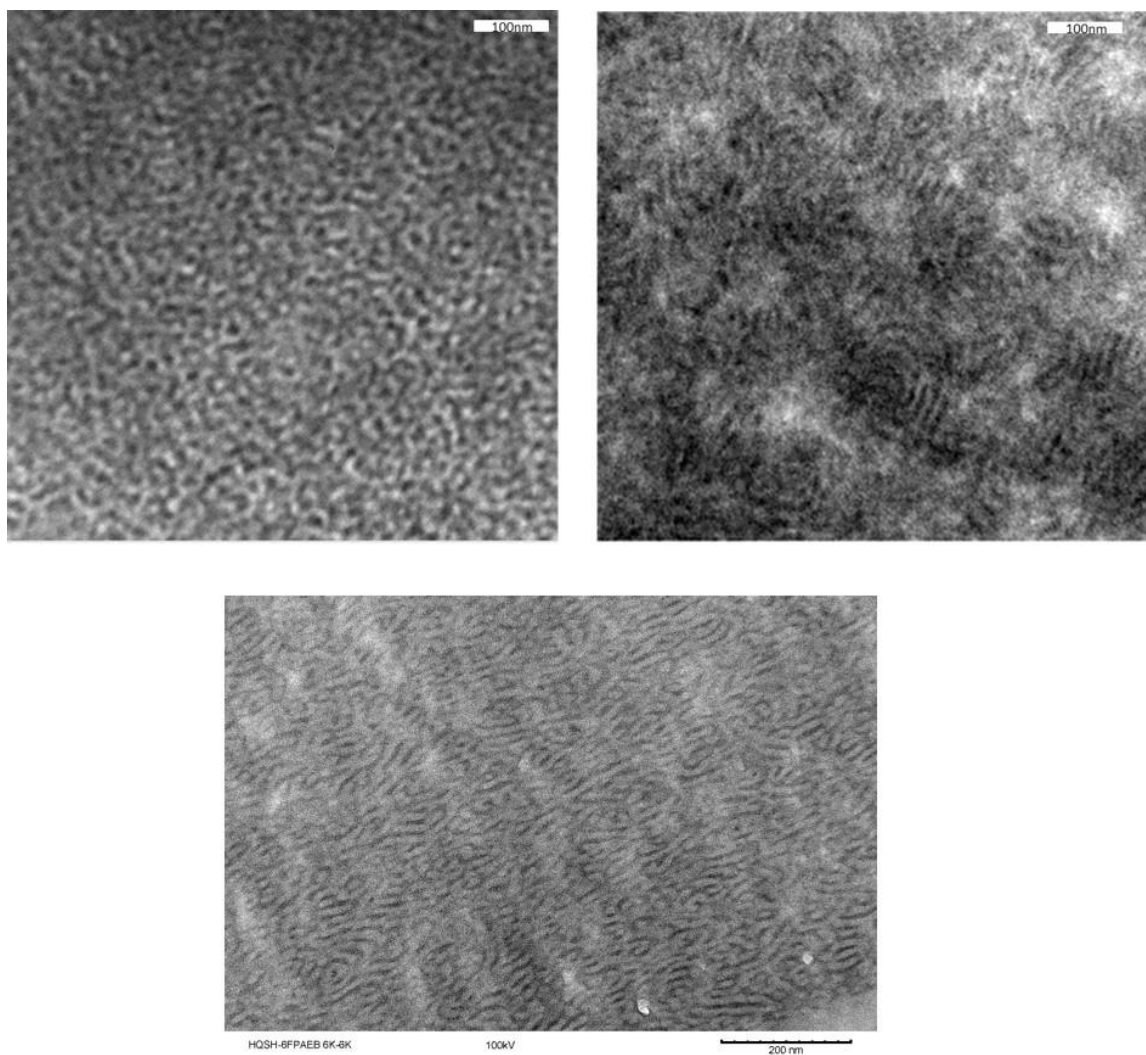


Figure 8.10. TEM images of 6FPAEB-BPSH (top left: 7K-7K, top right: 15K-15K) and 6FPAEB-HQSH (bottom 7K-7K) multiblock copolymer membranes, and data were collected by J. R. Rowlett from Prof. J. E. McGrath's research group (Reprinted with permission from *Polymer* **2013**, 54, 6305. Copyright, Elsevier, 2013)

8.2.4 Morphological Characterization of 4-vinylimidazole ABA triblock copolymers²⁰

4-vinylimidazole (4VIM)-containing ABA triblock copolymers (Figure 8.11) were synthesized via a difunctional RAFT chain transfer agent by Dr. M. H. Allen from Prof. T. E. Long's research group. SAXS experiments were performed on a series of these copolymers with variable weight percent of different blocks to study the morphology and

establish structure-property relationship of these copolymers. The scattering profiles are shown in Figure 8.11. Plots of log-log of scattering intensity-scattering vector were constructed to better reveal the scattering behaviors of these copolymers. The scattering plots were also vertically shifted in order to display the influence of wt% of VIM block on the morphology of these copolymers. For all the copolymers, a scattering maxima was observed at low q values, which is due to the microphase phase separation between different blocks within the ABA triblock copolymer. Bragg's law ($d=2\pi/q^*$) was used to estimate the average distance between different blocks in the ABA copolymer, and the results listed in Table 8.5. Furthermore, for both the 30 wt% and 40 wt% 4VIM-containing triblock copolymer, a clear secondary peak at $2q^*$ was observed, which suggests the presence of a highly ordered and periodic structure that may have lamellar morphology. While for 40 wt% 4VIM-containing, a clear fifth order peak at $5q^*$ was also observed, which may indicate an even more well-ordered lamella structure. However, for 20 wt% 4VIM-containing triblock polymers, no higher order peak was observed, which may be due to the lack of sufficient thermal annealing in these samples, resulting in a less ordered structure. One thing needs to notice here is that for both 30 wt% and 40 wt% 4VIM-containing triblock copolymer, only odd scattering maxima were observed, which may be due to the fact that even-ordered peaks coincide with minima in the form factor scattering when the volume fraction of one component is near 50 %.²¹

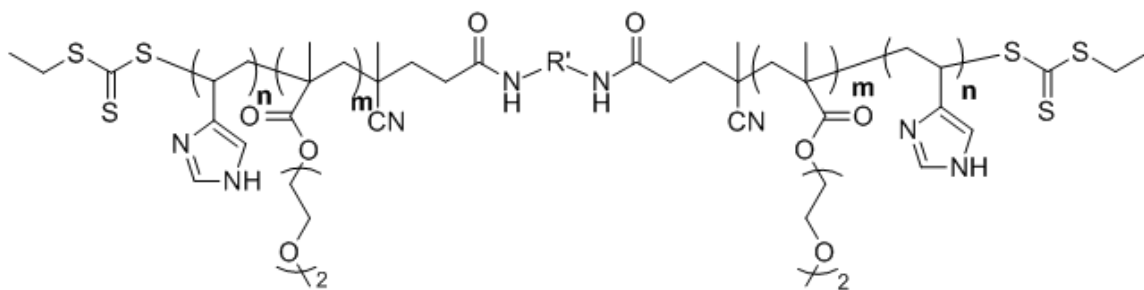


Figure 8.11. Chemical structures of poly(4VIM-*b*-DEGMEMA-*b*-4VIM) triblock copolymers, and copolymers were synthesized and by Dr. M. H. Allen from Prof. T. E. Long's research group (Reprinted with permission from *Polymer Chemistry* **2013**, *4*, 2333. Copyright, RSC Publishing, 2013)

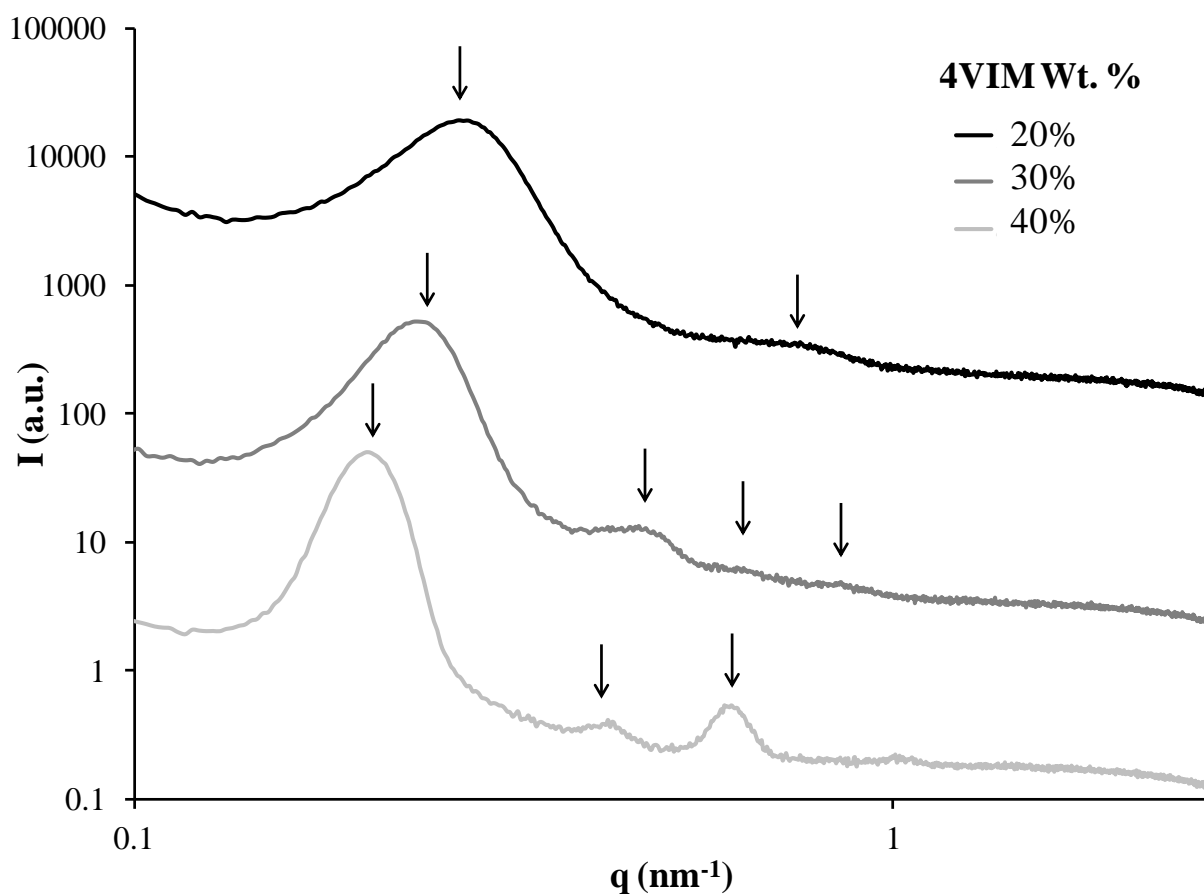


Figure 8.14. SAXS profiles of scattering intensity versus scattering vector for poly(4VIM-*b*-DEGMEMA-*b*-4VIM) triblock copolymers (Reprinted with permission from *Polymer Chemistry* **2013**, *4*, 2333. Copyright, RSC Publishing, 2013)

Table 8.5. SAXS q values and Bragg spacings (Reprinted with permission from Polymer Chemistry **2013**, 4, 2333. Copyright, RSC Publishing, 2013)

4VIM Wt.%	q (nm ⁻¹) (1st order peak)	Distance (nm)	q (nm ⁻¹) (2nd order peak)	q (nm ⁻¹) (3rd order peak)	q (nm ⁻¹) (4th order peak)
20%	0.27	23.3	0.77	--	--
30%	0.24	26.2	0.47	0.64	0.85
40%	0.20	31.4	0.42	0.61	--

In order to further demonstrate the disappearance of even order scattering maxima, we assume that the lamella thickness distribution to be Gaussian, with d_a as the average thickness and σ_a as the standard deviation of layer a , d_b as the average thickness and b as the standard deviation of layer σ_b , one can obtain the relative height of the scattering peaks of the successive order n by the following equation,⁷

$$I_1(q) = 16N \frac{(\Delta\rho)^2}{q^4} \frac{\sigma_b^2 \sin^2(qd_a/2) + \sigma_a^2 \sin^2(qd_b/2)}{(\sigma_a^2 + \sigma_b^2) + (16/q^4) \sin^2(q(d_a + d_b/2))} \quad (8.14)$$

where N is number of lamellae stacks; $\Delta\rho$ is the scattering length density difference between lamellae of phase a and lamellae of phase b . By varying the volume fraction of phase a , assuming that volume fraction of a to be the thickness fraction of layer a in the lamella, one can obtain that as volume fraction of phase a approaches 50%, the intensity of the even order peaks starts to decrease while the intensity of odd order peaks remain unchanged. Furthermore, it is observed that at 50% volume fraction of phase a , the second order peak is even totally unobservable. (Figure 8.11)

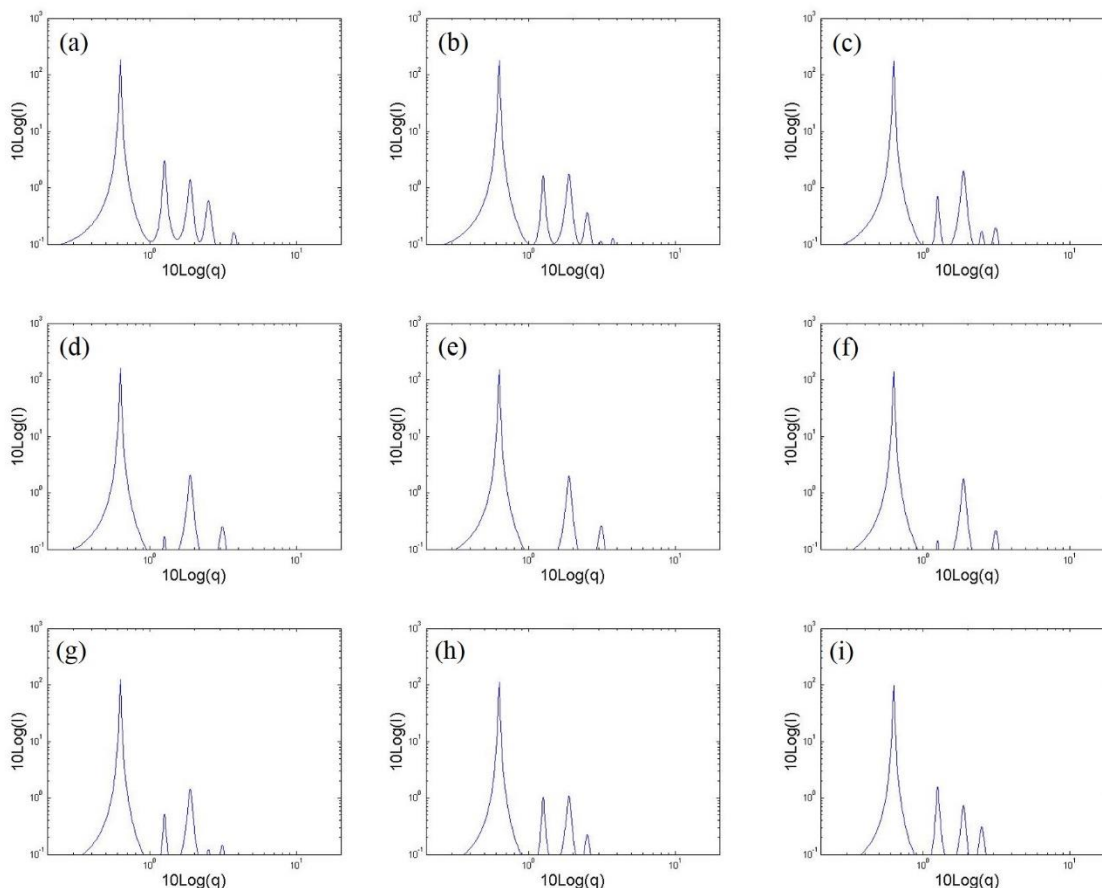


Figure 8.12. SAXS profiles with varying volume fraction of phase. (a) vol%(a)=0.42; (b) vol%(a)=0.44; (c) vol%(a)=0.46; (d) vol%(a)=0.48; (e) vol%(a)=0.50; (f) vol%(a)=0.52; (g) vol%(a)=0.54; (h) vol%(a)=0.56; (i) vol%(a)=0.58

Another scattering behavior needs to be pointed out here is that scattering maxima q^* shifted to lower q values as the weight percent of 4VIM increased in the triblock copolymers, which indicates a larger domain separation and higher degree of phase separation within the nanostructures. In order to further investigate this morphological property, TEM and AFM (Figure 8.13) were performed by Dr. M. H. Allen from Prof. T. E. Long's research group to confirm the presence of highly ordered lamellar structures in the 40 wt. % 4VIM triblock copolymers. The TEM and AFM images clearly showed the

appearance of clear, highly ordered lamellar morphologies in the triblock copolymers with higher composition of 4VIM, which further confirms the high degree of nano-phase separation within these triblock films. However, for 20 wt%4VIM-containing triblock copolymer, such morphology was neither observed in TEM nor AFM experiments, which demonstrate the composition of triblock copolymer as well as sufficient thermal annealing would strongly affect the morphology of these ABA triblock copolymers

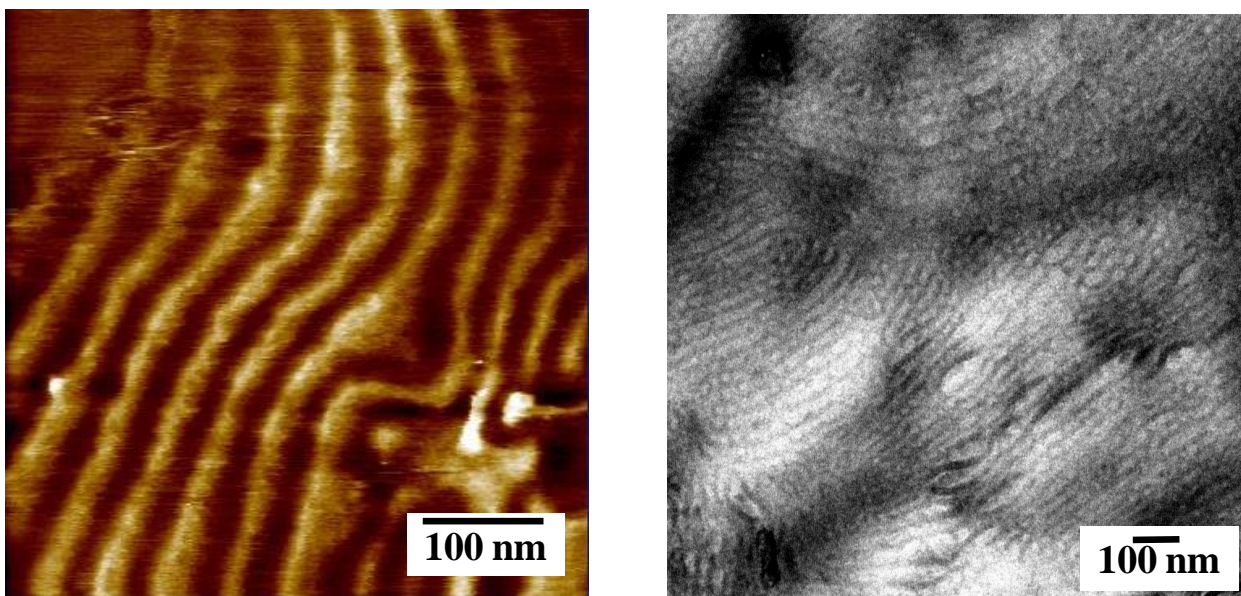


Figure 8.13. AFM phase image in tapping mode and TEM image of 40 wt. % 4VIM-containing ABA triblock copolymer, and data were collected by Dr. M. H. Allen from Prof. T. E. Long's research group (Reprinted with permission from *Polymer Chemistry* **2013**, *4*, 2333. Copyright, RSC Publishing, 2013)

8.2.5 Morphological Characterization of Perfectly Alternating Polycarbonate-Polydimethylsiloxane Multiblock Copolymers Possessing Controlled Block Lengths²²

One particular multiblock copolymer, polycarbonate-polydimethylsiloxane (PC-PMDS) multiblock copolymer has caused researchers' interest due to its good thermal stability, flame resistance, weatherability, high polymer chain flexibility, and good oxygen and nitrogen permselectivity associated with PDMS. In this collaboration work with Prof. B. J. Chisholm's research group, we investigated the morphology of perfectly alternating

PC-PDMS multiblock copolymers, (Figure 8.14) and utilized these morphological information to successfully explain the thermal and mechanical properties of these copolymers.

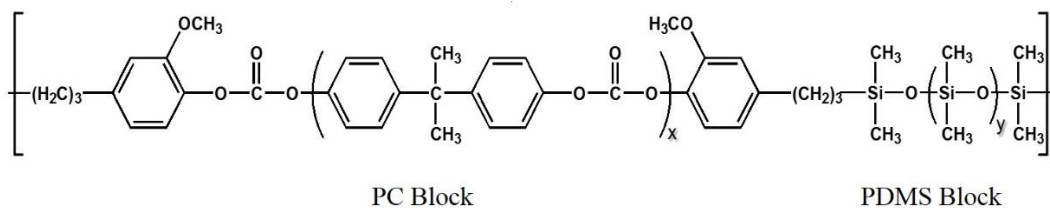


Figure 8.14. Chemical structure of PC-PDMS multiblock copolymers, and copolymers were obtained from Prof. B. J. Chisholm's research group (Reprinted with permission from *Polymer Engineering & Science* **2013**. Copyright, Wiley Online Library, 2013)

In this study, SAXS was utilized to provide a better understanding of nano-scale phase separation of the multiblock copolymers. The scattering results are shown in Figure 8.15 and the profiles were vertically shifted to facilitate a comparison of the peak positions. Estimates of average interdomain spacings were calculated using Bragg's law and listed in Table 8.6. It is first noted that for the pure PC homopolymer, the scattering intensity decreases monotonically with increasing q which is consistent with a lack of structure (as expected). For the commercial PC-PDMS random block polymer, a diffuse peak at $q \approx 0.21 \text{ nm}^{-1}$ is observed. A diffuse scattering peak suggests morphological heterogeneity. The heterogeneity may be caused by a large distribution of domain sizes, differences in domain ordering or by compositional variations of the components within the domains. For the 3KPC series of multiblock copolymers, the 3KPC(81%)-0.7KPDMS(19%) shows a broad scattering peak at $q \approx 1 \text{ nm}^{-1}$. As the length of PDMS increases, the primary peak shifts to lower q value, indicating an increase in the phase-separation distance. For 3KPC(73%)-1.1KPDMS(27%) and 3KPC(38%)-6KPDMS(62%), a much sharper peak is observed, indicating a more uniform distribution of phase separation spacing. Furthermore,

a clear secondary peak at $2q_{\max}$ is observed, which suggests the presence of a highly ordered lamellar structure. As the length of PDMS blocks increase, a third order peak ($3q_{\max}$) at $q \approx 1 \text{ nm}^{-1}$ is observed for 3KPC(38%)-6KPDMS(62%), indicating an even more well-ordered lamella structure. This data is consistent with the low M_n of PDMS results where there is a higher degree of phase mixing between the PC and PDMS blocks. Higher M_n of PDMS results in greater phase separation between the PC and PDMS blocks. For the 5KPC series of multiblock copolymers, a much broader phase-separation peak is observed for 5KPC(87%)-7KPDMS(13%), indicating a higher degree of phase mixing between PC and PDMS at low M_n of PDMS.

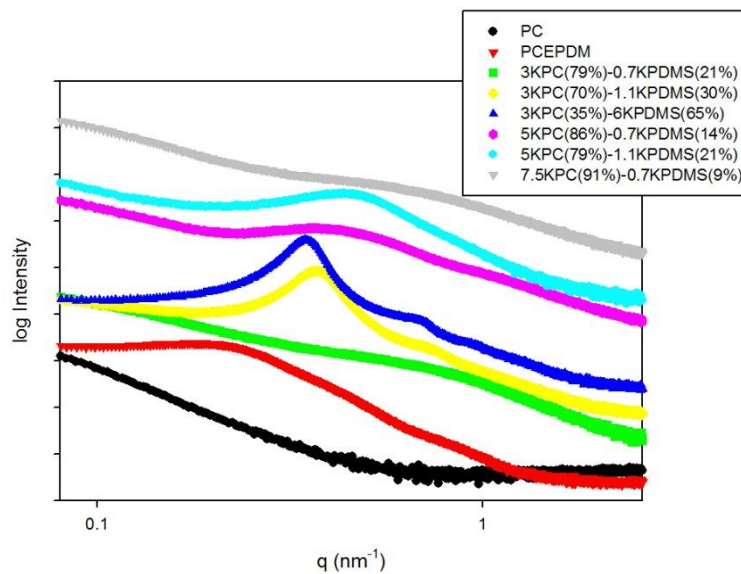


Figure 8.15. SAXS profiles for PC-PDMS multiblock copolymers. The SAXS profiles have been vertically shifted to facilitate a comparison of the peak positions (Reprinted with permission from *Polymer Engineering & Science* **2013**. Copyright, Wiley Online Library, 2013)

Table 8.6. Interdomain spacings for selected polymers (Reprinted with permission from Polymer Engineering & Science **2013**. Copyright, Wiley Online Library, 2013)

Sample Designation	q_{\max} (nm ⁻¹)	D (nm)	$2q_{\max}$	$3q_{\max}$
PC	----			
PCEPDM	0.22	29		
3KPC(81%)- 0.7KPDMS(19%)	0.81	7.6		
3KPC(73%)- 1.1KPDMS(27%)	0.37	17	0.74	
3KPC(38%)- 6KPDMS(62%)	0.35	18	0.69	0.96
5KPC(87%)- 0.7KPDMS(13%)	0.45	14		
5KPC(80%)- 1.1KPDMS(20%)	0.45	14		
7.5KPC(91%)- 0.7KPDMS(9%)	0.74	8.5		

8.3 Acknowledgements

We would like to thank all our collaborations in these studies, Dr. Yanfang Fan, Dr. Yu Chen, Jarrett R. Rowlett, Dr. Michael H. Allen, Prof. Chris J. Cornelius, Prof. Timothy E. Long, and Prof. Bret J. Chisholm. This material is partially based upon work supported by the National Science Foundation under Grant No. DMR-0923107.

8.4 References

- (1) Hamley, I. W. *The physics of block copolymers*; Oxford University Press: Oxford; New York, 1998.
- (2) In *Developments series*; Applied Science: London ; New York, 1982, p v.
- (3) Lazzari, M.; Liu, G.; Lecommandoux, S. b. *Block copolymers in nanoscience*; Wiley-VCH; John Wiley distributor: Weinheim, Chichester, 2006.

- (4) Schacher, F. H.; Rugar, P. A.; Manners, I. *Angewandte Chemie International Edition* **2012**, *51*, 7898.
- (5) Fredrickson, G. H.; Bates, F. S. *Annual Review of Materials Science* **1996**, *26*, 501.
- (6) Khandpur, A. K.; Foerster, S.; Bates, F. S.; Hamley, I. W.; Ryan, A. J.; Bras, W.; Almdal, K.; Mortensen, K. *Macromolecules* **1995**, *28*, 8796.
- (7) Roe, R.-J. *Methods of X-ray and Neutron Scattering in Polymer Science*; Oxford University Press, Inc. : New York, 2000.
- (8) Porod, G. *Kolloid-Zeitschrift* **1951**, *124*, 83.
- (9) Peiser, H. S. *X-ray diffraction by polycrystalline materials*; Institute of Physics: London,, 1955.
- (10) Guinebretiere, R. *X-ray diffraction by polycrystalline materials*; ISTE: London ; Newport Beach, CA, 2007.
- (11) Balny, C.; Masson, P.; Heremans, K. *Frontiers in high pressure biochemistry and biophysics*; Elsevier: Amsterdam ; New York, 2002.
- (12) Burger, C.; Hsiao, B. S.; Chu, B. In *Polymer Science: A Comprehensive Reference*; Matyjaszewski, K., Möller, M., Eds.; Elsevier: Amsterdam, 2012, p 363.
- (13) Fan, Y.; Zhang, M.; Moore, R. B.; Lee, H.-S.; McGrath, J. E.; Cornelius, C. *J. Polymer* **2011**, *52*, 3963.
- (14) Neburchilov, V.; Martin, J.; Wang, H.; Zhang, J. *Journal of Power Sources* **2007**, *169*, 221.
- (15) Kocha, S. S.; Deliang Yang, J.; Yi, J. S. *AIChE Journal* **2006**, *52*, 1916.

- (16) Lee, H.-S.; Roy, A.; Lane, O.; Dunn, S.; McGrath, J. E. *Polymer* **2008**, *49*, 715.
- (17) Lee, M.; Park, J. K.; Lee, H.-S.; Lane, O.; Moore, R. B.; McGrath, J. E.; Baird, D. G. *Polymer* **2009**, *50*, 6129.
- (18) Chen, Y.; Rowlett, J. R.; Lee, C. H.; Lane, O. R.; VanHouten, D. J.; Zhang, M.; Moore, R. B.; McGrath, J. E. *Journal of Polymer Science Part A: Polymer Chemistry* **2013**, *51*, 2301.
- (19) Rowlett, J. R.; Chen, Y.; Shaver, A. T.; Lane, O.; Mittelsteadt, C.; Xu, H.; Zhang, M.; Moore, R. B.; Mecham, S.; McGrath, J. E. *Polymer* **2013**, *54*, 6305.
- (20) Allen, M.; Hemp, S. T.; Zhang, N.; Zhang, M.; Smith, A.; Moore, R. B.; Long, T. *Polymer Chemistry* **2013**, *4*, 2333.
- (21) Winey, K. I.; Thomas, E. L.; Fetters, L. J. *Macromolecules* **1991**, *24*, 6182.
- (22) Majumdar, P.; Chernykh, A.; Bao, H.; Crowley, E.; Zhang, M.; Bahr, J.; Weisz, M.; Ulven, C.; Zhou, T.; Moore, R. B. *Polymer Engineering & Science* **2013**.

Chapter 9

Future Work: Methods to Enhance Microdomain Orientation within Nafion

9.1 Introduction

As it has been introduced in Chapter 2, researchers have utilized stretching technique to facilitate morphological and property studies in Nafion,¹⁻⁷ which could induce an alignment of the ionic domains or water channels along the stretching direction. In other words, stretching can be utilized as a means to enhance the microdomain orientation within Nafion. However, stretching will lead to changes in membrane dimensions, which will be undesired in many applications. In this chapter, several other methods without changing membrane dimensions are introduced as means to enhance the microdomain orientation within Nafion.

9.2 Methods to Enhance Microdomain Orientation in Polymers

9.2.1 Applying Electric Field to Enhance Microdomain Orientation

The effect of electric field on block copolymer microstructure was first studied by Amundson and co-workers.⁸ They showed that electric field could induce macroscopic anisotropy in block copolymers, and their ability in changing the microstructure depends not only on the strength of the electric field, but also on the size and shape of the regions that electric field acts on. Given that the electric field and size and shape of the regions satisfy certain conditions, both lamellar microstructure and cylindrical microstructure could be aligned parallel to the electric field. However, for spherical and bicontinuous

double-diamond microstructure, no preferential orientation would be achieved due to their symmetrical structures.

Later on, a detailed study on the kinetics and mechanisms of alignment of lamellar block copolymer microstructure in an electric field were performed by Amundson and co-workers.^{9,10} The anisotropic SAXS pattern that two arcs parallel to the electric field are observed (Figure 9.1 (A)), which clearly showed that alignment in the lamellar microstructure was achieved under electric field. A morphological model for aligned lamellar sample was proposed as shown in Figure 9.1 (B). The morphology of the lamella was different in the two slices directions, perpendicular slice direction and parallel slice direction, respectively. In the parallel slice direction, the lamellas were aligned parallel to the electric field, while in the perpendicular slice direction, slice plane was orthogonal to the electric field.

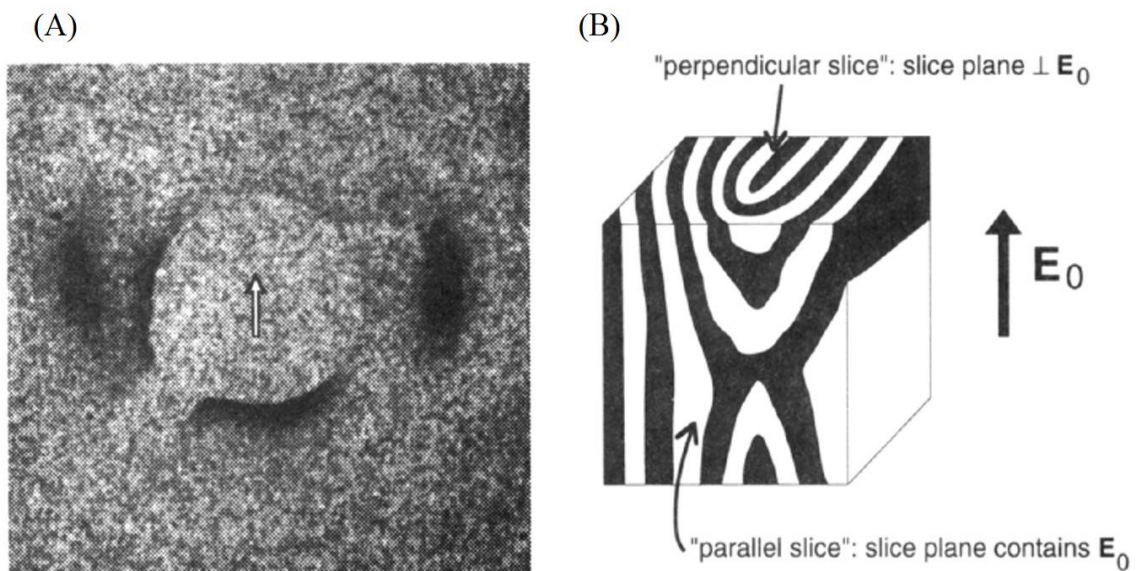


Figure 9.1. (A) SAXS pattern from the block copolymer sample after alignment in the electric field. The arrow shows that X-ray beam was orthogonal to the applied field direction. (B) Schema of the orientation of slice planes under the applied electric field (Reprinted with permission from *Macromolecules* **1993**, 26, 2698. Copyright, The American Chemistry Society, 1993)

Russell and co-workers¹¹ proposed that applying electric fields could also control the domain orientation in block copolymer thin film that is around 100 nm in thickness. They observed that without electric fields, the spin-coated poly(styrene-*block*-methyl methacrylate) (PS-*b*-PMMA) copolymer contained a large number of defects, as well as random orientation of PMMA cylinders in the PS matrix. However, when high in-plane electric fields were applied, a clearly better alignment of cylinders of PMMA in PS matrix parallel to the electric field with few defects was achieved. The high electric fields could be obtained by using small potentials with electrodes separated by very small distances.

A recent study following similar approach by Amundson and co-workers^{9,10} was performed on Nafion by Lin and co-workers.¹² The cast Nafion membranes were placed in the electric field with 15 kV voltage and a distance of 2.0 cm between the electrodes. However, the morphology of Nafion after placing in the electric field did not show distinct

difference from that of as-received Nafion. Furthermore, the proton conductivities of Nafion after applying electric field either in parallel direction or vertical direction were very similar to that of as-received Nafion, which indicates that applying electric field on Nafion dry membranes will not induce significant microdomain orientation.

9.2.2 Applying Magnetic Field to Enhance Microdomain Orientation

One issue with using electric field as a means to induce alignment is that dielectric breakdown would happen during electric field alignment. On the other hand, magnetic field has no such issue and could be a more attractive method for introducing alignment and orientation within polymers.¹³⁻¹⁶

Tao and co-workers¹³ applied 9.4 T magnetic field for alignment in coil block copolymers, poly-(2,5-di(2'-ethylhexyloxy)-1,4-phenylenevinylene-*block*-1,4-isoprene) (PPV-*b*-PI), which forms lamellar structures with rigid rods oriented perpendicular to the block copolymer surface. It was observed that the liquid crystalline rods would reorient to the direction parallel to the magnetic field after applying magnetic field. Figure 9.2(A) shows a theoretical WAXS pattern of aligned rod-like structure in block polymer after applying magnetic field. While the experimental WAXS data in Figure 9.2(B) clearly show that scattering arcs were obtained, which demonstrates the alignment of the rod-like blocks under magnetic field. Figure 9.2(C) shows the SAXS scattering pattern when X-rays were parallel to the magnetic field, which clearly demonstrates that the alignment of interface is perpendicular to the magnetic field.

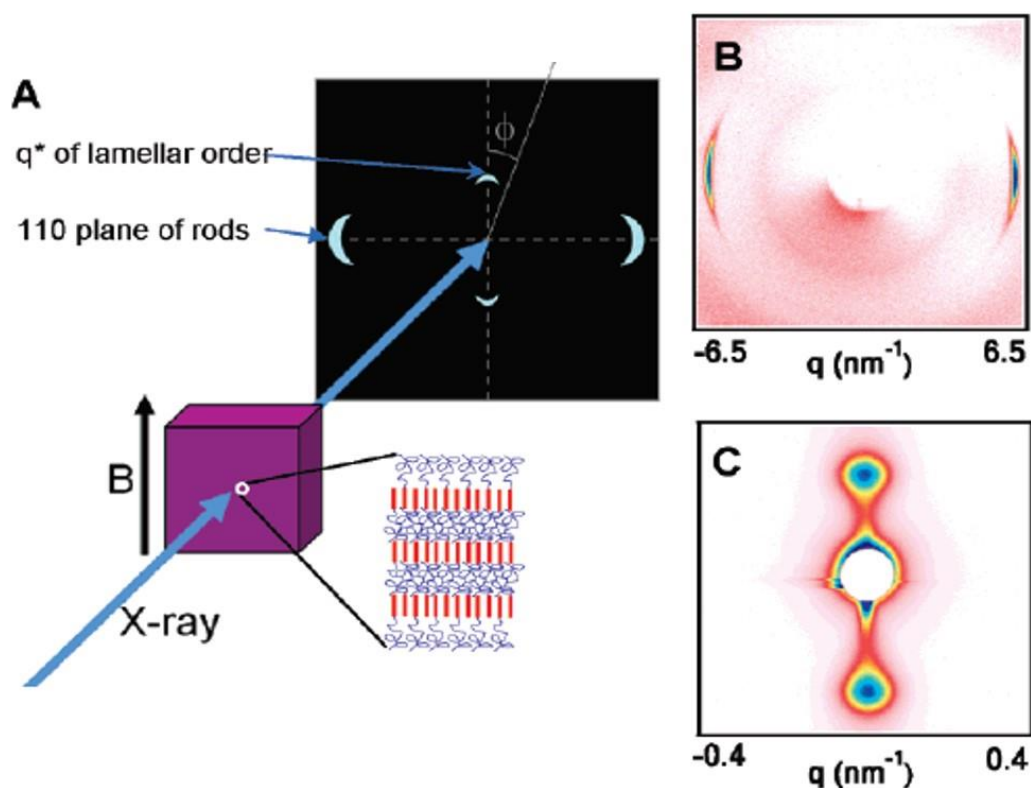


Figure 9.2. (A) Theoretical WAXS pattern of a main chain liquid crystalline block copolymer annealed in a magnetic field at elevated temperature. X-ray beam is perpendicular to the magnetic field direction (B) Experimental WAXS pattern clearly shows the rod-like structure are aligned parallel to the magnetic field (C) SAXS pattern clearly demonstrates the alignment of the blocks within the block copolymer is perpendicular to the magnetic field direction (Reprinted permission with from *Nano Letters* **2007**, 7, 2742. Copyright, The American Chemistry Society, 2007)

Majewski and co-workers also studied the effect of magnetic fields on the morphology of block copolymers.¹⁴⁻¹⁶ By performing SAXS on the poly(ethylene oxide-*block*-methyl acrylate) (PEO-*b*-PMA) block copolymer that were treated under different magnetic field strength, they observed that at least 3T is required to induce significant alignment within this block copolymer.(Figure 9.3) Besides SAXS, the alignment under magnetic field was further demonstrated by conductivity data. In Figure 9.4, significant increase (more than 10-fold) in conductivity was achieved in the perpendicularly aligned sample, while significant decrease in conductivity was observed in the parallel aligned sample due to

much higher electrical resistance of the samples. It is also needs to point out that temperature effect on the conductivity of the aligned samples above the order-disorder transition (ODT) temperature, i.e. a decrease in the conductivity of the perpendicularly aligned samples, is still not well understood. However, it is suggested by the authors that this may be due to the large scale morphological changes in the structure of the samples.

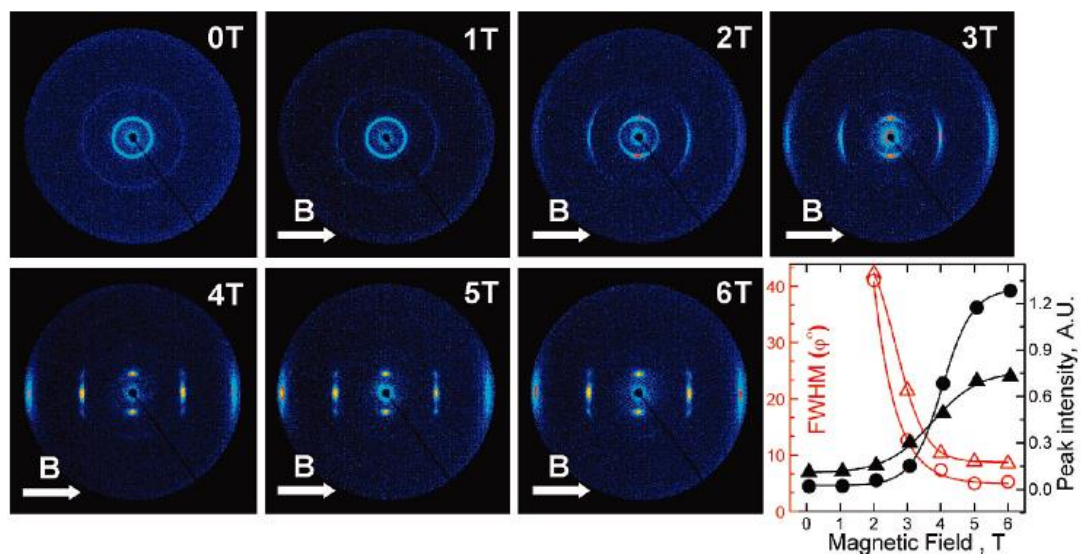


Figure 9.3. SAXS patterns as a function of the applied magnetic field strength. The magnetic field direction is horizontal with respect to the orientation of the X-ray detector. The curves show the peak intensities and peak shapes of the microdomain scattering at $q=0.07 \text{ \AA}^{-1}$ (triangles) and scattering at $q=0.18 \text{ \AA}^{-1}$ (circles), respectively as a function of field strength (Reprinted with permission from *Journal of the American Chemical Society* **2010**, *132*, 17516. Copyright, The American Chemistry Society, 2010)

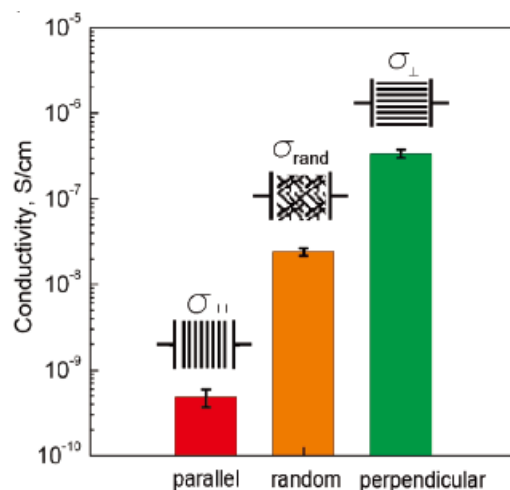


Figure 9.4. The average conductivity of 120:1 EO:Li⁺ sample aligned in 5 T magnetic field in two directions under room temperature, with conductivity of nonaligned sample shown for comparison (Reprinted with permission from *Journal of the American Chemical Society* **2010**, 132, 17516. Copyright, The American Chemistry Society, 2010)

9.2.3 Proposed Further Work on Enhancing Microdomain Orientation in Nafion

We propose that both electric field and magnetic field could be applied during the solution processing Nafion. Electric/Magnetic field could be applied either vertical or parallel to the surface of Nafion. In either case, water channels that contain the ionic aggregates would be aligned parallel to the direction of electric/magnetic field. By performing SAXS on the Nafion membrane in both the in-plane and through plane directions, we would expect to observe anisotropic scattering behaviors if alignments were achieved. Furthermore, in-plane and through-plane proton conductivity measurement could be applied to further confirm the direction of alignments.

Besides, as introduced in Chapter 5, Grazing Incident SAXS (GISAXS) on spin-coated Nafion film could probe the anisotropic alignment of water channels within Nafion thin film. Thus, we could apply similar approach as described in the work by Russell and co-workers¹¹ to examine this alignment within Nafion thin film.

However, both high electric field and magnetic field have the drawback that they require strong electric or magnetic field, which may be difficult to achieve and also dangerous to work with. Previous work on ionic polymer-metal composites (IPMCs) that consist of Nafion showed that under a 3V square-waveform stimulus (i.e. a field of ca. 15 Vmm^{-1}), it would undergo significant bending actuation.¹⁷ The mechanism of this bending behavior was studied by Park and co-workers,¹⁸ and it was suggested that actuation process is strongly affected by the water that contains ionic aggregates within the Nafion membrane in the IPMC. Also, the bending force may be related to the segmental relaxation of the polymer matrix. Thus electro-poling process could also be utilized to achieve alignment of the water channels within Nafion in order to improve transport properties.

Some preliminary work on IPMCs that consist of H^+ -form Nafion did not show significant changes in morphology or improvement in transport properties. However, besides H^+ -form Nafion, tetramethylammonium (TMA^+)-and tetrabutylammonium (TBA^+)-form Nafion could also be utilized for electro-poling process. Furthermore, the electro-poling process should be carried out under a temperature that is above the α -relaxation temperature of Nafion. Since H^+ -form Nafion will degrade when temperature is above 180 $^{\circ}\text{C}$, TMA^+ -Nafion could be a better choice for electro poling process under high temperature. It also needs to be careful here that water will evaporate out when electro-poling temperature is too high. Thus, we could also incorporate Nafion with ionic liquid to facilitate the poling process under high temperature. Then the membrane should be quenched to room temperature right after the poling process in order to lock the alignment formed during the poling process. In order to examine the alignment, both in-plane and through SAXS and conductivity measurements should be performed. We would expect a

significant increase in conductivity in the direction parallel to the alignment of water channels, and a decrease in conductivity in the direction perpendicular to the alignment of water channels. Besides, we would also expect anisotropic scattering behavior from SAXS measurements which would serve to demonstrate the existence of alignment of water channels after electro-poling process.

9.3 References

- (1) Fujimura, M.; Hashimoto, T.; Kawai, H. *Macromolecules* **1982**, *15*, 136.
- (2) van der Heijden, P. C.; Rubatat, L.; Diat, O. *Macromolecules* **2004**, *37*, 5327.
- (3) Heijden, P. C. v. d.; Rosa, A. d. l.; Gebel, G.; Diat, O. *Polymers for Advanced Technologies* **2005**, *16*, 102.
- (4) Page, K. A.; Landis, F. A.; Phillips, A. K.; Moore, R. B. *Macromolecules* **2006**, *39*, 3939.
- (5) Rubatat, L.; Diat, O. *Macromolecules* **2007**, *40*, 9455.
- (6) Li, J.; Park, J. K.; Moore, R. B.; Madsen, L. A. *Nat Mater* **2011**, *10*, 507.
- (7) Park, J. K.; Li, J.; Divoux, G. M.; Madsen, L. A.; Moore, R. B. *Macromolecules* **2011**, *44*, 5701.
- (8) Amundson, K.; Helfand, E.; Davis, D. D.; Quan, X.; Patel, S. S.; Smith, S. D. *Macromolecules* **1991**, *24*, 6546.
- (9) Amundson, K.; Helfand, E.; Quan, X.; Smith, S. D. *Macromolecules* **1993**, *26*, 2698.

- (10) Amundson, K.; Helfand, E.; Quan, X.; Hudson, S. D.; Smith, S. D. *Macromolecules* **1994**, *27*, 6559.
- (11) Morkved, T. L.; Lu, M.; Urbas, A. M.; Ehrichs, E. E.; Jaeger, H. M.; Mansky, P.; Russell, T. P. *Science* **1996**, *273*, 931.
- (12) Lin, H. L.; Yu, T. L.; Han, F. H. *Journal of Polymer Research* **2006**, *13*, 379.
- (13) Tao, Y.; Zohar, H.; Olsen, B. D.; Segalman, R. A. *Nano Letters* **2007**, *7*, 2742.
- (14) Gopinadhan, M.; Majewski, P. W.; Osuji, C. O. *Macromolecules* **2010**, *43*, 3286.
- (15) Majewski, P. W.; Gopinadhan, M.; Jang, W.-S.; Lutkenhaus, J. L.; Osuji, C. O. *Journal of the American Chemical Society* **2010**, *132*, 17516.
- (16) Majewski, P. W.; Gopinadhan, M.; Osuji, C. O. *Journal of Polymer Science Part B: Polymer Physics* **2012**, *50*, 2.
- (17) Park, J. K.; Moore, R. B. *ACS Applied Materials & Interfaces* **2009**, *1*, 697.
- (18) Park, J. K.; Jones, P. J.; Sahagun, C.; Page, K. A.; Hussey, D. S.; Jacobson, D. L.; Morgan, S. E.; Moore, R. B. *Soft Matter* **2010**, *6*, 1444.